Université Lille 1 Sciences et Technologies
Shanghai University
École Doctorale des Sciences de la Matière et du Rayonnement

Thesis

for the degree of

Doctor of Université Lille 1 Sciences et Technologies
and Shanghai University
Major: Molecules and condensed Matter (Lille)
Ferrous metallurgy (Shanghai)

defended by Rong LI,
on the 11st of December 2009

Preparation and ion conductivity of nano to micron grains size Bi_2O_3-Ln_2O_3 (Ln=Dy, Y, Er) ceramics

supervised by: Pr. Rose-Noëlle VANNIER and Pr. Qiang ZHEN

Jury members

Pr. Elisabeth DUJRADO	LEPMI, INP-Grenoble	Rewiewer
Pr. Kexin CHEN	National Natural Science Foundation of China	Rewiewer
Pr. Rose-Noëlle VANNIER	UCCS, ENS-Chimie Lille	Supervisor
Pr. Qiang ZHEN	Shanghai University	Supervisor

Outline

Abstract in English

The aim of this work was the study of the effect of the grain size of bismuth based oxide ceramics on the ionic properties. With the aim to prepare dense ceramics with controlled grain size at the nano-scale, nano-powders of $(Bi_2O_3)_{0.75}(Dy_2O_3)_{0.25}$, $(Bi_2O_3)_{0.75}(Er_2O_3)_{0.25}$, $(Bi_2O_3)_{0.75}(Y_2O_3)_{0.25}$ and $(Bi_2O_3)_{0.75}(Er_2O_3)_{0.125}(Y_2O_3)_{0.125}$ compositions were successfully prepared by a reverse chemical titration method. As shown by XRD and TEM, after annealing for 3 hours at 500°C, powders with single crystal grains with size of about 20nm were obtained. At that stage, a β-form was evidenced for all compositions.

Then, conditions of sintering were optimized. Two techniques were used: pressureless sintering in a conventional furnace and Spark Plasma Sintering (SPS). In both methods, ceramics with relative density higher than 94% were obtained. The grain size was only 20nm by SPS. It ranges from 60nm to 500nm by conventional sintering, for which it was shown that the grain growth was controlled by mass transport through the grain boundaries.

The effect of grain size on total ionic conductivity was studied by impedance spectroscopy for all compositions. For most compositions except yttrium doped compounds, a decrease of total ionic conductivity with grain size was observed due to a predominant blocking effect of grain boundary when grain size decreases. In contrast, almost no evolution of conductivity with grain size was noticed for yttria doped compounds and composition $(Bi_2O_3)_{0.75}(Y_2O_3)_{0.25}$ with grain size of 22nm exhibits a better separation of bulk and grain boundary responses.

Keywords: nanocrystalline ceramics, bismuth oxide, oxide ion conductor, impedance spectroscopy

Abstract in French

L'objectif de ce travail était l'étude de l'effet de la taille des grains de céramiques à base d'oxyde de bismuth sur les propriétés de conduction ionique. Dans le but de préparer des céramiques denses avec des grains de taille nanométrique, une méthode de dosage en retour a permis de réaliser la synthèse de poudres de composition $(Bi_2O_3)_{0.75}(Dy_2O_3)_{0.25}$, $(Bi_2O_3)_{0.75}(Er_2O_3)_{0.25}$, $(Bi_2O_3)_{0.75}(Y_2O_3)_{0.25}$ et $(Bi_2O_3)_{0.75}(Er_2O_3)_{0.125}(Y_2O_3)_{0.125}$. Des échantillons présentant des grains monocristallins d'environ 20nm ont été obtenus, à partir desquels des céramiques denses ont été préparées soit par frittage conventionnel, soit par « Spark Plasma Sintering ». Ces deux méthodes ont conduit à des céramiques de densité relative supérieures à 94%. Une taille de grains de seulement 20nm est obtenue par SPS. Elle varie de 60 à 500nm par frittage conventionnel pour lequel une croissance de grains contrôlée par le transport de matière aux joints de grains, est démontrée.

L'effet de la taille des grains sur la conductivité a finalement été étudié par spectroscopie d'impédance. Une diminution de la conductivité avec la diminution de la taille des grains est généralement observée, probablement due au caractère bloquant des joints de grains. Néanmoins, aucun effet de la taille des grains n'est observé pour les phases substituées à l'yttrium. Au contraire des autres céramiques, la composition $(Bi_2O_3)_{0.75}(Y_2O_3)_{0.25}$ avec des grains de 22nm présente une meilleure séparation des réponses dues aux grains et aux joints de grains.

Mots clés : céramique nanocristalline, oxyde de bismuth, conducteur par ions oxyde, spectroscopie d'impédance

Extended abstract in French

Avec une conductivité de $1 S.cm^{-1}$ à 800°C, δ-Bi_2O_3 peut être considéré comme le meilleur conducteur par ions oxyde, avec des valeurs de conductivité de trois ordres de grandeurs supérieures à celle de la zircone stabilisée à l'Yttrium (YSZ). Avec de telles conductivités, des applications comme capteur d'oxygène ou membrane pour la séparation de l'oxygène de l'air ou encore comme matériaux pour pile à combustible à oxyde solide ont été envisagées. Cependant, cette phase n'est stable que sur un domaine très restreint en température, limité par son point de fusion à 830°C et une transition de phase qui s'accompagne de contraintes mécaniques importantes à 730°C, restreignant ainsi le domaine d'application.

Avec pour objectif, la stabilisation de cette forme haute température à plus basse température, de nombreux essais de substitution partielle du bismuth ont été réalisés. Parmi les substituants possibles, les oxydes de terres rares, Ln_2O_3, ont conduit à des résultats intéressants. Il a ainsi été montré que, dans les systèmes Bi_2O_3-Ln_2O_3, la forme δ était facilement stabilisée à température ambiante par trempe à l'air de la forme haute température pour des taux en $Ln_2O_3 \geq 22{,}5$ mol % (Ln=La-Er and Y).

Pour l'application, des céramiques denses sont nécessaires. Leur microstructure (taille de grains) joue un rôle important car elle peut avoir une influence sur leurs propriétés. Cependant, cette idée est sujette à controverse. Certains auteurs ont montré une diminution de la conductivité avec la décroissance de la taille des grains, alors que d'autres annoncent des conclusions opposées. L'étude de l'effet de la taille des grains sur des matériaux polycristallins à base d'oxyde de bismuth réalisée par Y.J. Lee *et al.* montre une indépendance de la conductivité pour $(Bi_2O_3)_{0.75}(WO_3)_{0.25}$ et $(Bi_2O_3)_{0.7}(SrO)_{0.3}$. A l'inverse, F. C. Fonseca *et al.* décrivent une augmentation de la conductivité ionique de $Bi_{26}Mo_{10}O_{69}$ lorsque la taille des grains diminue de 10μm à 1μm. Cela dit, ces études se sont focalisées sur des céramiques à grains de taille micrométrique et l'effet de leur taille sur la conductivité des phases des systèmes Bi_2O_3-Ln_2O_3 n'a encore jamais été étudié.

L'objectif de ce travail était l'étude de l'effet de la taille des grains à l'échelle nanométrique sur les propriétés électriques des céramiques. Dans un premier temps, après une étude bibliographique sur les phases à base d'oxyde de bismuth, les compositions $(Bi_2O_3)_{0.75}(Dy_2O_3)_{0.25}$, $(Bi_2O_3)_{0.75}(Y_2O_3)_{0.25}$, $(Bi_2O_3)_{0.75}(Er_2O_3)_{0.25}$ et $(Bi_2O_3)_{0.75}(Er_2O_3)_{0.125}$ $(Y_2O_3)_{0.125}$, qui présentent la structure de la forme δ, ont été sélectionnées. La préparation de poudre à grains de taille nanométrique a ensuite été optimisée en combinant les analyses thermiques, la diffraction X et la diffusion Raman. Ces résultats font l'objet du deuxième chapitre. Les méthodes de frittage des céramiques sont présentées dans le troisième chapitre. Deux techniques ont été employées : le frittage conventionnel et le frittage SPS (Spark Plasma Sintering). Leur utilisation conjointe a permis l'obtention avec une large gamme de taille de grains, de céramiques denses qui ont finalement été caractérisées par spectroscopie d'impédance dans le quatrième chapitre.

Les conclusions de chaque chapitre sont résumées ci-après.

Chapitre 1. Rappels bibliographiques sur Bi_2O_3 et les oxydes mixtes de bismuth et de lanthanides et effet de la taille des grains sur la conductivité

Malgré leur sensibilité à la réduction, les phases dérivées de l'oxyde de bismuth restent des matériaux prometteurs pour leurs exceptionnelles propriétés de conduction par ions oxide. Avec une conductivité de $1 S.cm^{-1}$, δ-Bi_2O_3 présente la plus grande valeur qui puisse être espérée pour une conduction ionique. Dans les systèmes Bi_2O_3-Ln_2O_3, les formes δ sont les plus prometteuses. Elles sont métastables mais en diminuant la taille de leurs grains, on peut espérer une meilleure stabilité. De plus la diminution de la taille des grains pourrait avoir un effet bénéfique sur leurs propriétés de conduction, bien que ce point soit sujet à controverse. Avec pour objectif la stabilisation de formes δ, dans la suite de cette étude, des céramiques à grains de taille nanométriques ont été préparées. La composition x=0,25 qui occupe une position centrale dans le domaine de stabilité compris entre 0,222 et 0,292 pour les composés $(Bi_2O_3)_{1-x}(Ln_2O_3)_x$ avec Ln=Dy, Er et Y est apparue comme judicieuse pour éviter la transformation de la phase δ, métastable. L'étude s'est donc portée sur la préparation des phases $(Bi_2O_3)_{0.75}(Dy_2O_3)_{0.25}$, $(Bi_2O_3)_{0.75}(Y_2O_3)_{0.25}$, $(Bi_2O_3)_{0.75}(Er_2O_3)_{0.25}$ mais également $(Bi_2O_3)_{0.75}(Er_2O_3)_{0.125}(Y_2O_3)_{0.125}$. Des travaux ont en effet montré qu'un dopage double ou multiple de Bi_2O_3 était plus favorable à la stabilisation de la structure δ qu'un dopage simple.

Chapitre 2. Préparation et caractérisation des poudres Bi_2O_3-Ln_2O_3 (Ln=Y, Er, Dy) à grains nanométriques

Des poudres de composés dérivés de l'oxyde de bismuth avec des tailles de grains nanométriques ont été préparées avec succès par une méthode de dosage en retour. La méthode de préparation a tout d'abord été optimisée pour la composition $(Bi_2O_3)_{0.75}(Dy_2O_3)_{0.25}$ puis a été appliquée aux autres compositions $(Bi_2O_3)_{0.75}(Er_2O_3)_{0.25}$, $(Bi_2O_3)_{0.75}(Dy_2O_3)_{0.25}$ et $(Bi_2O_3)_{0.75}(Er_2O_3)_{0.125}(Y_2O_3)_{0.125}$). Pour des raisons de stabilité des oxydes et hydroxydes, un pH élevé (11,5) a été retenu et la précipitation est réalisée en versant goutte à goutte une solution de nitrates des précurseurs (0,1mol/L) dans une solution aqueuse d'ammoniaque (50mL dans 550mL). Les conditions de recuit ont ensuite été optimisées en combinant l'analyse thermogravimétrique associée à la spectrométrie de masse, la diffraction X et la spectroscopie de diffusion Raman. Les poudres les plus homogènes sont obtenues quand le précipité filtré est recuit à 500°C pendant 3 heures. Bien que les échantillons présentent des traces de nitrates, elles restent inférieures à 1%. D'un point de vue cristallographique, quelle que soit la composition, des formes β isotypes à β-Bi_2O_3 sont obtenues bien qu'on ne puisse pas écarter la possibilité d'un mélange avec des formes δ. Comme l'attestent la diffraction X et la microscopie électronique à transmission, des poudres à grains monocristallins de taille d'environ 20nm sont systématiquement obtenues.

Chapitre 3. Céramiques denses à taille de grains nanométrique

En utilisant les poudres obtenues après recuit à 500°C pendant 3 heures, des céramiques denses avec différentes tailles de grains ont été réalisées par frittage SPS d'une part et frittage conventionnel, d'autre part.

En se basant sur les domaines de stabilité des diagrammes Bi-O, Bi(Dy)-O, Bi(Er)-O et les courbes de retrait obtenues par dilatométrie, les conditions du frittage SPS ont été optimisées pour la composition $(Bi_2O_3)_{0.75}(Dy_2O_3)_{0.25}$. Les mêmes conditions ont ensuite été appliquées aux autres compositions. Des céramiques présentant des densités relatives supérieures à 94%, ont ainsi été préparées par frittage SPS à 500°C, pendant une minute. Quelle que soit la composition, les échantillons adoptent la forme δ et des tailles de grains de l'ordre de 20nm.

Des échantillons de densités supérieures à 94% ont également été obtenus par frittage conventionnel. Cependant, dans ce cas, des températures plus élevées sont nécessaires et un grossissement des grains est alors observé. Comme montré par l'évolution de la taille des grains en fonction de la durée du frittage, la croissance des grains est contrôlée par le transport de matière aux joints de grains. Ainsi, des céramiques denses avec différentes tailles de grains ont été obtenues. Le frittage a été réalisé 2h à 700°C, 1h à 750°C et 1h à 800°C. Les tailles de grains varient entre 60nm et 500nm, suivant la température de frittage et la composition.

Chapitre 4. Effet de la taille des grains de céramiques denses sur les propriétés d'électrolyte à base d'oxyde de bismuth

Des analyses par spectroscopie d'impédance ont été menées sur les céramiques de compositions $(Bi_2O_3)_{0.75}(Dy_2O_3)_{0.25}$, $(Bi_2O_3)_{0.75}(Er_2O_3)_{0.25}$, $(Bi_2O_3)_{0.75}(Y_2O_3)_{0.25}$ et $(Bi_2O_3)_{0.75}(Er_2O_3)_{0.125}(Y_2O_3)_{0.125}$, présentant des tailles de grains allant de 20nm à 2µm. A l'exception des compositions à base d'yttrium, une diminution de la conductivité est observée lorsque la taille des grains décroit. Bien que dans ces cas, la séparation entre la réponse due au matériau et celle due aux joints de grains n'a pas pu être mise en évidence, la diminution de la conductivité est attribuée à l'effet bloquant des joints de grains. A la différence des travaux de Nakayama qui annoncent de meilleures propriétés pour le composé au Dysprosium, dans notre étude, les phases dopées Yttrium présentent les meilleures valeurs de conductivité. Pour ce matériau, l'effet de la taille des grains sur la conductivité est plus modeste, peu d'évolution est observée. La conductivité de l'échantillon présentant des tailles de grains de l'ordre de 62nm est inférieure à celle des échantillons avec des tailles de grains de l'ordre de 104nm mais une valeur intermédiaire est observée pour l'échantillon avec des tailles de grains de 22nm. Cependant, les variations restent de l'ordre de la précision des mesures. Néanmoins, pour l'échantillon présentant une taille de 22nm, les réponses des grains et des joints de grains sont parfaitement séparées. Un modèle de type « brick layer » a alors été utilisé pour extraire les paramètres associés aux grains et aux joints de grains. La conductivité des joints de grains présente une énergie d'activation plus élevée que les grains. On ne peut pas exclure un effet de charge d'espace mais il est difficile de conclure avec des échantillons préparés avec des méthodes différentes et un seul point de mesure.

Conclusion

Dans cette étude des poudres à grains de taille nanométrique de composition $(Bi_2O_3)_{0.75}(Dy_2O_3)_{0.25}$, $(Bi_2O_3)_{0.75}(Y_2O_3)_{0.25}$, $(Bi_2O_3)_{0.75}(Er_2O_3)_{0.25}$, et $(Bi_2O_3)_{0.75}(Er_2O_3)_{0.125}(Y_2O_3)_{0.125}$ ont été préparées par une méthode de dosage en retour. Des céramiques denses avec différentes tailles de grains ont été obtenues par frittage SPS et frittage conventionnel. L'effet de la taille des grains sur la conductivité a été étudié et ressortent les conclusions suivantes :

(1) Pour éviter la formation de $BiONO_3$ et obtenir des précipités d'oxydes et d'hydroxydes, les espèces en solution ont été déterminées afin de définir un pH adéquat. La précipitation est provoquée en versant goutte à goutte une solution de précurseurs de nitrates (0.1mol/L) dans une solution aqueuse d'ammoniaque (50mL dans 550mL) à pH=11,5. Seuls BiOOH, $Dy(OH)_3$, $Y(OH)_3$ et $Er(OH)_3$ étaient prédits comme produits finaux à l'équilibre. Cependant, les analyses par TG-MS et diffusion Raman révèlent des traces de nitrates.

(2) Sur la base des caractérisations par TG-MS, XRD et spectroscopie Raman, les conditions de recuit des poudres ont été optimisées. Les échantillons les plus homogènes sont obtenus par filtration du précipité et recuit à 500°C pendant 3 heures. Bien que des traces de nitrates soient observées, leur quantité est inférieure à 1%. D'un point de vue cristallographique des formes de structure β sont obtenues, sans que l'on puisse écarter la possibilité d'un mélange des formes β et δ. Comme montré en combinant diffraction X et microscopie électronique à transmission, les poudres présentent des grains monocristallins de 20nm environ. Leur composition a été vérifiée par fluorescence X et est en bon accord avec celle attendue.

(3) Sur la base des diagrammes de stabilité des systèmes Bi-O, Bi(Dy)-O, Bi(Er)-O et des courbes de retrait, les conditions de frittage ont été optimisées pour la composition $(Bi_2O_3)_{0.75}(Dy_2O_3)_{0.25}$. Deux techniques ont été utilisées : le frittage SPS (Spark Plasma Sintering) et le frittage conventionnel.

(4) Par SPS, des céramiques avec des densités relatives supérieures à 95% sont obtenues avec un palier de 1 min à 500°C. Des analyses par diffraction X confirment la stabilisation de forme δ avec une taille de grains de l'ordre de 20nm.

(5) Pour le frittage conventionnel, l'étude de la taille des grains en fonction du temps de frittage montre que le grossissement des grains est contrôlé par le transport

de matière aux joints de grains. Des céramiques de densités relatives supérieures à 94% sont obtenues pour des frittages de 2h à 700°C, 1h à 750°C et 1h à 800°C. Tous les échantillons présentent la forme δ avec des tailles de grains allant de 60nm à 500nm, suivant la température de frittage et la composition.

(6) Au contraire de ce qui pouvait être espéré au début de l'étude, la diminution de la taille des grains ne permet pas une meilleure stabilité de la forme δ à 650°C.

(7) Les spectres d'impédance des phases $(Bi_2O_3)_{0.75}(Dy_2O_3)_{0.25}$ et $(Bi_2O_3)_{0.75}(Y_2O_3)_{0.25}$ ont été étudiés en détail. Pour la plupart, il n'a pas été possible de séparer les contributions dues aux grains de celles des joints de grains à l'exception de la composition $(Bi_2O_3)_{0.75}(Y_2O_3)_{0.25}$ d_g=22nm, pour laquelle deux demi-cercles sont observés.

(8) A l'exception des compositions à base d'oxyde d'yttrium, une diminution de la conductivité lorsque la taille des grains diminue est généralement observée. Ce point s'explique par une augmentation de la densité des joints de grains qui prédomine à l'effet de blocage.

Pour conclure, ce travail démontre la possibilité de préparer des céramiques à base d'oxyde de bismuth à grains de taille contrôlée à l'échelle nanométrique. Bien que la contribution des joints de grains reste l'effet prépondérant dans le blocage de la conductivité, pour de très petits grains, un effet de charge d'espace est possible mais reste à démontrer.

Acknowledgements

First of all, I want to express my acknowledgements to Pr. Elisabeth DUJRADO and Pr. Kexin CHEN, for spending time to review my thesis and for their comments. These comments were very helpful in improving the quality of my manuscript.

Second, I would like to show my deepest gratitude to my supervisors: Pr. Rose-Noëlle VANNIER and Pr. Qiang ZHEN, for their careful guidance for completion of this thesis. During these three years， they worked with me and give me numerous advices. From the topics of papers, the experimental program design to the analysis of data, the implementation to the final thesis, they had devoted a great deal of efforts. They are respectable, responsible and resourceful scholars, and their keen and vigorous academic observation enlightens me not only in this thesis but also in my future study. And I also want to thank Pr. VANNIER, for her help in my life in France.

Then, I want to give my acknowledgements to Dr. Michel DRACHE, who also worked with me and give me many helps in the experiments, the completion of the thesis, etc; and Pr. Annick RUBBENS, who helps me much in characterization of the samples by Raman. I also would like to thank all the staffs of UCCS and the staffs of Advance ceramic lab in Shanghai University for their help in every aspect of my work and life.

I am also grateful to the French Embassy in China and International center at USTL, since they gave me this chance to study as a co-culture Ph.D student. I'm very glad to have this opportunity to do my thesis with my superviors in two countries and have met so many friends.

Last, I'd like to thank all my friends, for their encouragement and support; and everyone who had ever helped me during these three years.

Introduction

δ-Bi_2O_3 exhibits the best oxygen ion conductivity, which is at least 3 orders of magnitude higher than YSZ with a conductivity value of $1 S.cm^{-1}$ at 800°C[1]. With such a high conductivity, it was considered as a potential material for application in the fields of oxygen sensors, oxygen separation and even solid oxide fuel cells. However this δ-form is only stable from 730°C to 830°C and, from the mechanical point of view, exhibits a drastic phase transition which limits its application. With the aim to stabilize this high temperature form at lower temperature, numerous partial substitutions of bismuth were performed. Among the possible substituents, Ln_2O_3 was considered as an effective additive. Then, it was shown that in Bi_2O_3-Ln_2O_3 systems, the δ-phase was easily stabilized at room temperature by sample air quenching from its high temperature stability domain for Ln_2O_3 contents ≥22.5 mol % (Ln=La-Er and Y). This metastable δ-phase clearly exhibits the most promising properties.

High ionic conductivity is an important parameter for the applications. Dense ceramics are needed and microstructure (size of grains) may have an impact on the properties. However this idea is still a subject of controversy. Some authors showed that the ionic conductivity decreased with decrease of grain size, while the opposite conclusions were also reported. Effect of grain size on the ionic conductivity of Bi_2O_3-based polycrystalline material was studied by Y.J. Lee *et al.*[2] who found that the ionic conductivity was independent of grain size in $(Bi_2O_3)_{0.75}(WO_3)_{0.25}$ and $(Bi_2O_3)_{0.7}(SrO)_{0.3}$ materials. In contrast, F. C. Fonseca *et al.*[3] reported that the ion conductivity of $Bi_{26}Mo_{10}O_{69}$ increased with the decrease of grain size from 10μm to 1μm. However, these studies were focused on microcrystalline Bi_2O_3-based material, and the effect of grain size on the ionic conductivity of Bi_2O_3-Ln_2O_3 system was not reported before.

The aim of the present work was the study of the effect of grain size at the nanoscale on the electrical properties of ceramics. After a brief review on bismuth based materials, compositions $(Bi_2O_3)_{0.75}(Dy_2O_3)_{0.25}$, $(Bi_2O_3)_{0.75}(Y_2O_3)_{0.25}$, $(Bi_2O_3)_{0.75}(Er_2O_3)_{0.25}$, $(Bi_2O_3)_{0.75}(Er_2O_3)_{0.125}$ $(Y_2O_3)_{0.125}$ which display the δ structural type were selected. Then, preparation of nano-powders was optimized by combining thermal analyses, X-ray diffraction and Raman scattering. It will be presented in the second chapter of this manuscript before the optimization of sintering conditions using conventional sintering on one hand, and Spark Plasma Sintering, on the other hand, in the third chapter. Dense ceramics with different grain size were obtained, and at last, the effect of grain size on the ionic conductivity was studied in chapter 4.

References

[1] Takahashi T, Iwahara H, Nagai Y. *J. Appl. Electrochem.*, 1972, **2**: 97.
[2] Lee YJ, Park CO, Beak HD, Hwang JS. *Solid State Ionics*, 1995, **76**: 1.
[3] Fonseca FC, Steil MC, Vannier RN, Mairesse G, Muccillo R. *Solid State Ionics*, **140**: 61

Chapter 1

Bibliographical recalls on Bi_2O_3 and Bi-Ln mixed oxides systems and grain size effect on conductivity

Among oxide ion conductors, δ-Bi_2O_3 exhibits the best oxide ion conductivity. With a conductivity of $1 S.cm^{-1}$ at 800°C, it can be considered as the pragmatic limit of oxide ion conduction in solid electrolyte. Unfortunately, this high temperature form of Bi_2O_3 is only stable in a very narrow domain of temperature, limited by its melting point at 825°C and a phase transition at 730°C. Numerous substitutions were performed to stabilize this high temperature form at lower temperature; solid solutions obtained with lanthanides are reviewed in this chapter after a description of the different varieties of Bi_2O_3. Moreover, according to several studies, a decrease of the ceramic grain size to the nano-scale could have a beneficial impact on their properties. A few studies were carried out on stabilized zirconia and doped ceria, and the effect of grain size will be discussed at the end of this chapter.

1.1 Bi_2O_3-based solid electrolyte

1.1.1 Bi_2O_3 polymorphism

Six Bi_2O_3 varieties, labelled α, β, γ, δ, ε and ω-, have been reported in the literature. Their principal structural characteristics, reviewed below, are summarized in Table 1.1.

The room temperature stable variety is the α- monoclinic form. Its structure was investigated on single crystal and on powder samples using X-ray diffraction and neutron diffraction data[1-8]. It crystallizes in the $P2_1/c$ space group with the following unit cell parameters: a=5.8444(2), b=8.1574(3), c=7.5032(3)Å, β=112.97(1)° [8]. It exhibits four Bi_2O_3 units per unit cell and the structure can be described as a succession of alternated layers of bismuth atoms and oxide ions, parallel to the (100) plane with voids along [001].

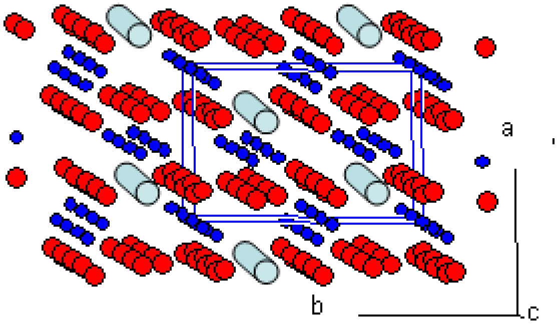

Fig.1.1 α-Bi_2O_3 layered structure, atomic representation with oxygen voids alignments (light blue rolls)

Table 1.1 Domains of stable and metastable reported Bi_2O_3 polymorphs[9]

T (°C)	**Phases**				
	Liquid	Liquid	Liquid	Liquid	δ-phase
900 --					↑
825 –	**δ-phase**	δ-phase ↓	δ-phase ↓	δ-phase	
800 --					**ω-phase**
	fcc				
730 –	↑			↑	*triclinic*
650 –					
639 –					
		β-phase ↓	**γ-phase** ↓		
		tetragonal	*bcc*		
500 –					
			α-phase	α-phase	
400 --			or	↑	
			possibly		
330 –					
			γ-phase		
240 --		α-phase		**ε-phase**	
	α-phase		which may persist to room temperature	*tetragonal*	
	monoclinic				

When increasing the temperature, at 730°C, α- turns into the δ- high temperature form which is stable between 730 and approximately 825°C, the melting point of the material. Structural investigation based on high temperature powder X-ray diffraction[10], showed that this δ form crystallizes in a cubic cell (space group $Fm\bar{3}m$; Z=2; $a_{750°C}$=5.66Å). It belongs to the CaF_2-type structure (the so-called fluorite) with a ¼ defective anionic 8*c* Wyckoff site. The characterization of this structure was recently completed by combining neutron diffraction data, Rietveld refinement and maximum entropy methods[11]. The structural disorder was clarified, with a split of the oxygen ions in 8*c* and 32*f* sites with partial occupancy fitting to the total oxygen content (6 per cell). All the descriptions, with partial occupancy of the anions sites by oxygen atoms (which can consequently move from one site to another) are thoroughly supported by the highly conductive character of δ-Bi_2O_3. Because of the high oxygen motion in this form, the structure is better described as built upon a Bi skeleton merged in an oxygen liquid like system.

During the cooling process, δ- doesn't lead directly to the α-variety. The δ-form is preserved in a significant temperature range (730-640°C) and then it transforms into metastable forms.

Depending on the sample thermal treatment, the tetragonal β-Bi_2O_3 phase can be obtained near 650°C, or the body centered cubic γ-variety at about 640°C[12]. The subsequent transformation of β, nearby 300°C, leads to α- whereas γ- can persist to room temperature using low cooling rate[13].

The β-Bi_2O_3 structure was determined in the space group $P\bar{4}2_1c$ with Z=4 and the following lattice parameters at 643°C: *a*=7.738(3) and *c*= 5.731(8)Å[13, 14]. This cell is related to the δ-cubic cell from the relationships $\vec{a}_\beta = \vec{a}_\delta + \vec{b}_\delta$, $\vec{b}_\beta = -\vec{a}_\delta + \vec{b}_\delta$, $\vec{c}_\beta = \vec{c}_\delta$[9]. The structure corresponds to a distorted anionic deficient fluorite structure with voids in the oxygen sublattice, ordered in the [001] direction.

γ-Bi_2O_3 is isomorphous with $Bi_{12}GeO_{20}$ (S.G. I23; Z=2)[12, 15] and its room temperature lattice parameter is *a*=10.268(1)Å. This cell is related to the δ-cubic cell from the relationships $\vec{a}_\gamma = 1/2\,\vec{a}_\delta - \vec{b}_\delta + 3/2\,\vec{c}_\delta$, $\vec{b}_\gamma = \vec{a}_\delta + 3/2\,\vec{b}_\delta + 1/2\,\vec{c}_\delta$, $\vec{c}_\gamma = -3/2\,\vec{a}_\delta + 1/2\,\vec{b}_\delta + \vec{c}_\delta$[9]. The most recent structure determination was realized using neutron diffraction data[16]. Bismuth was observed in 24*f* and partially occupied (0.8) 2*a* sites.

Oxygen was localized in 24f sites and in two sets of 8c sites; one kind only of the 8c sites was partially occupied.

Two other Bi_2O_3 varieties, reported as meta-stable forms, were also obtained using very specific synthesis conditions.

The orthorhombic ε-Bi_2O_3 polymorph was prepared as single crystalline phase from hydrothermal treatment of $Bi(NO_3)_3.5H_2O$, MnO_2, $MnSO_4.H_2O$ and $(NH_4)_2HPO_4$ in highly concentrated KOH [17] (a=4.9555(1), b=5.5854(2), c=12.7299(3)Å). This cell is related to the δ-cubic cell from the relationships $\vec{a}_{\varepsilon}=\vec{a}_{\delta}$, $\vec{b}_{\varepsilon}=\vec{b}_{\delta}$, $\vec{c}_{\varepsilon} = 2\vec{c}_{\delta}$[9]. On progressive heating, ε-Bi_2O_3 transforms into monoclinic α- variety which subsequently follows its normal behavior. The ε-Bi_2O_3 crystal structure was resolved in Pbnb space group with Z=4; it is essentially characterized by the oxygen organization, whereas the cationic sublattice is closely similar to the fcc δ-type one. The structure was described as an arrangement of $[Bi_2O_3]$ columns formed by edge-sharing OBi_4 tetrahedrons and developing along [010] direction.

Triclinic ω-Bi_2O_3 variety, characterized by powder X-ray diffraction pattern (a=7.2688(4), b=8.6390(6), c=11.9698Å; α=87.713(6), β=92.227(6), γ=86.653(4)°), was obtained at 800°C on a BeO substrate; $P\bar{1}$ was given as possible space group with Z=9[18]. A transition ω→ δ was announced at 900°C, although the melting point of pure Bi_2O_3 is expected at 825°C.

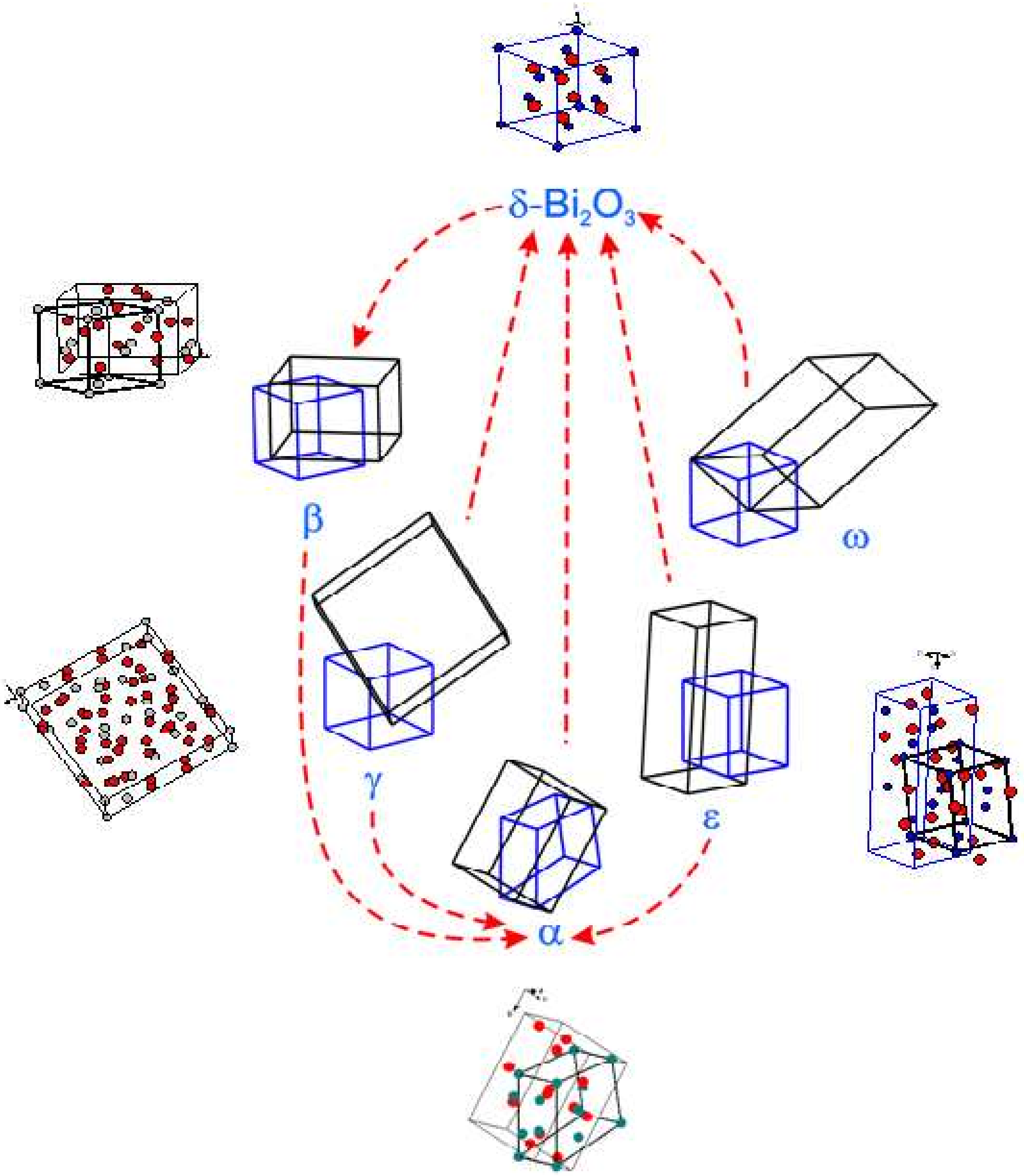

Fig.1.2 Lattice relationships for various pairs of low and high temperature Bi_2O_3 varieties[9]

On the basis of the crystalline data of each polymorph (cationic sublattice organization, or lattice parameters in the case of ω-), the structural matrix relationship between the considered variety and the δ- high temperature variety was determined [9]. Fig.1.2 gives an account of these matrix relationships. Considering only the heavy atoms network, therefore the cations lattice, the structural modification during each transition was examined. The modification of the cationic network is significant during the α→δ transition, whereas it is light during the δ→β or δ→γ transformations. This explains the easy β- and γ- formations on δ- cooling.

Harwing and Gerards systematically measured the conductivities of α, β, γ and δ-phase of Bi_2O_3. Fig.1.3[19] shows some typical plots of conductivity versus temperature for Bi_2O_3, during repeated heating and cooling runs. The conductivity was found to increase by 3 orders of magnitude when α transformed to δ at 730°C. δ-Bi_2O_3 exhibits the highest ion conductivity, but it is only stable from 730°C to 830°C, and the phase transition from α to δ is accompanied with a high volume change which causes microcracks in the ceramic and results in performance deterioration.

Many attempts were performed to stabilize the δ-form properties at lower temperatures. Among the possible substitutions, Ln_2O_3 was considered as an effective additive, and has been intensively investigated.

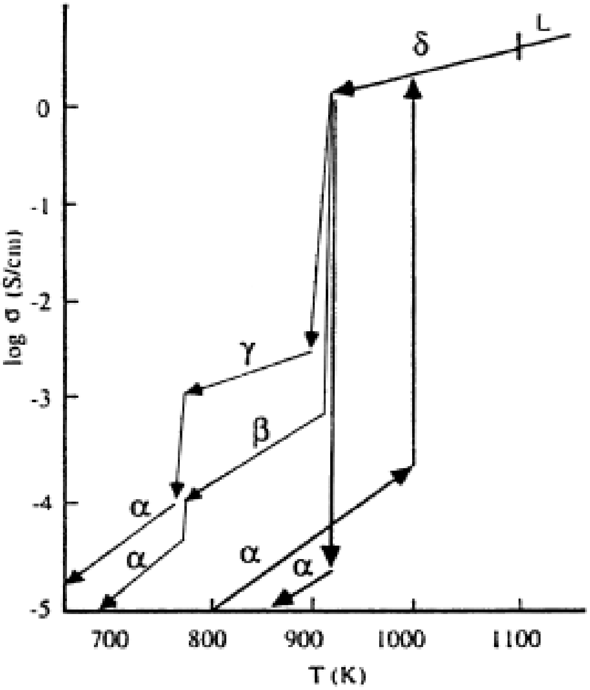

Fig.1.3 Electrical conductivity of Bi_2O_3 as a function of temperature[19]

1.1.2 Bi_2O_3-Ln_2O_3 equilibrium phase diagrams

Resulting from the numerous $Bi_{1-x}Ln_xO_{1.5}$ phase investigations, several Bi_2O_3-Ln_2O_3 equilibrium phase diagrams were reported. Among these, the most accurate diagrams, for *Ln*=La[20], Yb[21] or for Y[22], cover a wide *Ln* size range. The major parts of these three diagrams $0 \leq x \leq 0.8$ are gathered within a 3D representation allowing the correlation of phase compositional domains to the *Ln* size[9] in Fig.1.4.

The most striking common feature of these diagrams is the presence of an extended high temperature domain of solid solution related to the δ-Bi_2O_3 polymorph. In each case, the maximum temperature of the domain corresponds to the melting point of the sample. The minimum temperature of the domain corresponds to an eutectoidic or a peritectoidic transformation, or a transition between two single phases as the $\beta_1 \rightarrow \delta$ phase transition for the lanthanum based system (18-35% La). The wide range in composition for the δ-domain results from the analogy of Bi_2O_3 and Ln_2O_3 sesquioxides concerning the formulas, the cationic size, as well as the crystalline structure. Indeed, each of the Ln_2O_3 oxides exhibits at least a bcc cubic form (S.G. *Ia*3; $a \cong 10.4$-11.4Å)[23], which can be considered as close to a 2x2x2 superstructure of a fluorite type variety.

In the low temperature range, definite compositions exist, possibly surrounded by domains of non-stoichiometry; thus, larger the lanthanide size, wider the composition domain range. $Bi_{17}Ln_7O_{36}$ is evidenced for lanthanides with small radius (Er-Lu), $Bi_{1-x}Ln_xO_{1.5}$ with $x = 0.5 \pm \delta$ are observed for lanthanides in between Dy and Lu and for Y whose properties are close to lanthanides ones. Another solid solution around composition $Bi_5Ln_3O_{12}$ exits for *Ln*= Sm-Yb including Y. For lanthanides with larger radius, the definite compound $Bi_8La_{10}O_{17}$ is evidenced and in between La and Ho, including Y, two other solid solutions are to be noticed; the first with high *Ln* content ($x>0.5$) with a structure of LaOF type and the second corresponding to the rhombohedral phase (β_1,β_2) for $x<0.375$.

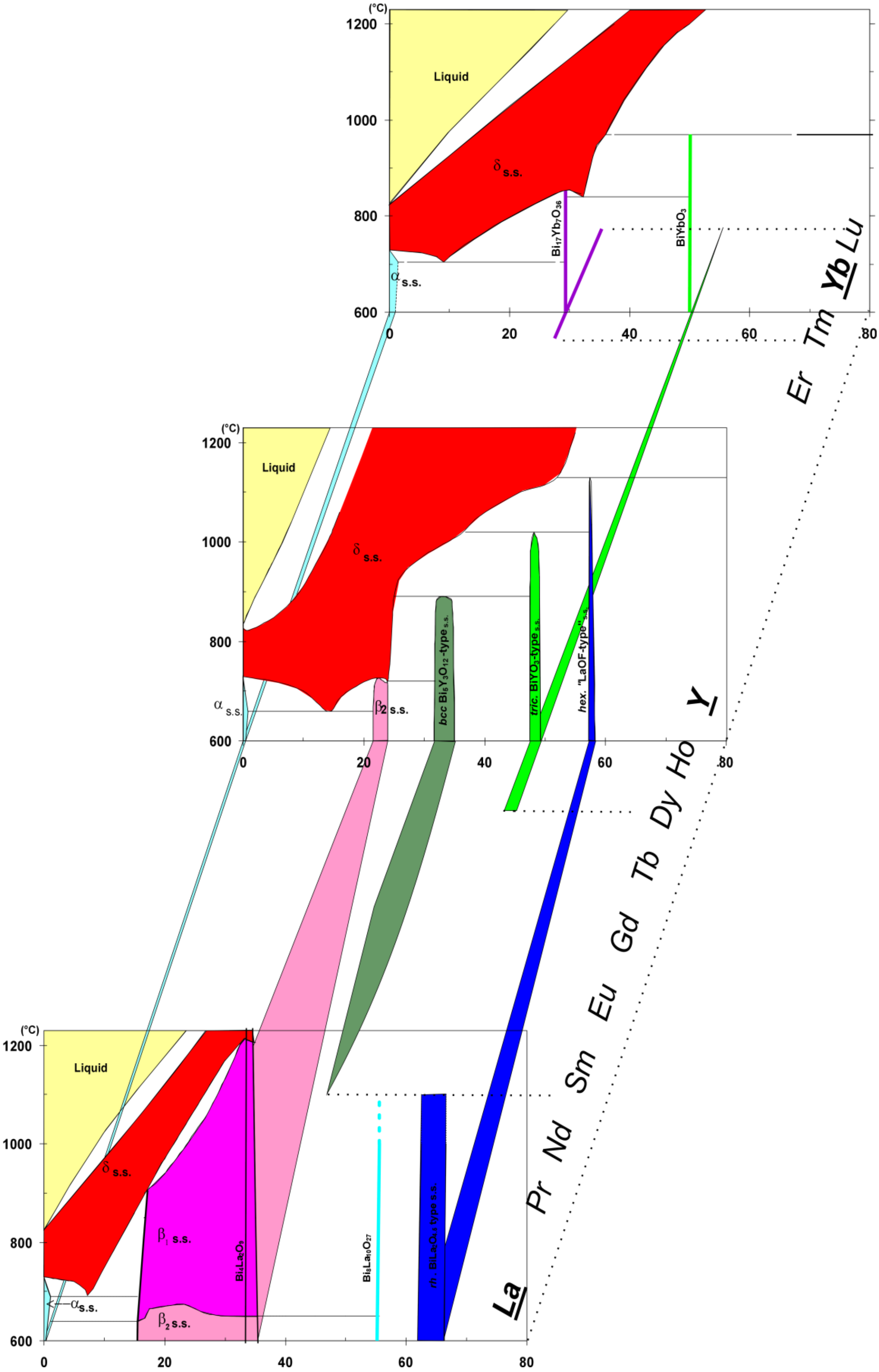

Fig.1.4 Representative $Bi_{1-x}Ln_xO_{1.5}$ phase diagrams (0-80% La cationic ratio) [9]

1.1.3 β-($0<x\leq0.08$) and δ-($x>0.08$) $Bi_{1-x}Ln_xO_{1.5}$ metastable phases

Until the discovery of some $Bi_{1-x}Ln_xO_{1.5}$ phases thermodynamically stable at room temperature, the researchers believed the obtained δ-phase to be stable at room temperature in significant compositional ranges. However, A. Watanabe[24] claimed that in all cases, it was metastable at room temperature. Despite that the high temperature δ-phase exists for x=0, this phase can not be preserved at room temperature below a minimum x lanthanide ratio. This minimum value depends on the cooling conditions (quenching in air or liquid nitrogen) and also on the lanthanide size. Moreover, for a lanthanide content lower than a critical x value ($x \cong 0.08$), a tetragonal β-Bi_2O_3 type phase is obtained by transformation of δ-phase (e.g. β-$Bi_{0.96}La_{0.04}O_{1.5}$ (PDF 41-0273), β-$Bi_{0.9}Yb_{0.1}O_{1.5}$[25]). The maximum x value allowing the quenching at room temperature of pure δ-type phase, depends on the treatment temperature.

Room temperature cell parameters of δ- and β- phases were reported for various compositions with *Ln* = Y, La-Lu. Different examples of composition dependence, for a given rare earth (*Ln* = Y, Sm-Yb)[26-29], were presented. Investigations were also reported showing the quenching domains extents of δ- in ternary oxide systems based on Bi-Y-Pb[30], Bi-Sm-Pb[31], Bi-*Ln*-V (*Ln*=La-Yb)[32], Bi-*Ln*-Te (Ln=La, Sm, Gd, Er)[33] or quaternary ones based on Bi-Sm-V-*M* (*M*=Pb, Co, Ni)[34]. Doping Bi_2O_3 using two elements or more than two, appears more favourable for the stabilization of the δ structure than single doping. On heating, the β-type phases transform into the low temperature stable phases (α-Bi_2O_3 + β_2-(poor Bi solid solution limit)), and subsequently into the δ-high temperature phase (Fig.1.5)

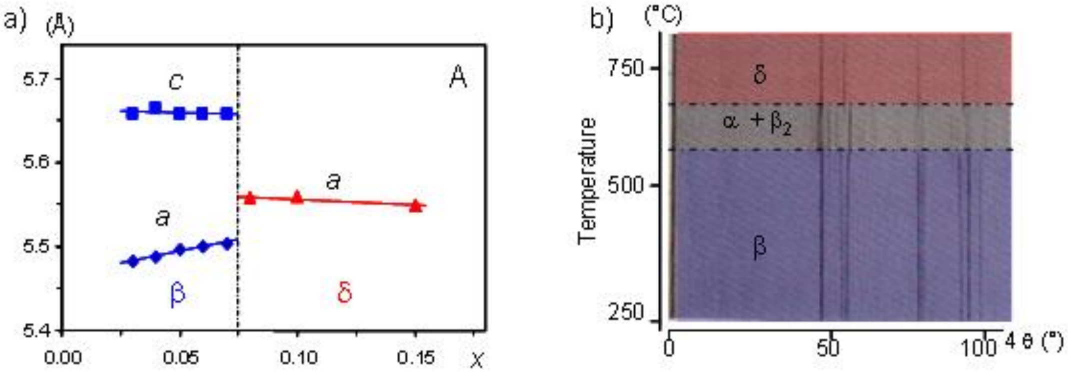

Fig.1.5 β- and δ-$Bi_{1-x}Sm_xO_{1.5}$ domain identification[9]:
(a) composition cell parameters dependence;
(b) temperature - Guinier Lenné evolution.

Structure neutron diffraction investigations of δ-Bi_2O_3[6, 35] and δ-(Bi_2O_3-Ln_2O_3) related phases[36-38], were reported and interpreted from a fluorite type model in which some additional interstitial oxide sites were observed. $(Bi_2O_3)_{0.8}(Er_2O_3)_{0.2}$ thermal investigation between 27 and 827°C led Verkerk *et al.*[36] to conclude that there is no long range ordering of vacancies at high temperature; a short-range ordering appears at low temperature, with the occurrence of short *Ln*-O distances and the oxide sub-lattice disorders above 597°C. This polymorphism was characterized by two temperature dependence domains of the cell parameters and of the Arrhenius plot of the conductivity. Another structural investigation concerning this material after quenching or aging (500°C annealing treatment for 2 weeks)[37] showed the distribution of oxide ions over three anionic sites, allowing to distinguish between quenched and annealed structures. Two anionic sites are occupied for quenched samples (33/54%), similarly to $(Bi_2O_3)_{0.73}(Y_2O_3)_{0.27}$ treated at 500°C for 1 day[15], whereas only one site is significantly occupied for annealed samples (87%). These characteristics, likely exist for all similar δ-type mixed oxides with two or several cations including Bi^{3+}, even when structural studies based on X-ray diffraction data such as for $Bi_{0.65}Yb_{0.35}O_{1.5}$ [25, 39-41] or $Bi_{0.85}Pr_{0.15(1-n)}V_{0.15n}O_{1.5+0.15n}$ (n=0.1, 0.3, 0.5)[42] can not reveal all the sites identified from neutron data. Indeed, these materials[37, 43] also exhibit two almost linear domains of cell parameter dependence versus temperature, as well as $Bi_{0.85}Ln_{0.105}V_{0.045}O_{1.545}$ (*Ln* = Y, Sm-Yb)[32] or $Bi_{0.85}Sm_{0.105}V_{0.018}Pb_{0.027}O_{1.5045}$[33].

The β phase was reported in different papers for *Ln*=Sm[27, 44], Gd[45, 46], Eu[47], Yb[48], and for Y[49]. Similarly to the δ-type phase, β- structure Rietveld refinements were performed from X-ray data with two fully occupied oxygen sites whereas using neutron diffraction data, three sites partially occupied were evidenced.

δ- and β-$Bi_{1-x}Ln_xO_{1.5}$ thermal behavior investigations clearly indicates that both phases are metastable below 730°C. Their transformation into stable phases, nearby 600°C, is unambiguously evidenced during a long time heating of δ- bismuth rich samples for Sm[27], Er[50], Y[31, 51], and of β for Sm[27]; the temperature of δ-transformation increases when the bismuth content decreases. A favorable effect on the δ- stability was also observed, when the oxygen vacancy ratio decreased during substitution of *Ln* with V (e.g. in δ-$Bi_{0.85}Ln_{0.105}V_{0.045}O_{1.545}$ (*Ln*= Y, Sm-Yb) samples[32]). Thus no transformation is observed for some specific samples of the δ phase which can then be erroneously presented as thermodynamically stable. TG investigations of such a quenched δ phase, led authors to consider an evolution of the oxide stoichiometry during analyzes conducted under various oxygen pressures[49, 50].

However, the review paper[9] clearly shows, from the point of view of conductivity properties, the superiority of metastable δ-phase, compared to the other phases which can be obtained in the considered *x* composition range. The δ-conductivity is slightly higher than β_1 or β_2 conductivity, and 100 times higher than that of orthorhombic $Bi_{17}Ln_7O_{36}$ or tetragonal β-$Bi_{1-x}Ln_xO_{1.5}$ phases.

Many researchers studied the conductivity properties of the δ-phase at various temperatures, either within various specific $Bi_{1-x}Ln_xO_{1.5}$ systems[7, 27, 28, 52-56]. The Arrhenius plots obtained for Ln = Er[53], Dy[56] (Fig.1.6) and for Y[7] are presented in Fig.1.7. Comparisons of conductivity performances for δ- oxide phases based on three[24, 31-33, 57, 58]or four cations[34] were also reported.

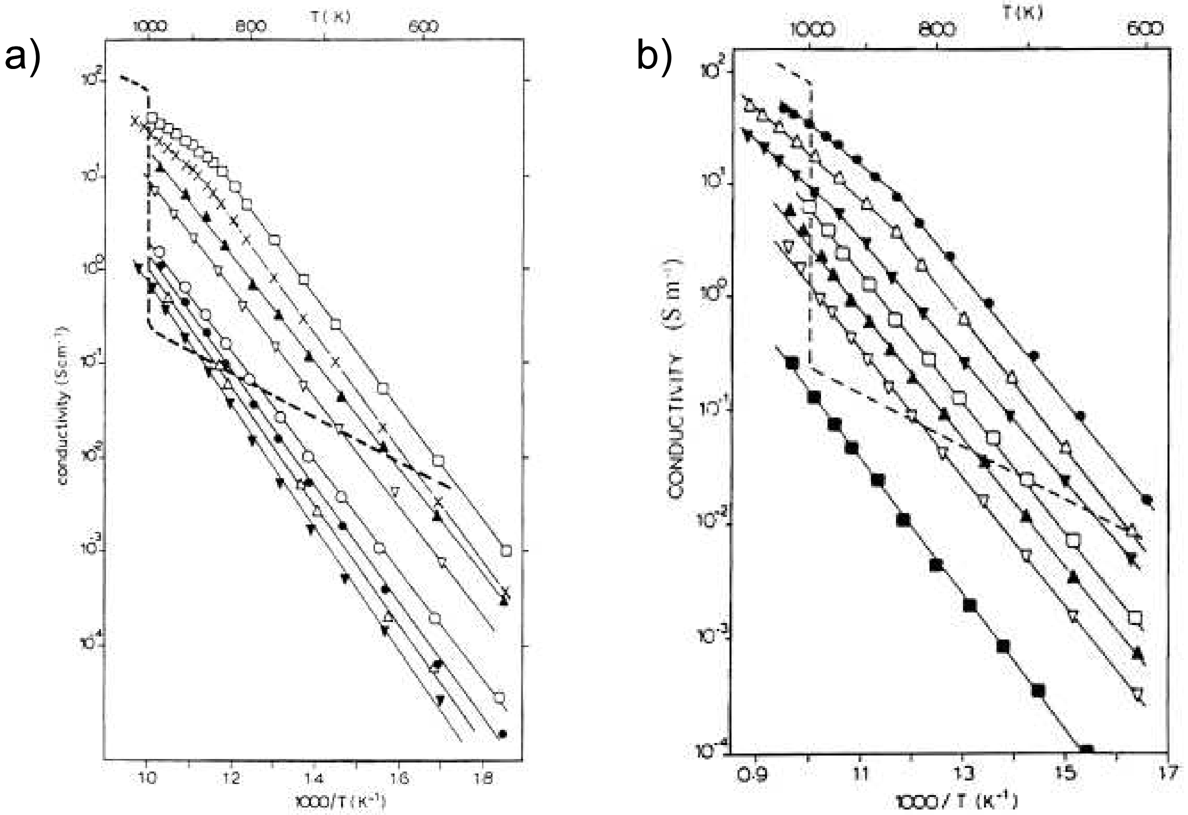

Fig.1.6 (a) Conductivity of $(Bi_2O_3)_{1-x}(Er_2O_3)_x$ in air[53]: (□) x=0.2, (X) x=0.25, (▲) x=0.3, (Δ)x=0.35, (○) x=0.4, (●) x=0.455, (+) x=0.5, (▼) x=0.6
(b) Conductivity of $(Bi_2O_3)_{1-x}(Dy_2O_3)_x$ in air[56]: (●) x=0.25, (+) x=0.285, (▼) x=0.35, (□) x=0.4, (▲) x=0.45, (Δ) x=0.5, (■) x=0.6;
the broken line corresponds to pure Bi_2O_3

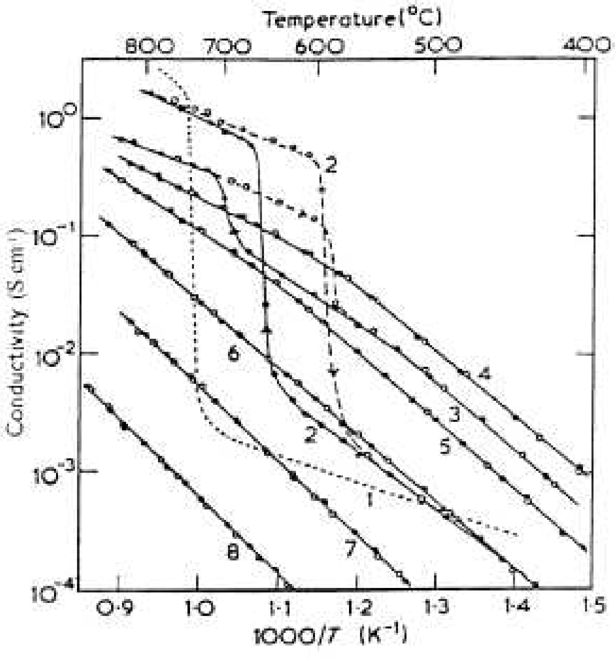

Fig.1.7 Conductivity of $(Bi_2O_3)_{1-x}(Y_2O_3)_x$ in air[7], the values for x are: 1=0, 2=0.05, 3=0.2, 4=0.25, 5=0.33, 6=0.425, 7=0.5, 8=0.6

For a given bismuth ratio and a given temperature, higher the lanthanide size, higher the conductivity. On the other hand, for a given lanthanide, an increase of conductivity is generally observed with the increase of bismuth content. This can be partly related to the higher polarizability of Bi^{3+} compared with that of doping element. The favorable effect of Bi^{3+} polarizability was verified using Pb^{2+} as dopant[24, 31].

The minimum concentration of dopant (x_{min}) required to "stabilize" the δ- phase in $Bi_2O_3 – Ln_2O_3$ systems was investigated by Verkerk and Burggraaf[56]. For Ln= Gd-Er, lower the lanthanide size, lower was x_{min}. The decrease of lanthanide size might lower the conductivity for a given lanthanide ratio; the decrease of x might increase the conductivity for a given lanthanide. These opposite influences result in a conductivity level increase, with Ln^{3+} radius lowering, for x_{min} value. These evolutions were presented for temperatures 500 and 700°C (Fig.1.8 a and b). Although Yb^{3+} exhibits the lower size of the lanthanides envisaged[53], it can not be included in the general evolution.

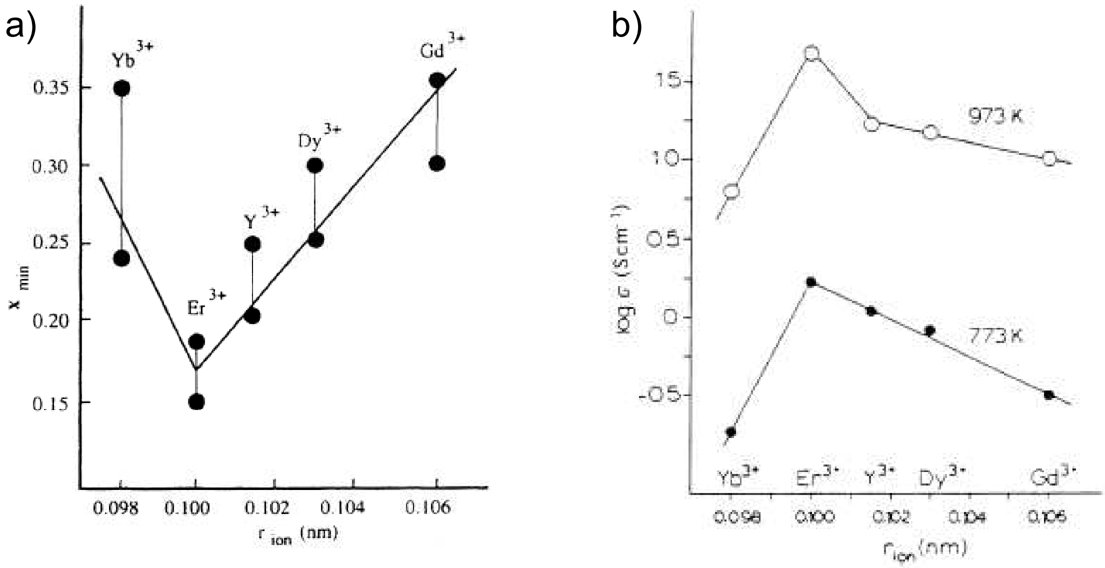

Fig.1.8 (a) x_{min} as a function of ionic radius (r_{ion}) of the dopant ion
(b) The conductivity of $(Bi_2O_3)_{1-x}(Ln_2O_3)_x$ for $x=x_{min}$ versus the ionic radius of the Ln^{3+} ion at 737K (filled circles) and 973K (open circles)[53]

Although no transformation of δ-phase is perceptible between the high temperature range of stability and the low temperature range including ambient, the conductivity exhibits two nearly Arrhenius behaviors with a change occurring in the range 450-550°C; this behavior was related to the short range ordering of oxygen atoms, at low temperature. A progressive decrease of the δ-conductivity, during a long time annealing below 600°C, was associated to a subtle modification evidenced from neutron diffraction studies. Various $Bi_{1-x}Er_xO_{1.5}$ samples ($0.25 \leq x \leq 0.30$) were investigated to link this aging to an ordering of the structure[38, 59-64]. The conductivity decay[38] was attributed to the appearance of a *bcc* superstructure, governed by the anions ordering ($Bi_5Ln_3O_{12}$-type phase).

In a recent paper[65], Nakayama examined, for some δ-type $Bi_{0.75}Ln_{0.25}O_{1.5}$ homologous ceramics (*Ln*=Dy, Ho, Er, Yb, and Y), the *Ln* size dependence of characteristics such as the crystalline lattice constant, the bulk density, the conductivity properties (σ and activation energy). As previously evidenced (Fig.1.6a), each Arrhenius plot revealed two linear domains with a breaking point around 550°C (Fig.1.9a, e.g. for *Ln*=Er). The conductivities at 500 and 700°C were almost constant while those at 300°C, slightly increased with an increase in the ionic radius of Ln^{3+}. The σ evolution distinguishes the Dy based sample with its highest conductivity (Fig1.9b), whereas the activation energies evolution distinguished the Er- sample with its lower association energy value and its higher migration energy value.

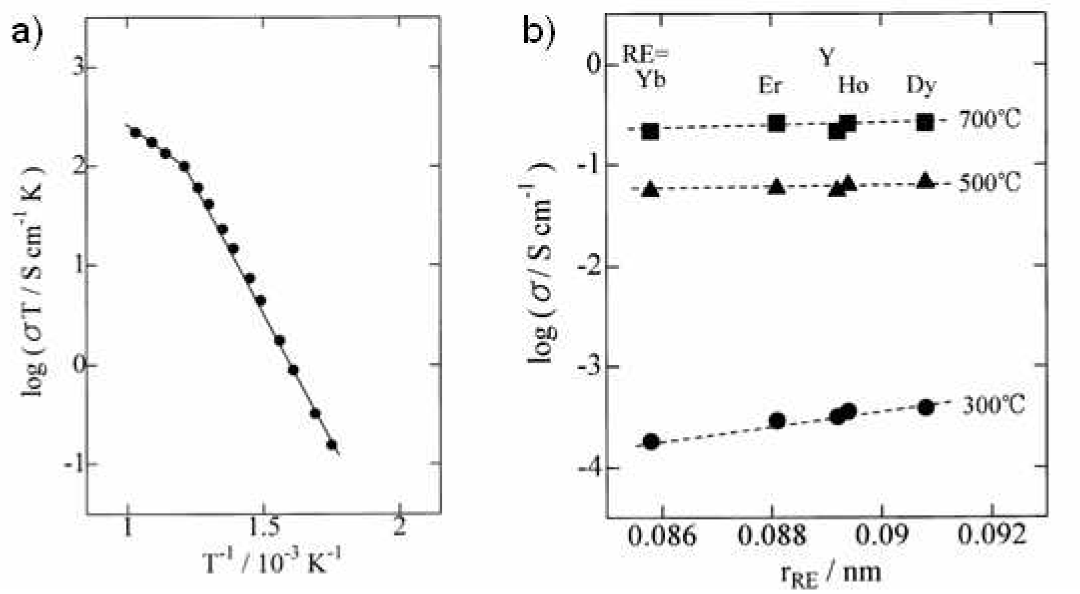

Fig.1.9 $Bi_{0.75}Ln_{0.25}O_{1.5}$ impedance spectrometry investigation of ceramics sintered at 1000°C[65]: (a) Arrhenius plot for *Ln*=Er; (b) Relationship between the ionic radius and the conductivity for *Ln*=Dy, Ho, Er, Yb, and Y.

From the point of view of conductivity, the best candidate would be $Bi_{0.825}Er_{0.175}O_{1.5}$ according to Verkerk and Burggraaf[56], whereas it would be the Dy containing sample within the $Bi_{0.75}Ln_{0.25}O_{1.5}$ series according to Nakayama[65]. In this composition range, the formation of rhombohedral Bi-Sr-O type phase can occur for Dy-([56]), Er-([27]) as well as for Y- containing sample[66], to which correspond the stoichiometric $Bi_7Ln_2O_{13.5}$ (x=0.222); that of an orthorhombic phase corresponding to $Bi_{17}Er_7O_{36}$([67]) can occur for x=0.292. However, it has already been shown that the kinetics of transformation could be slowed down by decreasing the grain size of ceramics.

1.2 Effect of grain size on the kinetics of phase transformation

The effect of grain size on phase transitions is well known. A typical example is the tetragonal–monoclinic phase transition in zirconia-based ceramics[68-70]. It was shown that the tetragonal form of zirconia which is stable above 1200°C, could be stabilized at room temperature by decreasing the grain size under 30nm. This was explained by excess surface energy, owing to the fact the high temperature form add a reduced surface energy with respect to the low temperature structure.

The effect of grain size on the kinetics of phase transition was more recently confirmed for composition $Bi_{26}Mo_9WO_{69}$[71] for which, at low temperature, higher conductivity was observed for ceramics sintered at lower temperature, with smaller grain size, in the range of 1μm (Fig.1.10).

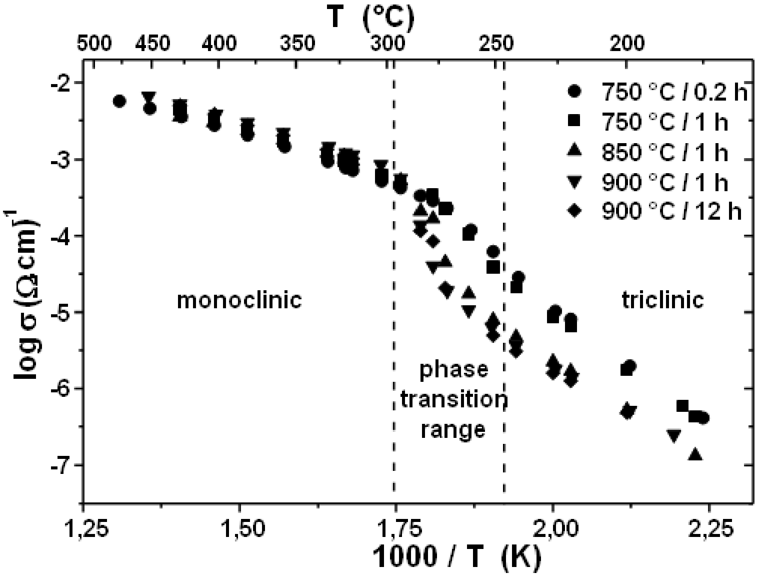

Fig.1.10 Arrhenius plots of the total electrical conductivity determined from the impedance diagram of $Bi_{26}Mo_9WO_{69}$ samples sintered at different temperatures with different grain sizes[71]

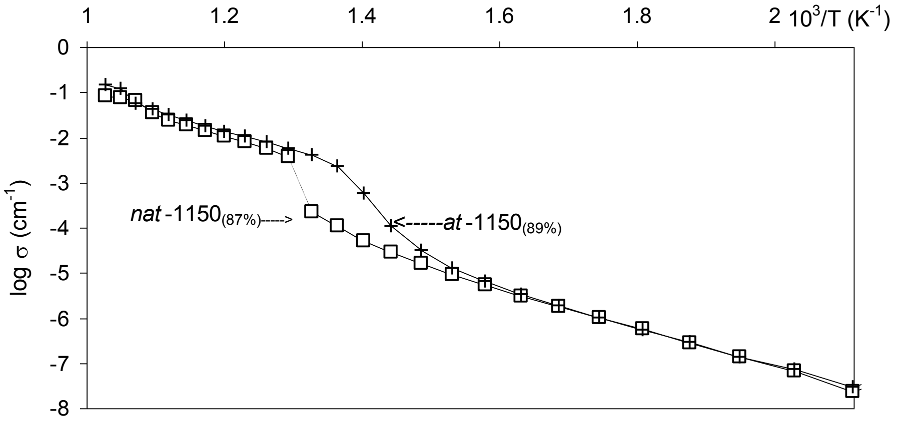

Fig.1.11 Arrhenius plots of the total electrical conductivity determined from the impedance diagram of $Bi_4La_2O_9$, samples prepared from attrition milled powder (small grain size) and non attrition milled powder (large grain size)[43]

The same behavior was observed for the rhombohedral Bi-Sr-O type phases in the Bi_2O_3-La_2O_3 system[43]. For composition $Bi_4La_2O_9$, the kinetics of transformation of the β_2 polymorph to a monoclinic polymorph (ε) were shown to be slowed down for ceramics prepared from attrition milled powder in respect to ceramics prepared from coarse powder (Fig.1.11).

In these latter studies, the increase of conductivity at low temperature was explained by the presence of the high temperature polymorph at low temperature but, according to some authors, a decrease of the grain size of ceramics could also lead to an increase of their conductivity.

1.3 Effect of ceramic grain size on conductivity

In recent years, based on nano technology, reducing the grain size to nanoscale has received more attentions as another way to stabilize phases and further to enhance the properties. It is considered that developing nanoceramics as solid electrolyte is an effective way to improve strength and toughness, and also other properties. For example, nano oxygen sensor exhibits superior properties to conventional sensor: they could work at 300°C compared to micro sensor at 800°C[72, 73]. This is explained by the fact that nano-materials display more interfaces which provide the channel for ion mobility.

The total conductivity of a solid electrolyte includes bulk conductivity and grain boundary conductivity. One model employed to correlate the microstructure with the bulk and grain boundary conductivity is the brick-layer model (Fig.1.12). In this model, it is assumed that the ceramic samples consist of grains with high conductivity, separated by relatively thin, uniform grain boundaries.

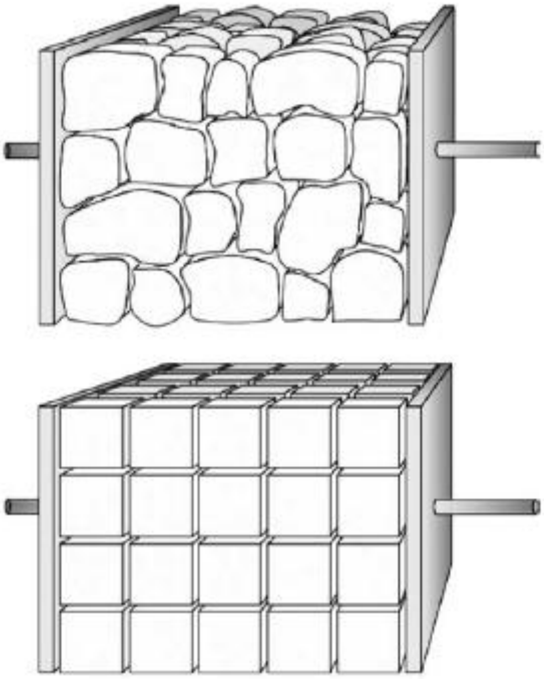

Fig.1.12 Real ceramic microstructure and brick layer model

It is well known that, in polycrystalline ceramic materials, grain boundaries often have a significant influence on overall properties. In many polycrystalline materials grain boundaries provide a region of relatively rapid mass transport compared to the bulk properties of the crystallites. However, in zirconia- or ceria-based electrolytes the grain boundaries have a lower effective charge carrier concentration and thus results in highly resistive grain boundary phase. In materials of usual purities, the grain-boundary effect has been largely attributed to the existence of second phase, consisting mainly of Si, Al, Mg and Ca impurities, in the grain-boundary.

However, in high purity materials with clean grain boundaries, it was also found that the specific grain-boundary conductivity is significantly lower than the bulk conductivity[74, 75]. Therefore, an “intrinsic” grain boundary blocking effect was suggested[74]. A grain boundary consists of one grain boundary core and two adjacent space-charge layers[76], as shown in Fig.1.13(a). Owing to the charged grain-boundary core, the concentrations of charged point defects in the space-charge layer deviate from their bulk values. As demonstrated by Maier[76, 77] and Waser[78, 79], the accumulation or depletion of charge carriers in the space-charge layer significantly influences the electrical properties of polycrystalline ionic and mixed conductors.

In ZrO_2 and CeO_2 based materials, the oxygen vacancy depletion in the space charge layers was proposed to be the cause for the intrinsic blocking effect.

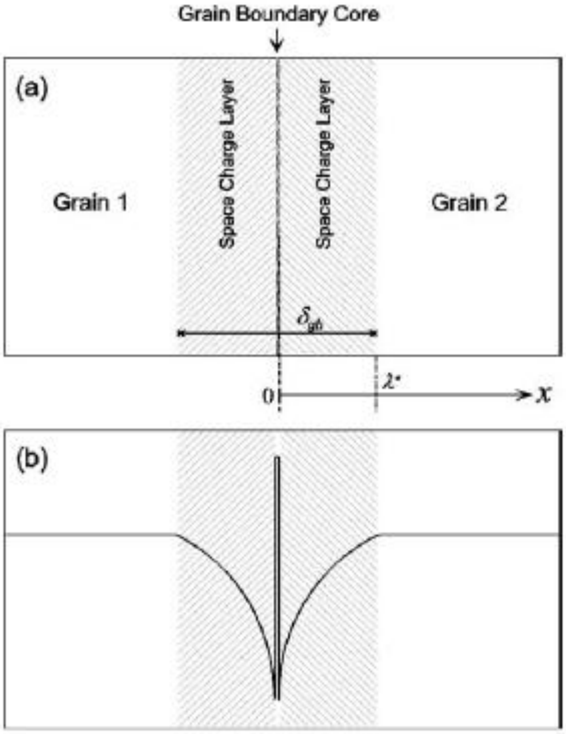

Fig.1.13 (a) Schematic representation of an "electrical grain boundary", consisting of one grain-boundary core and two adjacent space-charge layers. At the interface between the space-charge layer and the grainboundary core x = 0, while far into the bulk x =∞. (b) Schematic representation of oxygen vacancy profiles in space-charge layers and grain-boundary core[80].

There are many reports to confirm the effect of grain size on conductivity of polycrystalline material. Youngblood[81] and Virkar[82] measured the conductivity of Li_2O stabilized Beta-Al_2O_3 samples which had the same composition. It was found that when the grain grew from 2μm to 100μm, the electrical resistivity lowered from 4.80Ω.cm to 2.81Ω.cm at 300°C. Gordon[83] further point that the decrease in electrical resistivity with grain growth could be visibly observed only when the grain size was lower than 5μm. Otherwise, Moghadam[84], Inoffe[85], Verkerk[86] and Yanagida[87] *et al.* studied ZrO_2-base material with different components, the results showed that the ion conductivity of the sample decreased with the decrease of grain size.

All the researches above focused on microcrystalline material, but many researchers have investigated the grain size dependence of conductivity in nanocrystalline solid electrolytes and agreed that a beneficial grain size effect could be observed when grain size is below 100nm. The group of Heitjans[88] has reported that the ion conductivity of nanocrystalline CaF_2 was 3 orders of magnitude higher than for single crystal at 390-500K, and activation energy of the ionic conduction was lower. It was also found that in Li_2SO_4-Al_2O_3 composite material, the ion conductivity increased when the grain size was lowered to 10nm[89]. Ramasamy[90] et al obtained for the 12mol% Y_2O_3 stabilized ZrO_2, higher conductivity for nanocrystalline ceramics than for microcrystalline sample. For CeO_2 with 10nm grain size, the same phenomenon was observed[91]. Suzuki Toshibo[92] *et al.* studied CeO_2-based materials; it was found that in pure CeO_2, electronic conductivity increased with the decrease of grain size, but in Gd^{3+} doped CeO_2, the ionic conductivity increased. The study of Tschope[93] showed that nanocrystalline CeO_2 was found to be electronically conductive while microcystalline CeO_2 exhibited predominantly ion conduction in the same conditions. The electronic conductivity of nanocrystalline CeO_2 was higher than for single crystal, and increased when the size of grains decreased.

Based on the brick-layer model, assuming that all the grains are cubic with equal size of d_g, the grain size is much bigger than grain boundary thickness, δ_{gb}, and that the contribution to the conductivity parallel to the grain boundaries is negligible, the specific grain boundary conductivity can be estimated by the following equation[74].

$$\sigma_{gb}^{sp} = \sigma_{gb} \frac{\delta_{gb}}{d_g} \tag{1.1}$$

In their report on tetragonal zirconia, Guo *et al*[94], showed that the specific grain boundary conductivity increased when the grain size decreased. As shown in Fig.1.14, bulk conductivity doesn't change too much when grain size decreased to the nanoscale, but grain boundary conductivity could increase by 1-2 orders of magnitude.

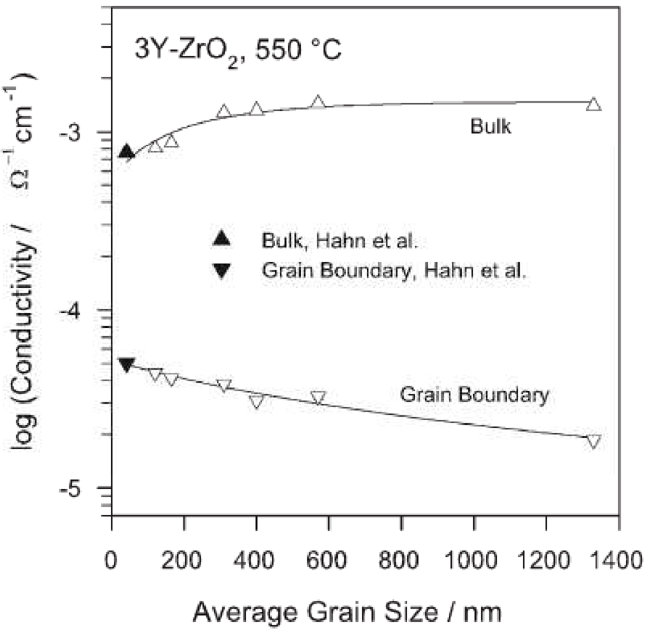

Fig.1.14 Bulk conductivities and specific grain boundary conductivities for 3mol%Y_2O_3 doped ZrO_2 at 550°C as a function of average grain size [94]

This increase can be explained by the space charge layer model. By assuming the oxygen vacancies depletion in the vicinity of grain boundaries, a Schottky barrier model can explain most of grain boundaries features.

In space charge layers, the magnitude of the depletion can be quantified by using the potential barrier height Δϕ(0) defined as the difference between the electric potential at grain boundaries and the electric potential within the volume of grains, which can be expressed as fellows:

$$E_a^{gb} - E_a^{bulk} = (2e\Delta\phi(0) - k_B T)\left[1 + \frac{1}{T\Delta\phi(0)}\frac{d\Delta\phi(0)}{d(1/T)}\right] \qquad (1.2)$$

where E_a^{bulk} and E_a^{gb} are the activation energy of grain interior and grain boundary, Δϕ(0) is the Schottky barrier height. As E_a^{bulk} is independent of Δϕ(0), the activation energy for the grain-boundary conductivity, E_a^{gb}, is thus determined by the Schottky barrier height Δϕ(0). It could be found in the studies above that the Δϕ(0) decreased with decrease of grain size, and it also indicated that the concentration of oxygen vacancies in the space-charge layers increased with decrease of grain size. As a result, the specific grain boundary conductivity increased with decrease of grain size.

However, even if the specific grain boundary conductivity increased with decrease of grain size, it was still 1-2 orders magnitude lower than the grain interior. Thus the higher the volume fraction of grain boundaries in a sample (the smaller the grain size), the lower would be the total conductivity.

The idea of a beneficial effect of grains with size at the nanoscale is not shared by all the community. Ponpandian[95] found that for zinc ferrite when the grain size decreased from 115nm to 7nm, the conductivity decreased. Bertini[96] also reported that for $CoSb_3$, when the grain size decreased to the nano scale, the thermal conductivity was lowered by 1 order of magnitude, and ion conductivity also decreased.

The bulk and grain-boundary electrical properties as a function of grain size were studied in ZrO_2-based materials. The research on 3mol%Y_2O_3 - ZrO_2[94], 8mol%Y_2O_3 -ZrO_2[86, 97, 98], 8mol% Sc_2O_3 -ZrO_2[99] and 15mol% CaO-ZrO_2[74] showed that the grain-boundary conductivity decreased with the decrease of grain size.

1.4 Conclusion

Although their sensitivity toward reduction, bismuth based compounds remains challenging materials for the high oxide ion conductivity. With a conductivity of $1 S.cm^{-1}$, δ-Bi_2O_3 is the pragmatic limit of conductivity one can expect in oxide ion solid state electrolyte. In the Bi_2O_3-Ln_2O_3 systems, from the point of view of conductivity, the metastable δ-phases clearly exhibit the most promising properties. They appeared to be metastable but, by decreasing the grain size of ceramics, one can expect a better stability. Moreover, a decrease of the grain size could have a beneficial impact on the conductivity, although such an impact is still subject at controversy. With the aim to stabilize the δ form, in the following of this study, ceramics with small grain size were prepared. The lanthanide ratio x=0.25, which occupies a quasi central position in the 0.222-0.292 domain, appears well adapted to prevent the transformation of Dy- as well as that of Er- based δ- phases. The preparation of $(Bi_2O_3)_{0.75}(Ln_2O_3)_{0.25}$ nanopowders with Ln=Dy, Er, Y, was therefore optimized before the preparation of dense ceramics with nano grain size.

References

[1] Sillen LG. *Naturwissenschaften*, 1940, **28**: 206.

[2] Sillen LG. *Zeitschrift für Kristallographie,* 1941, **A103**: 274.

[3] Malmos G. *Acta Chemica Scandinavi,* 1970, **24**: 384.

[4] Malmos G, Thomas JO. *J. Appl. Crystallogr.*, 1977, **10**: 7.

[5] Cheetham AK, Taylor JC. *J. Solid State Chem.,* 1977, **21**: 253.

[6] Harwig HA, Weenk JW. *Zeitschrift für Anorganishe and Allgemeine Chemie,* 1978, **444**: 167.

[7] Takahashi T, Iwahara H. *Mater. Res. Bull.*, 1978, **13**: 1447.

[8] Ivanov SA, Tellgren R, Rundlof H, Orloy VG. *Powder Diffr.*, 2001, **16**: 227.

[9] Drache M, Roussel P, Wignacourt JP. *Chem. Rev*., 2007, **107**: 80.

[10] Gattow G, Schroder H. *Zeitschrift für Anorganishe and Allgemeine Chemie*, 1962, **318**: 176.

[11] Yashima M, Ishimura D. *Chem. Phys. Lett.,* 2003, **378**: 395.

[12] Levin EM, Roth RS. *Journal of Research of National Bureau of Standards-A*, 1964, **68A**: 197.

[13] Blower SK, Greaves C. *Acta Crystallogr., C*, 1988, **44**: 587.

[14] Harwig HA, Gerards AG. *Thermochimica Acta*., 1979, **28**: 121.

[15] Harwig HA. *Zeitschrift für Anorganishe and Allgemeine Chemie,,* 1978, **444**: 151.

[16] Radaev SF, Simonov VI. *Kristallografiya*, 1992, **37**: 914.

[17] Cornei N, Tancret N, Abraham F, Mentre O. *Mentre, Inorg. Chem. (Communication),* 2006, **45**: 4886.

[18] Gualtieri AF, Immovilli S, Prudenziati M. *Powder Diffr.,* 1997, **12**: 90.

[19] Harwig HA, Gerards AG. *J. Solid State Chem.,* 1978, **6**: 265.

[20] Drache M, Huve M, Roussel P, Conflant P. *Mater. Res. Bull.,* 2003, **38**: 113.

[21] Drache M, Roussel P, Wignacourt JP, Conflant P. *Mater. Res. Bull.,* 2004, **39**: 1393.

[22] Watanabe A. *Solid State Ionic*, 1996, **86-88**: 1427.

[23] Hirosaki N, Ogata S, Kocer C. *J. Alloys and Compd.,* 2003, **351**: 31.

[24] Watanabe A. *J Solid State Chem*., 1990, **40-41**: 889.

[25] Chen XL, Zhang FF, Shen YM, Liang JK, Tang WH, Tu QY. *J. Solid State Chem.*, 1998, **139**: 398.

[26] Verkerk MJ, Keizer, K. and Burggraaf, AJ. *J.Appl. Electrochem.*, 1980, **10**: 81.

[27] Conflant P, Follet-houttemane C, Drache M. *J. Mater. Chem.*, 1991, **1**: 649.

[28] Takahashi T, Iwahara H, Arao T. *J. Appl. Electrochem.*, 1975, **5**: 187.

[29] Iwahara H, Esaka T, Stao T, Takahashi T. *J. Solid State Chem.*, 1981, **39**: 173.

[30] Omari M, Drache M, Conflant P, Boivin JC. *Solid State Ionic,* 1990, **40-41**: 929.

[31] Omari M. Lille University 1989.

[32] Portefaix N, Conflant P, Boivin JC, Wignacourt JP, Drache M. *J .Solid State Chem.*, 1997, **134**: 219.

[33] Mercurio D, Farisi MEI, Frit B, Reau JM, Senegas J. *Solid State Ionic*, 1990, **39**: 297.

[34] Benkaddour M, Omari M, Boivin JC, Conflant P, Drache M. *Ann Chim Sci Mat*., 2000, **25**: S165.

[35] Battle PD, Catlow CRA, Drennan J, Murray AD. *J. Phys. C: Solid State Phys*., 1983, **16**: 561.

[36] Verkerk MJ, Van de Velde, Burggraaf AJ, Helmoldt RB. *J. Phys. Chem. Solid.,* 1982, **43**: 1129.

[37] Battle PD, Catlow CRA, Heap JW, Moroney LM. *J. Solid State Chem*., 1986, **63**: 8.

[38] Jiang N, Buchanan RM, Stevenson DA, Nix WD, Li JZ, Yang JL. *Mater Let*., 1995, **22**: 215.

[39] Ito Y, Mukovama T, Mori H, Koto K. *Solid State Ionic*, 1995, **79**: 81.

[40] Koto K, Mori H, Ito Y. *Solid State Ionic*. 1986, **18**: 720.

[41] Sooryanarayana K, Somashekar R, Row TNG. *Solid State Ionic,* 1997, **104**: 319.

[42] Benkaddour M, Obbade S, Conflant P, Drache M. *J. Solid State Chem*., 2002, **163**: 300.

[43] Drache M, Djelal N, Steil MC, Roussel P, Conflant P. *Mater. Res. Bull.,* 2005, **40**: 599.

[44] Turkoglu O, Altiparmak F, Belenli I. *Chem Pap*., 2003, **5**: 304.

[45] Jingling Y, Jingkui L, Weihua T, Ying S, Xiaolong C, Guanghui R. *J. Alloys Compd.*, 1997, **252**: 143.

[46] Turkoglu O, Soylak M. *Asian J Chem.*, 2002, **14**: 1698.
[47] Turkoglu O, Soylak M, Belenli I. *Bull Mat Sci.*, 2002, **25**: 583.
[48] Zargarova MI, Akhmedoya NA, Kuli-zade ES, Mustafaev NM. *Zh Neorg Khimii*, 1995, **40**: 1389.
[49] Ducke J, Troemel M, Hohlwein D, Kizler P. *Acta Crystallogr., C*, 1996, **52**: 1329.
[50] Kruidhof H, Bouwmeester HJM, De Vries KJ, Gellings PJ, Burggraaf AJ. *Solid State Ionic*, 1992, **50**: 181.
[51] Kruidhof K, De Vries KJ, Burggraaf AJ. *Solid State Ionic*, 1990, **37**: 213.
[52] Esaka T, Iwahara H. *J Appl Electrochem.*, 1985, **15**: 447.
[53] Keizer K, Verkerk MJ, Burggraaf AJ. *Ceramurgia International*, 1979, **5**: 143.
[54] Shuk P, Jakobs S, Mobius HH. *Z Anorg Allg Chem.*, 1985, **524**: 14.
[55] Takahashi T, Esaka T, Iwahara H. *J Appl Electrochem.*, 1975, **5**: 197.
[56] Verkerk MJ, Burggraaf AJ. *J Electrochem.*, 1981, **128**: 75.
[57] Benkaddour M, Conflant P, Drache M, Steil MC. *Solid State Ionics*, 2002, **146**: 175.
[58] Benkaddour M, Steil MC, Drache M, Conflant P. *J Solid State Chem.*, 2000, **155**: 273.
[59] Fung KZ, Virkar AV. *J Am Ceram Soc.*, 1993, **76**: 2403.
[60] Fung KZ, Baek HD, Virkar AV. *Solid State Ionic*, 1992, **52**: 199.
[61] Jiang N, Buchanan RM, Henn FEG, Marshall AF, Stevenson DA, Wachsman ED. *Mater Res Bull.*, 1994, **29**: 247.
[62] Stevenson DA. *An EPRI/GRI Fuel Cell Workshop,* San Francisco: CA 1992.
[63] Wachman ED, Ball GR, Mason DM, Stevenson DA. *Solid State Ionic*, 1992, **52**: 213.
[64] Wachman ED, Jiang N, Mason DM, Stevenson DA. *Proc Electrochem. Soc.*, 1989, **89**:15.
[65] Nakayama S. *Ceram. Int.*, 2002, **28**: 907.
[66] Drache M, Obbade S, Wignacourt JP, Conflant P. *J Solid State Chem.*, 1999, **142**: 349.
[67] Watanabe A. *Solid State Ionic,* 2005, **176**: 2423
[68] Subbarao. EC. In: Hobbs AHHaLW, (ed.). Columbus, OH, USA The American Ceramic Society 1981; 1.
[69] Garvie RC. *J Phys Chem Solids*, 1965, **69**(4): 1238.
[70] Garvie RC. *J Phys Chem Solids*, 1978, **82**(2): 218.
[71] Fonseca FC, Steil MC, Vannier RN, Mairesse G, Muccillo R. *Solid State Ionics*, 2001, **140**: 161
[72] Ferrari. A. Development, Industrialization of Nanocomposite Ceramic Material, Proceedings of anostructure Materials and Coating' 95, Atlanta Airport Marriott. *Atlanta, Georgia, USA*. 1995.
[73] Boulc'h F, Dessemond L, Djurado E. *Solid State Ionics,* 2002, **154/155**: 143.
[74] Aoki M, Chiang YM, Kosacki I, Lee LJR, Tuller H, Liu Y. *J Am Ceram Soc.*, 1996, **79**: 1169.
[75] Tian CY, Chan SW. *Solid State Ionic*, 2000, **134**: 89.
[76] Maier J. *Ber Bunsenges Phys Chem.*, 1986, **90**: 26.
[77] Maier J. *J. Prog. Solid State Chem.*, 1995, **23**: 171.
[78] Holbling T, Waser R. *J. Appl. Phys.*, 2002, **91**: 3037.
[79] Waser R, Hagenbeck R. *Acta Mater.*, 2000, **48**: 797.
[80] Guo X, Waser R. *Prog. Mater Sci.*, 2006, **51**: 151.
[81] Youngblood GE, Miller GR, Gordon RS. *J. Am. Ceram. Soc.*,1978, **61**: 86.
[82] Virkar AV, Miller GR, Gordon RS. *J. Am. Ceram. Soc.*, 1978, **61**: 250.
[83] Gordon RS. Processing of polycrystalline Ceramic. Plenum Press, *New York and London*, 1977: 405.
[84] Moghadam FK, Stevenson DA. *J. Am. Ceram. Soc.*, 1982, **65**: 213.
[85] Inoffe AI, Inozemtsev MV, Lipilin AS, Perfilev MV, Karpachov SV. *Physica Status Solidi (a)* 1975, **30**(1): 87.
[86] Verkerk MJ, Middelhuis BJ, Burggraaf AJ. *Solid State Ionic,* 1982, **6**: 159.
[87] Yanagida H, Takata M, Nagai M. *J. Am. Ceram. Soc.,* 1981, **64**: c-34.
[88] Puin W, Heitjans P. *Nanostructured Materials,* 1995, **6**: 885.
[89] Uvarov NF, Bokhonov BB, Isupov VP, Hairetdinov EF. *Solid State Ionics,* 1994, **74** 15.
[90] Ramamoorthy R, Viswanath RN, Ramasamy S. *Nanostructured Material,* 1995, **6**: 337.

[91] Lavik EB, Chiang YM. *Nanophase and Nanocomposite Materials II Symposium,* Boston, MA, USA: part of the (Nanophase and Nanocomposite Materials II. Symposium), Mater. Res. Soc., 1996, 63.

[92] Suzuki T, Kosacki I, Anderson HU. *SSP-2000*, Tokyo, Japan: part of the Solid State Ionics, Elsevier Science 2000, 111.

[93] Tschope AS, Sommer E, Birringer, R. *Solid State Ionics, Diffusion Reactions (Solid State Ion Diffus React (Netherlands))*, 2001/02, **139**: 255.

[94] Guo X, Zhang Z. *Acta Materialia,* 2003, **51**: 2539.

[95] Ponpandian N, Narayanasamy A. *J. Appl. Phys.,* 2002, **92**(5): 2770.

[96] Bertini LB, K.;Christensen, M.etal. *Proceedings ICT'03 22nd International Conference on Thermoelectric,* La Grande Motte, France: part of the (Proceedings ICT'03. 22nd International Conference on Thermoelectrics (IEEE Cat. No.03TH8726)), IEEE, 2003, 93.

[97] Verkerk MJ, Winnubst AJA, Burggraaf AJ. *Solid State Ionics,* 1982, **6**(2): 159.

[98] Boulfrad S, Djurado E, Dessemond L. *Fuel Cells,* 2008, **5**: 313.

[99] Xu G, Zhang YW, Liao CS, Yan CH. *Solid State Ionics,* 2004, **166**: 391.

Chapter 2

Preparation and characterization of Bi_2O_3-Ln_2O_3 (Ln=Y, Er, Dy) nano powders

There are several methods to prepare oxide ceramics. Solid state reaction from the reaction of mixed oxides, carbonates, hydroxides or salts is one of the most common and easier methods. The mixture is usually heated at temperature at least equal to the 2/3 of the melting point temperature (^{o}C), for period up to 10 hours. It is easy to operate, but several grindings and annealings are usually needed to obtain phase of good purity. Moreover powders with coarse grains are usually obtained which renders sintering difficult, thus a reduction of particle size is needed. This reduction can be achieved by attrition milling but this has an energetic cost.

Hydrothermal, sol-gel or co-precipitation routes are usually preferred to obtain powder with small grain size. The sol-gel method is widely used to prepare Bi_2O_3-based thin films. Chen *et al.*[1] obtained superfine Bi_2O_3 particle using $Bi(OCH_2CH_2OCH_3)$ and $Bi(OCMe_2Et)_3$ as precursors. The particles were spheric with a size distribution between 60-120nm after calcination at 420^{o}C. Bi_2O_3 nano- powders were also prepared by spray combustion of metal inorganic salts dissolved in glacial acetic acid ($C_2H_4O_2$) [2]. Oxygen was used as the oxidant and dispersion gas, and its flow rate was controlled to maintain a constant pressure decrease of 1.5 bar at the nozzle tip. Premixed methane/oxygen gas flowed through the supporting flamelets at a total flow rate of 2.96 L/min (The CH_4 flow rate was 1.58 L/min, and the O_2 flow rate was 1.38 L/min). An oxygen sheath flow (5 L/min) was supplied through a sintered metal plate ring.

With the aim to prepare dense ceramics with grain size at the nanoscale, in the present study, co-precipitation was preferred for the preparation of nano-powders. In a first step the composition corresponding to $(Bi_2O_3)_{0.75}(Ln_2O_3)_{0.25}$ with Ln=Dy, Y, Er were selected, the mixed compound $(Bi_2O_3)_{0.75}(Er_2O_3)_{0.125}(Y_2O_3)_{0.125}$ was also prepared. The preparation was first optimized for composition $(Bi_2O_3)_{0.75}(Dy_2O_3)_{0.25}$ and then applied to the other compositions.

2.1 Preparation by co-precipitation

Co-precipitation is considered as one of the most effective methods to prepare nano-powders. In this method, an aqueous solution containing the desired cations is mixed with another solution acting as a precipitation agent. Strong base, weak base and organic acid can be chosen as precipitant. Usually, filtration, drying and thermal decomposition followed to obtain the desired products whose physical properties can be controlled by adjusting the pH of the solution, the mixing rate, the concentration and temperature. Using this method, the control of morphology, purity and composition is good, although different precipitation rate may sometimes result in inhomogeneity.

There were several attempts to prepare Bi_2O_3 powders using this technique. β-Bi_2O_3 with particle size of 1-10μm was successfully obtained by Wang *et al.* [3]. A 30% NaOH solution was added as precipitant until a pH of 12. During the precipitation process the solution was kept at 70~90°C with a stirring rate of 300r/min. In these conditions, the following reactions happen gradually in the nitrate solution:

$$Bi^{3+} + NO_3^- + H_2O = BiONO_3\downarrow + 2H^+ \tag{2.1}$$

$$BiONO_3 + OH^- + H_2O = Bi(OH)_3\downarrow + NO_3^- \tag{2.2}$$

$$H_3BiO_3 + OH^- = BiO_2^- + 2H_2O \tag{2.3}$$

$$2BiO_2^- + 2H_2O = 2OH^- + Bi_2O_3\downarrow \tag{2.4}$$

Sun *et al.* [4] prepared Bi_2O_3 nano-powder by a two step hydrolysis method: first, at 40-60°C, a NaOH solution was added into a bismuth nitrate solution to adjust the pH at 3-5, the precipitate was washed and filtered to obtain $BiONO_3$; second, at 50-60°C, NaOH was dropped into the slurry of $BiONO_3$ with a certain amount of dispersant until the pH value reached 13-14, the solution was then stirred until the complete reaction. The obtained powder was α-Bi_2O_3 with a particle size of 50-70nm and good particle dispersion.

Shi *et al.* [5] prepared Bi_2O_3 nano-powder with an average particle size of 20nm using ammonia solution as precipitant to avoid the introduction of cationic impurity. Indeed, NH_4^+ decomposes to gas at 200-300°C, which is perfect for the preparation of high purity powder. In these conditions, the following reactions using ammonia as precipitant occur:

$$Bi^{3+} + NO_3^- + H_2O = BiONO_3\downarrow + 2H^+ \tag{2.5}$$

$$BiONO_3\downarrow + NH_3(aq) + 2H_2O = Bi(OH)_3\downarrow + NH_4^+ + NO_3^- \tag{2.6}$$

$$Bi(OH)_3\downarrow + NH_3(aq) = BiOOH\downarrow + NH_4^+ + OH^- \tag{2.7}$$

The total reaction equations are:

$$Bi^{3+} + 3NH_3(aq) + 2H_2O = BiOOH\downarrow + 3NH_4^+ \tag{2.8}$$

$$2BiOOH\downarrow + NH_3(aq) = Bi_2O_3\downarrow + NH_4^+ + OH^- \tag{2.9}$$

There are also reports which introduce the organic acid as precipitant. The process is similar to the two mentioned above, but organic acid may avoid the intermediate products in the hydrolysis like $BiONO_3$ and could be helpful to refine the particle size and obtain uniform particles. Santos *et al.* [6] prepared Bi-Sr-Ca-Cu-O and (Bi, Pb)-Sr-Ca-Cu-O composite powders using this method, and fabricated semiconductor materials. These composite powders were prepared from acetate of all the metal which were dissolved in glacial acetic acid, once the solution was stable, excessive amount of ethane diacid was added until the complete precipitation. After filtration and heat treatment, a superfine Bi_2O_3 powder could be obtained.

As mentioned above, when ammonia is added drop by drop into the metallic ion solution (forward titration process), $BiONO_3$, BiOOH, $Bi(OH)_3$ and Bi_2O_3 can precipitate one by one with the pH value increase.

The $\log C_{(Bi)}$-pH diagram of Bi^{3+}-NO_3-H_2O system (Fig.2.1) was given by Wang *et al* [7]. It shows the overlapped diagram of species at equilibrium in solution of $BiONO_3$, $Bi(OH)_3$, Bi_2O_3 and BiOOH.

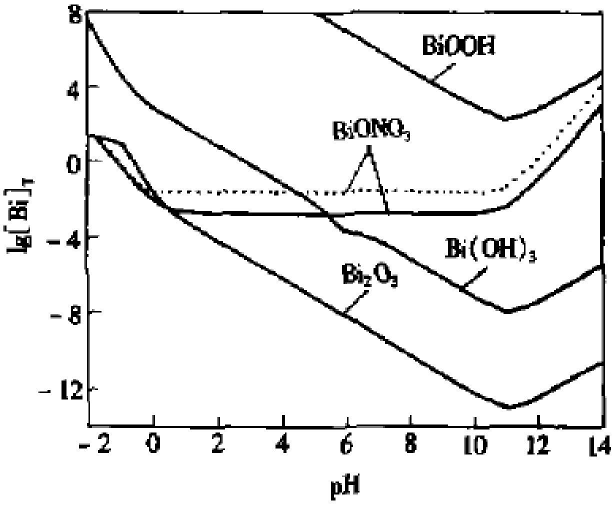

Fig.2.1 $\log C_{(Bi)}$-pH diagram in Bi^{3+}-NO_3-H_2O system[7]

– —$c_0(NO_3\text{-})=3.0\ mol.L^{-1}$; ··· —$c_0(NO_3\text{-})=0.3\ mol.L^{-1}$

From Fig.2.1, within these four solids, the most stable phase is Bi_2O_3. It should precipitate at very low pH. $Bi(OH)_3$ is also rather stable whereas BiOOH appears to be less stable. The possibility of $BiONO_3$ precipitation cannot be discarded, however its solubility is lowered at pH higher than 11. In this system, it is also worth noting that changes of $c_0(Bi^{3+})$ and $c_0(NO_3^-)$ have little effect on the equilibrium of $Bi(OH)_3$, BiOOH and Bi_2O_3-solution. However, from the point of view of dynamics, with the increase of pH, the extent of transformation may influence the purity of Bi_2O_3, and the actual product may also be a mixture of Bi_2O_3, $BiONO_3$ and $Bi(OH)_3$.

To avoid the formation of $BiONO_3$, a reversing-titration method was applied to keep the solution at high pH. He *et al.* [8] prepared nano-Bi_2O_3 powder by this method using ammonia as precipitant, and found the precipitate was mainly BiOOH (instead of $Bi(OH)_3$) with little Bi_2O_3. This is the method we chose for the preparation of the Bi_2O_3-based nano-powders.

2.2 Thermodynamic equilibrium in the titration process

To confirm which products would form by using the reverse chemical titration method, the equilibrium of all the components in solution was calculated.

The standards Gibbs free energies of all the components in the aqueous solution are given in Table 2.1. Only Dy and Y were considered as Bi substituents. Besides $BiONO_3$, the existence of $DyONO_3$, $Bi_5O_7NO_3$ and mixed oxy-nitrates $MBi_2O_4NO_3$ (M=Y, Sm, Eu, Gd, Tb, Dy, Er, Yb) have also been reported [9]. However, these species could not be taken into the calculation, because of shortage of Δ_fG^0.

Table 2.1 Δ_fG^0 of the related species of Bi, Dy, Y in aqueous solution[10]

	Δ_fG^0/(kal·mol^{-1})		Δ_fG^0/(kal·mol^{-1})		Δ_fG^0/(kal·mol^{-1})
Bi_2O_3	-118.809	**Dy_2O_3**	-423.320	**Y^{3+}**	-163.788
$Bi(OH)_3$	-136.995	**$Dy(OH)_3$**	-325.136	**YO^+**	-198.99
Bi^{3+}(a)	22.851	**Dy^{3+}(a)**	-158.669	**YO_2^-**	-277.355
BiO^+(a)	-29.298	**DyO^+(a)**	-202.377	**YOH^{2+}**	-209.927
BiO_2^-(a)	-61.729	**DyO_2^-(a)**	-221.611	**H_2O**	-56.741
$BiOH^{2+}$(a)	-32.290	**$DyOH^{2+}$(a)**	-205.255	**OH^-**	-46.434
$HBiO_2$(a)	-79.261	**DyO_2H(a)**	-238.141	**NO_3^-**	-26.489
BiOOH	-88.0	**Y_2O_3**	-43.061		
$BiONO_3$	-67.0	**$Y(OH)_3$**	-305.37		

Fig.2.2 gives the relationship between the pH value and precipitates of Bi^{3+}, Dy^{3+} and Y^{3+} at 25°C and at 1 atm. In this case, there was no valence change of ions, it meant that the reactions were independent of the electrochemical potential (Eh), but only dependent on pH. Therefore, only the dependence with pH will be discussed.

The calculations were performed according to two scenarios. In the first scenario (at the initial stage), concentrations of Bi^{3+}, Dy^{3+} and Y^{3+} were 0.075mol/L 0.0025mol/L and 0.025mol/L, respectively. In the second scenario (at the end of the reaction), it was assumed the concentrations of Bi^{3+}, Dy^{3+} and Y^{3+} were all lower than 10^{-5} mol/L.

From these diagrams, $BiONO_3$ would form only at pH lower than 6.3, in good agreement with Wang *et al.*[7] results. However, at higher pH value, the predominant specie would be BiOOH. For Dy^{3+}, the pH value at which $Dy(OH)_3$ would form increases when the concentration decreases, but it would form at pH value higher than 2.5, even for very low concentrations. In case of Y^{3+}, it is more complex, other ion would occur in the solution with lower concentration, and the window of stability of $Y(OH)_3$ would be reduced.

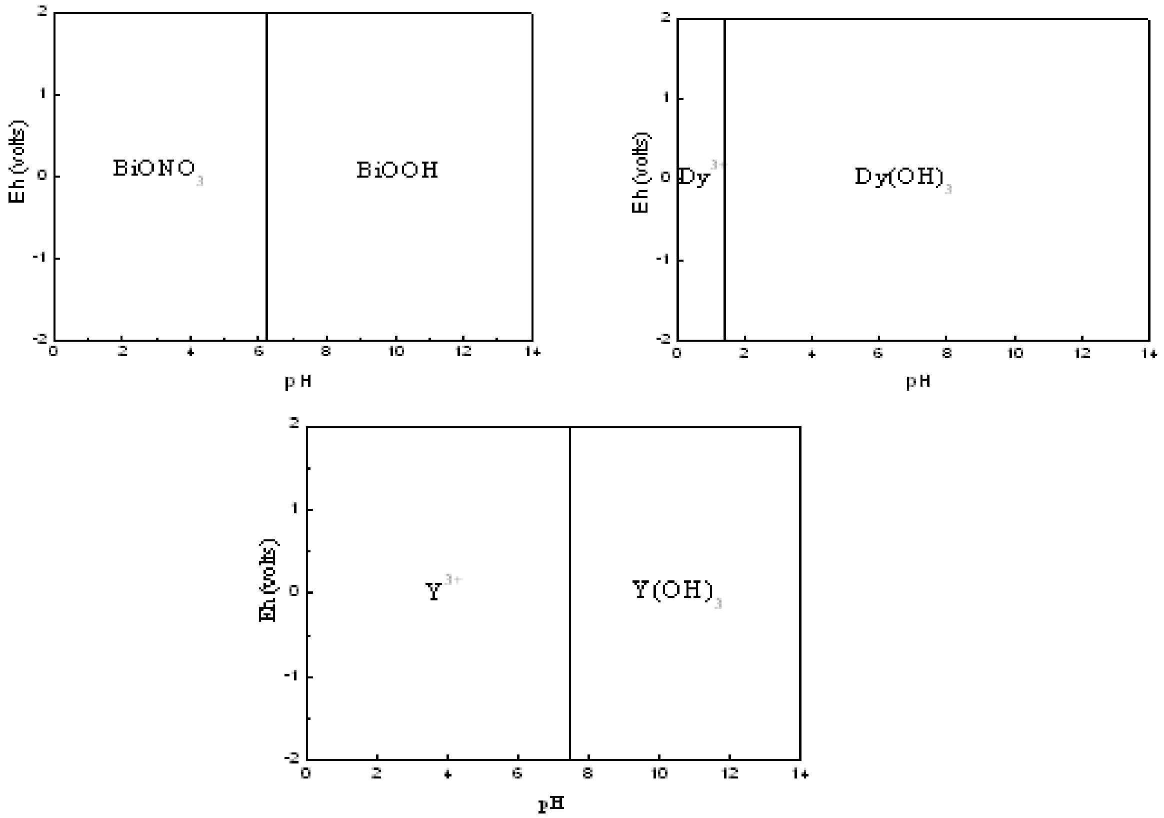

(a) At initial stage ($C_{Bi^{3+}} = 0.075 mol/L, C_{Dy^{3+}} = 0.025 mol/L, C_{Y^{3+}} = 0.025 mol/L,$)

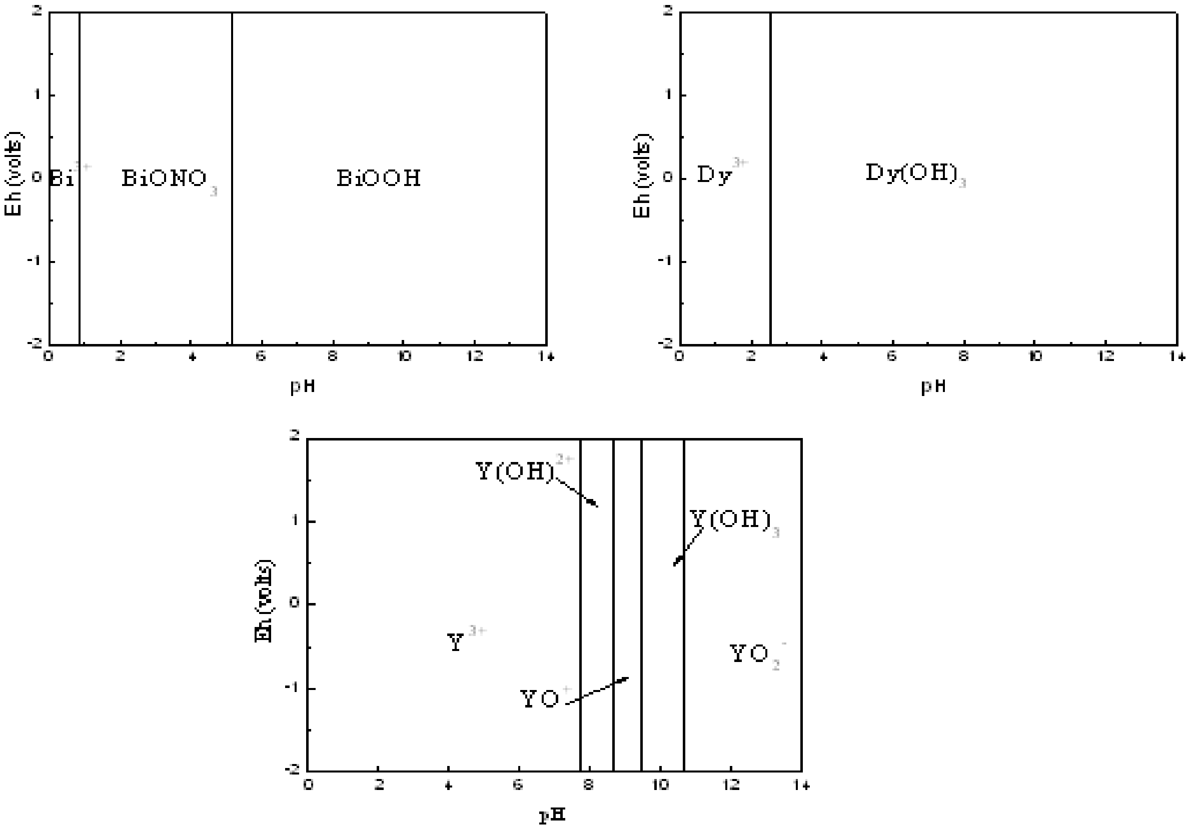

(b) At the end of the reaction
($C_{Bi^{3+}} = 10^{-5} mol/L, C_{Dy^{3+}} = 10^{-5} mol/L, C_{Y^{3+}} = 10^{-5} mol/L$)

Fig.2.2 Predominant species in the solution at 25°C and at 1atm.

Therefore, according to the calculation results and also taking into account Wang *et al.*[7] results, it was decided to fix the pH at 11.5 to avoid the formation of nitrate. And it is worth to note that the solubility of $Y(OH)_3$ is higher, but, at this pH, the concentration of $Y(OH)_3$ in solution should be lower than 10^{-4} mol/L, which should have little effect on the final composition. Then, the conditions of preparation for $(Bi_2O_3)_{0.75}(Dy_2O_3)_{0.25}$ were first optimized.

2.3 Experimental

2.3.1 Preparation of $(Bi_2O_3)_{0.75}(Dy_2O_3)_{0.25}$ nano-powder

$(Bi_2O_3)_{0.75}(Dy_2O_3)_{0.25}$ nano-powder samples were prepared by reverse titration of a solution of bismuth and dysprosium nitrate into an ammonia solution. Based on the thermodynamic equilibrium, the pH was maintained at 11.5 during the precipitation process by addition of ammonia. After thermal analysis, the precipitates were annealed at given temperatures to obtain the expected nano-powders.

Two methods were used:

(1) Analytical pure $Bi(NO_3)_3.5H_2O$and Dy_2O_3 were used as raw materials, the two reagents were dissolved in a nitric acid solution in molar ratio of 3:1 to obtain a total concentration of 0.1mol/L of [$Bi^{3+,}$ Dy^{3+}] metal ions. Aqueous ammonia (25%) was mixed with de-ionized water in 1:10 volume ratio (pH≅11.5) and 1 wt% PEG6000 (polyethylene glycol of average molecular weight equal to 6000) was added as a dispersant. A 50mL of the nitrate solution was then dropped into 550ml of the aqueous ammonia solution in a reaction vessel at room temperature. During the precipitation, the solution was continuously stirred using a magnetic needle. The precipitate was first washed 4 times by de-ionized water, then ethanol was added and the ethanol suspend solution was dried in a rotatory evaporator at 60^oC. The first $(Bi_2O_3)_{0.75}(Dy_2O_3)_{0.25}$ precursor was formed, it will be marked with a “E” in the following of the text, as well as the powder obtained afterwards.

(2) Bi_2O_3 and Dy_2O_3 were used as raw materials. Bi_2O_3 was annealed at 600^oC for one night prior to be used in order to remove the carbonates and the adsorbed water. Bi_2O_3 and Dy_2O_3 were first dissolved in nitric acid to prepare a 0.1mol/L solution of nitrate and the precipitation process was conducted using the same way as method (1), but at the end, the precipitate was washed 5 times with de-ionized water, it was then filtered and dried at 60^oC in an oven. To distinguish it from the first, the second precursor and the $(Bi_2O_3)_{0.75}(Dy_2O_3)_{0.25}$ powder obtained afterwards will be marked with the letter “F” (as filtered) in the following of the text.

2.3.2 Characterization

The precursors’ thermal behavior was investigated using a Setaram 92 TG-DTA combined with a Pfeifer Omnistar mass spectrometer in order to characterize the undergone decompositions. Experiments were carried out in air from room temperature to 900°C with a heating rate of 5°C/min.

A multi channel Raman spectrometer (DILOR XY 800) was used to record the room temperature spectra. The 647.1nm excitation line from a Spectra Physics Krypton ion laser was used. All samples were irradiated with a very low laser power

(3mW on the sample) to avoid any damage of the material, the beam was focused on the compound using the macroscopic configuration of the apparatus. Each spectral range of the spectrum was recorded using four accumulations of few seconds of integration time. An optical multi-channel charge coupled device, cooled with liquid nitrogen was used as detector. In the 15-1000 cm^{-1} frequency range, the spectral resolution was roughly 0.5 cm^{-1}. The LABSPEC software was used for collection and data processing.

High temperature X-ray diffraction was also performed on both precursor. Data were collected on a D8 Advance AXS Bruker diffractometer equipped with an Anton Paar HTK 1200N high temperature chamber and a Vantec1 detector (CuK_{α} radiation), from room temperature to 800°C, with a diagram collected every 20°C, in the $20^{o} \leq 2\theta \leq 80^{o}$ domain, with a 0.0148° step size and a counting time of 0.2 sec per step. A diagram was collected in 16′24″.

X-ray patterns of the powders were collected at room temperature, on a D8 Advance AXS Bruker diffractometer equipped with a Vantec1 detector ($\lambda_{CuK\alpha}$=1.5406Å). Data were collected in the $20^{o} \leq 2\theta \leq 80^{o}$ domain, with a 0.0148° step size and a counting time of 0.5 sec per step. A diagram was collected in 42′05″.

2.4 Results and analysis

2.4.1 Thermal behavior of the $(Bi_2O_3)_{0.75}(Dy_2O_3)_{0.25}$ precursors

2.4.1.1 Simultaneous TG-MS analysis of precipitates

Simultaneous thermogravimetric (TG)–mass spectra (MS) and thermo differential analysis (DTA) of both $(Bi_2O_3)_{0.75}(Dy_2O_3)_{0.25}$ precursors are shown in Fig.2.3.

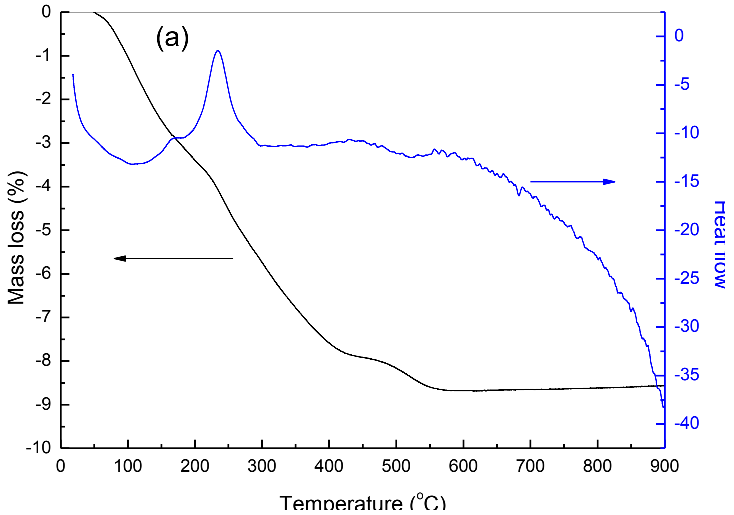
(a)
Mass loss (%)
0
-1
-2
-3
-4
-5
-6
-7
-8
-9
-10
Heat flow
0
-5
-10
-15
-20
-25
-30
-35
-40
0
100
200
300
400
500
600
700
800
900
Temperature (°C)

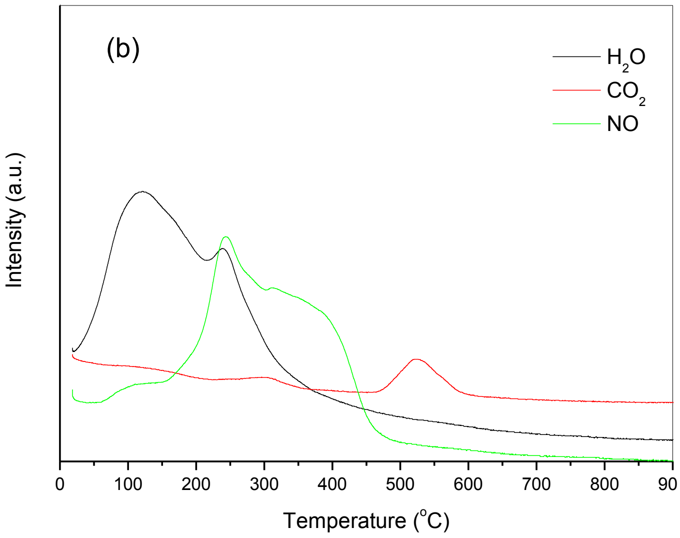
(b)
H₂O
CO₂
NO
Intensity (a.u.)
0
100
200
300
400
500
600
700
800
90
Temperature (°C)

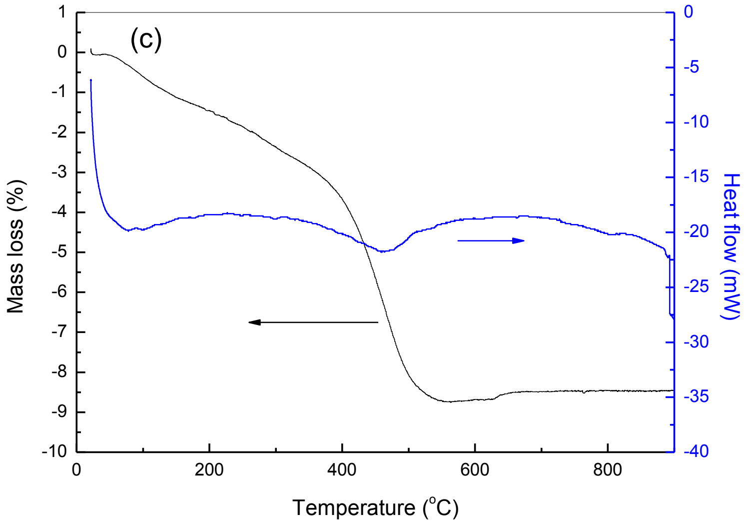
(c)
Mass loss (%)
1
0
-1
-2
-3
-4
-5
-6
-7
-8
-9
-10
Heat flow (mW)
0
-5
-10
-15
-20
-25
-30
-35
-40
0
200
400
600
800
Temperature (°C)

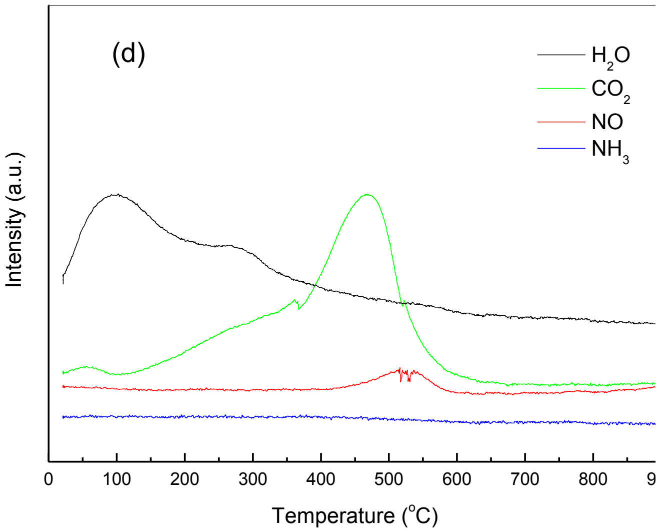

Fig.2.3 Thermal analysis (DTA-TG-MS) in air (5°C/min heating process) for $(Bi_2O_3)_{0.75}(Dy_2O_3)_{0.25}$ precursor E((a), (b))and precursor F((c), (d))

For precursor E (Fig.2.3a), the TG curve during the heating process can be divided into 3 steps with mass loss of 4%, 4% and 0.7%, respectively. From 20 to 200°C, the mass loss was due to the release of adsorbed water, which is characterized by a maximum of MS18 intensity nearby 120°C. In the range of 200-460°C, a small amount of water also released at the beginning of this step (peak MS18 at 235°C), it could be attributed to the decomposition of the hydroxide. CO_2, characterized by MS44, is identified weakly during the first mass change, but the signal became stronger during the second weight variation and reached to maximum at 255°C. It results from the decomposition of carbonate.

Between 460 and 600°C (max. at 535°C), a peak of MS30, which characterizes NO entity, indicated that the third step of mass loss corresponded to the decomposition of nitrate compounds. It is worth noting that the temperature of this decomposition is in good agreement with the TG curve reported by Kodama[11] for thermal decomposition of $Bi_5O_7NO_3$. This confirms the presence of nitrates in the sample, despite the precautions taken during the precipitation.

TG curve (Fig.2.3b) of the precursor F is somewhat different from that of precursor E (Fig.2.3a), although the final mass change is closely similar (≅8.7%). The mass change corresponding to water release until 300°C is slightly less intense (≅2.6%) than for precursor E. In contrast to precursor E, the release of CO_2 is smooth at the beginning and gives a main peak in the 370-550°C range (maximum at almost

470°C). The intermediate stage, which was identified in the temperature range 400-460°C for E, has disappeared for F. However, the MS signal 30 (mass of NO), corresponding to nitrate(s) decomposition, is still observed in the temperature range 400-580°C, its intensity is slightly lower than for precursor E. So the de-carbonation and the decomposition of nitrate species occur almost simultaneously and lead to a single weight loss in the range 370-580°C, characterized by a wide endothermal effect centered at 450°C.

MS15 signal, which could characterize NH_3 ionization, was also examined, but no clear modification was observed.

From these results, one can conclude that the precursors contain a mixture of hydroxide, carbonate with a small amount of nitrates, which start to decompose at 450°C.

2.4.1.2 Raman spectroscopy on precursors

The presence of nitrate was confirmed by Raman spectroscopy for the two precursors. The spectra are given in Fig.2.4. The presentation of the results is firstly limited to the 900-1200cm^{-1} spectral domain, where the most intense bands of nitrate species are usually observed. Raman spectra of NH_4NO_3, $Bi(NO_3)_3.5H_2O$, $Bi_5O_7NO_3$ are also presented as reference compounds.

Both precursors exhibit two main bands at 1044 and 1070 cm^{-1}. The observation of several lines for a symmetrical stretching motion of the N-O bond associated to the evolution of their intensity ratio indicate the presence of two nitrate species, with a specific ratio for each sample. The low wave-number band (1044cm^{-1}) is likely the fingerprint of $Bi_5O_7NO_3$ which exhibits a band at the same frequency. For the second band, none of the references we used matched. It is worth noting that the intensity of these two bands is not the same in both precipitates. Precursor F would contain more $Bi_5O_7NO_3$ than other unknown nitrate in contrast to precursor E.

The occurrence of ammonium ion could not be examined, since the bands of NH_4^+ (3040 and 3145 cm^{-1} for the symmetrical and anti-symmetrical stretching motions and 1680 and 1400 cm^{-1} for the deformations of the free cation) are very weak due to a too low cross section of the ammonium ion.

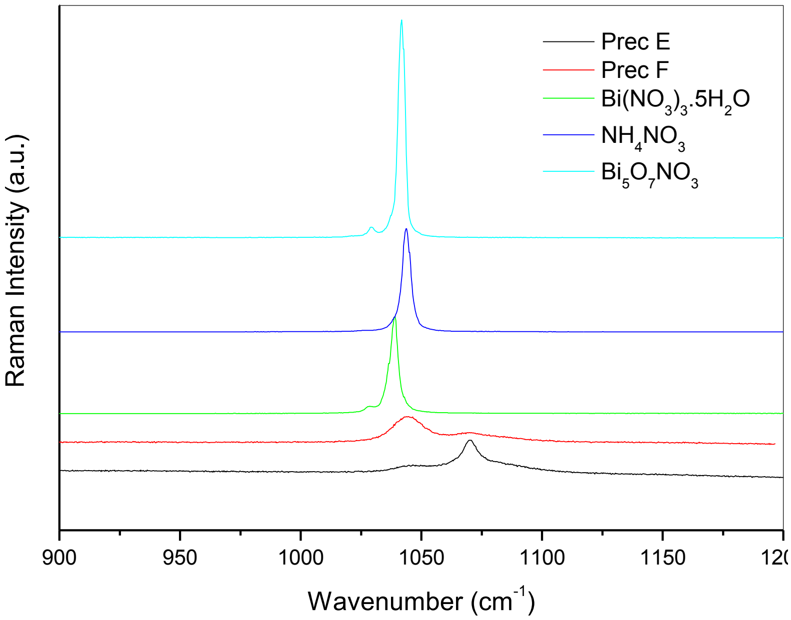

Fig.2.4 Raman spectra in the 900-1200 cm^{-1} wavenumber range of NH_4NO_3, $Bi(NO_3)_3.5H_2O$, $(Bi_2O_3)_{0.75}(Dy_2O_3)_{0.25}$ precursor E and precursor F

The presence of nitrate seems to contradict the thermodynamic calculations. One reason is the uncompleted calculation because of the shortage of data. Another reason was the pH gradient in the drop. Indeed, when a drop fells into the ammonia solution, the pH value at the interface reached to 11.5 immediately; but the pH value in the interior of the drop increased gradually. In this process, for example $BiONO_3$ could form, as well as $Bi_5O_7NO_3$. According to the thermodynamic data, $BiONO_3$ would transform to BiOOH if the solution reached to the equilibrium, as well as $Bi_5O_7NO_3$. But from the kinetic point of view, these transformations may be not complete during the prepcipitation process. This would explain the presence of nitrate in the precipitate obtained by reversing-titration method.

2.4.1.3 High temperature X-ray diffraction

The same precursors were then studied by high temperature X-ray diffraction. The corresponding thermodiffractograms are given in Fig.2.5.

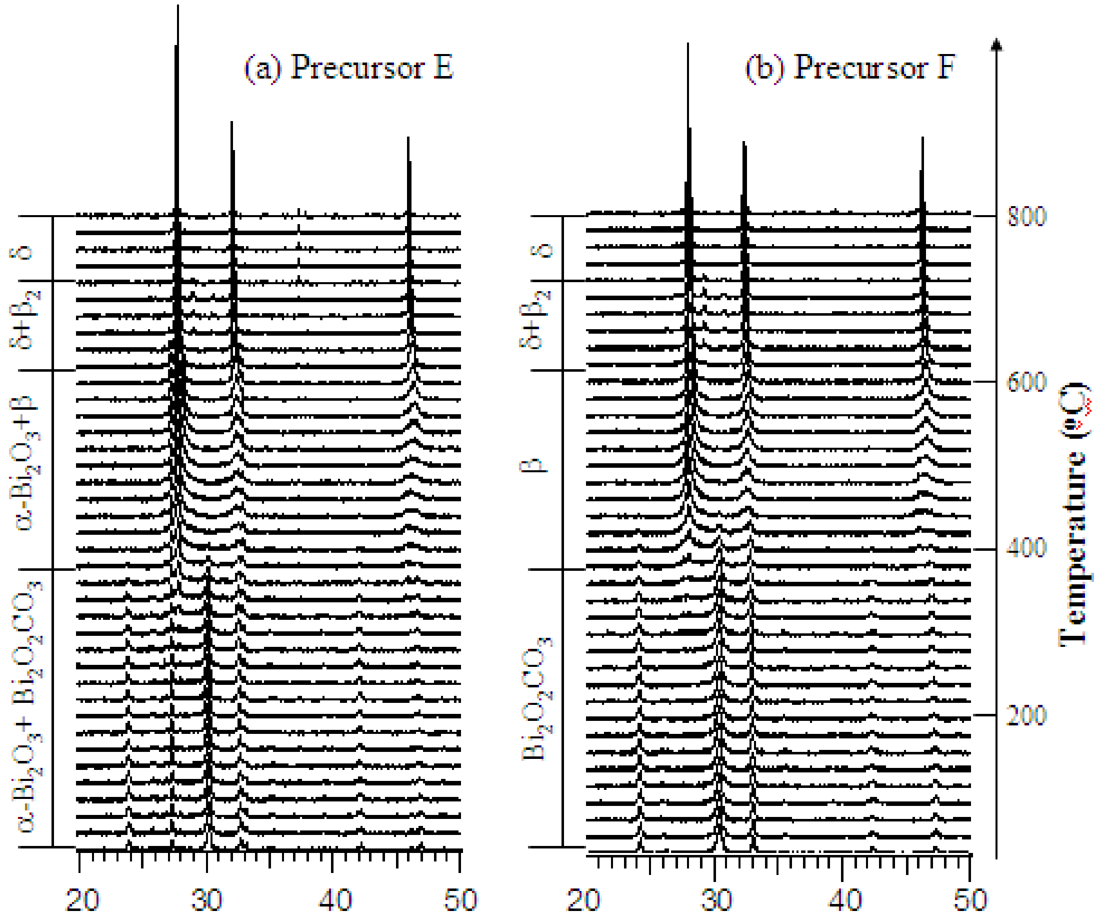

Fig.2.5 X-ray diffraction at variable temperatures
for $(Bi_2O_3)_{0.75}(Dy_2O_3)_{0.25}$ precursor E (a) and precursor F (b)

In Fig.2.5(a), for precursor E, $Bi_2O_2CO_3$ and α-Bi_2O_3 are obviously identified from room temperature to 380°C. $Bi_2O_2CO_3$ disappears between 380°C to 400°C, it is replaced by a tetragonal β-Bi_2O_3 type phase, including probably dysprosium, which coexists with α-Bi_2O_3 until 640°C. These phases, thus transform into a mixture of face centered cubic (fcc) fluorite type phase (δ-type) and rhombohedral β_2-type phase which are likely bismuth-dysprosium mixed oxides. These two latter forms merge into a single δ-bismuth-dysprosium oxide phase nearby 720°C and the characteristic pattern of fcc symmetry is maintained up to 800°C. The XRD evolution of precursor F is quite similar to that of precursor E. However α-Bi_2O_3 is not observed. Only carbonate is identified at room temperature up to 400°C. The peaks observed at angles ≅39.0-39.5° and ≅45.5-46.0° in 2θ correspond to the platinum sheet which was used as sample holder.

Above 600°C, a large decrease of the width at half maximum of peaks is clearly observed, indicating an increase of the powder grain size.

2.4.2 Characterization of the $(Bi_2O_3)_{0.75}(Dy_2O_3)_{0.25}$ nano-powders

To obtain $(Bi_2O_3)_{0.75}(Dy_2O_3)_{0.25}$ powders with grains at nano scale, the temperature must be as low as possible to avoid grain growth, but it must be high enough to allow the complete decomposition of the precursor. From the previous thermal behavior investigations, the last mass loss due to the decomposition of nitrate occurred around 500^{o}C. The precursors were therefore annealed at 450, 500 and 600°C for 3 hours, although, at these temperatures, β-forms may be stabilized instead of δ-forms. In order to confirm the decomposition of nitrates, the obtained powders were characterized analytically by Raman spectroscopy and X-ray diffraction techniques.

2.4.2.1 Raman spectra of powders annealed at different temperatures

Raman spectra of powders annealed at different temperatures for 3h, are shown in Fig.2.6. In contrast to the spectra collected on precursors, the Raman spectra of powders exhibit a decrease of the signal/noise ratio, which is in good agreement with a decrease of the nitrates amount after annealing. The signal/noise ratio for F samples are weaker than for E samples which indicates a lower amount of nitrates for this powder, in agreement with the TG-MS analyses which showed a lower signal for NO. For precursor E, even after annealing at 600^{o}C the principal lines characteristic of NO_3^- species are still observed, which is not the case for powder F annealed at 600^{o}C. However, a shift toward lower frequency 1023 and 1052 cm^{-1} is to be noticed for E-600, it could be due to a lengthening of the N-O bonds, due to the formation of intermediate nitrate(s).

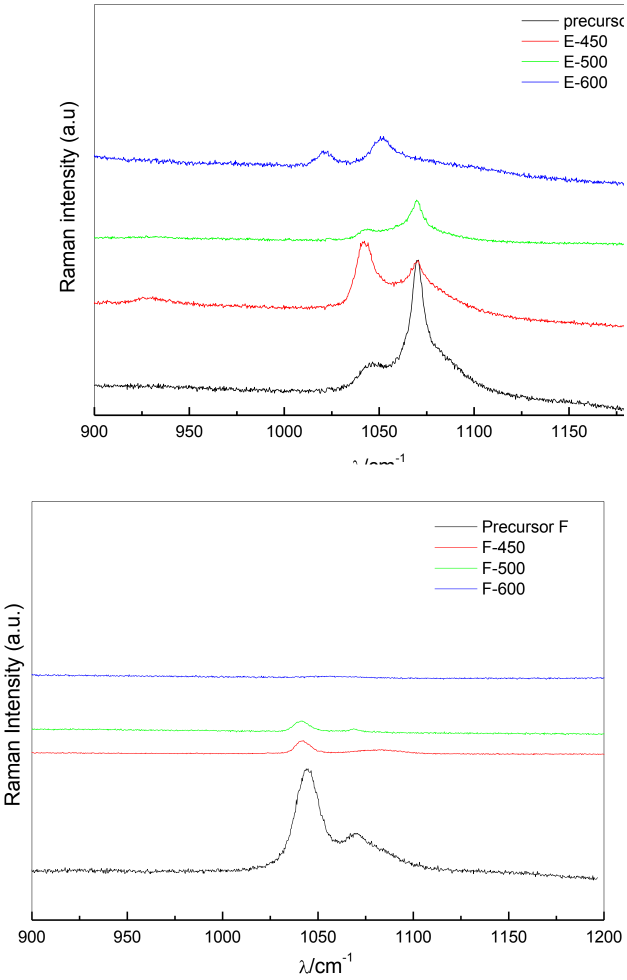

Fig.2.6 Raman spectra in the 900-1200 cm^{-1} wavenumber range of $(Bi_2O_3)_{0.75}(Dy_2O_3)_{0.25}$ precursor E, F; annealed at 450°C (E, F-450), annealed at 500°C (E, F-500) and annealed at 600°C (E, F-600)

Fig.2.7 gives the TG curve of the powder E annealed at 450^{o}C for 1h. This temperature is lower than the decomposition temperature of nitrates in the precursor (according to Fig.2.3), however the carbonate may be only partly decomposed. The weight loss observed between the room temperature and 450°C is to be attributed to the release of water and carbon dioxide, adsorbed by the powder before the TG analysis, and to the remaining traces of $Bi_2O_2CO_3$ which wouldn't decompose completely during the annealing process. The temperature range of the following weight loss (450-600°C) has to be attributed to the nitrates decomposition. It is only 0.9%. Therefore, the amount of nitrates in powders annealed at higher temperature should be lower than 4.8%.

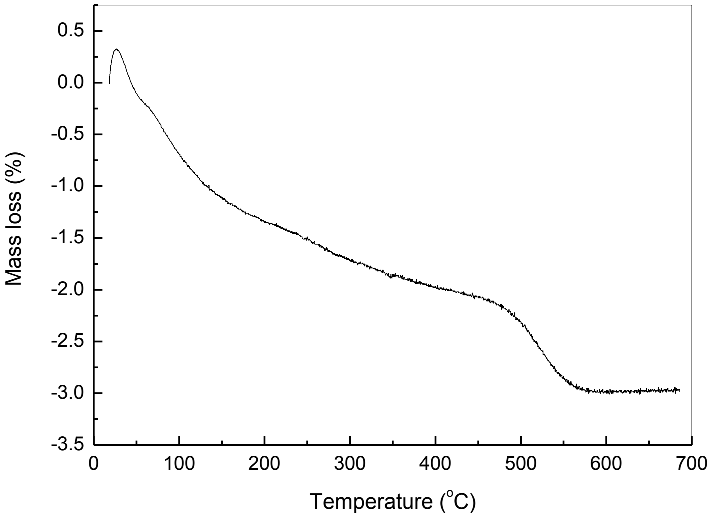

Fig.2.7 TG curve of powder E annealing at 450°C

Although the risk of a small amount of nitrates and the fact a β-phase would be stabilized, according to the results above, both precipitates were annealed at 500°C for 3h to avoid grain growth. The powders will be labeled E and F, respectively.

2.4.2.2 X-ray fluorescence

In order to determine the precise composition of the powders, X-ray fluorescence analysis was performed on both powders annealed at 500°C for 3h. Five standard samples, which were prepared by mixing Bi_2O_3 and Dy_2O_3 in mol ratio of 9:1, 7:1, 3:1, 5:3 and 1:1, and annealed at 800°C for 8h for several times, were also studied as references for quantitative analysis.

For this study, a Shimadzu XRF-1800 apparatus was used. Both powders were pressed into disks of 1 cm in diameter.

Results from quantitative analysis are given in Table 2.2. Within the experimental error, the compositions are in very good agreement with the expected one.

Table 2.2 The weight percentage of Bi_2O_3 and Dy_2O_3 in E and F powders annealed at 500°C for 3 hours

	Theoretical value	**Powder E**	**Powder F**
Bi_2O_3	78.94%	78.83 ± 0.31%	79.35±0.33%
Dy_2O_3	21.06%	21.17 ± 0.04%	20.65 ± 0.01%

2.4.2.3 X-ray diffraction and Raman scattering combined investigations

Then, to verify the structure of the phases obtained after annealing, X-ray diffraction was performed. Fig.2.8 showed the XRD patterns of both $(Bi_2O_3)_{0.75}(Dy_2O_3)_{0.25}$ powders.

As expected from high temperature X-ray diffraction, mainly β forms were evidenced in both cases. However, as in precursor E, α-Bi_2O_3 was observed in powder E.

However, using only XRD, with so wide peaks, it was difficult to confirm if the phase was a β or a δ form. In this aspect, Raman spectroscopy is more sensitive.

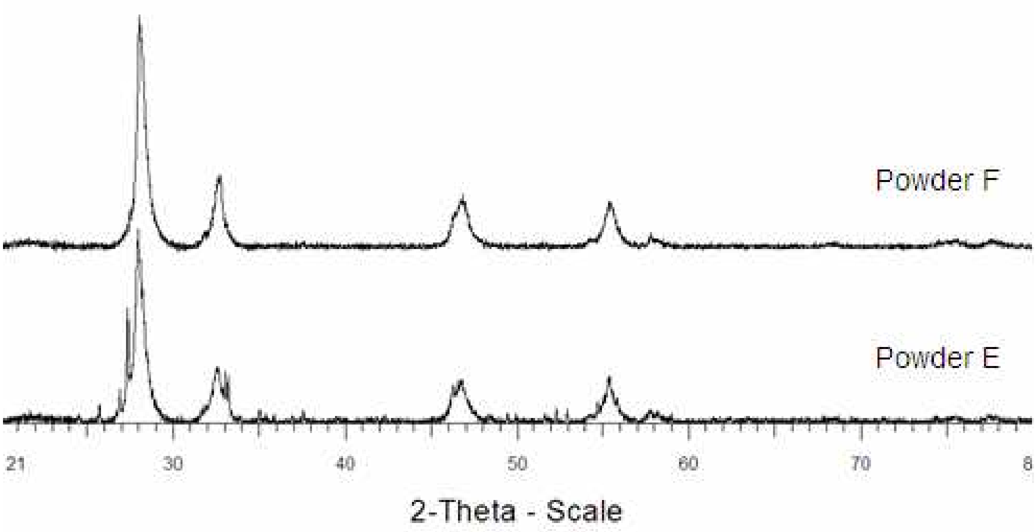

Fig.2.8 XRD patterns of $(Bi_2O_3)_{0.75}(Dy_2O_3)_{0.25}$ powders (E, F)

Fig.2.9 displays the extended Raman spectra (wave-number range: 25–1300 cm^{-1}) of both precursors and powders annealed at 500°C, they are compared to powders annealed at 750°C, temperature at which a δ form is expected. For comparison, the spectra of β-$Bi_{0.925}Dy_{0.075}O_{1.5}$, δ-$Bi_{0.7}Dy_{0.3}O_{1.5}$, prepared by solid state reaction, and that of α-Bi_2O_3 are also given. The typical bands of 3 phases are shown in Table 2.3.

Table 2.3 The typical bands of α, β and δ phases

Phase	Typical bands (cm^{-1})
α-Bi_2O_3	54, 61 ,68, 85, 95, 104, 120, 140, 153, 185, 212, 280, 314,412 and 449
β-$Bi_{0.925}Dy_{0.075}O_{1.5}$	52, 101, 121, 251, 313, 490 and 635
δ-$Bi_{0.7}Dy_{0.3}O_{1.5}$	51, 106, 233 and 636

Both precursors were in amorphous state. They display very different bands when compared with the other spectra. However, the presence of α phase in precursor E is clearly confirmed with bands at 210, 280, 315, 410 and 449 cm^{-1}. These bands remain in the powder E annealed at 500°C, as expected from the high temperature XRD, they disappear in the powder annealed at 750°C. The spectra of powders annealed at 750°C are very close to the spectrum of δ-$Bi_{0.7}Dy_{0.3}O_{1.5}$ which confirms the stabilization of δ-form at this temperature. In contrast, powder F annealed at 500°C exhibits the same typical bands as β-$Bi_{0.925}Dy_{0.075}O_{1.5}$, while in powder E, besides the bands of β, the bands of α- Bi_2O_3 are clearly visible. The bands observed around 1044 and 1070 cm^{-1} correspond to remaining NO_3^-, they disappear in the powder E and F annealed at 750°C. Therefore, as expected from high temperature X-ray diffraction, β-phase are mainly obtained after annealing at 500°C, although traces of δ could not be excluded since δ characteristic bands are very close to the main bands of β.

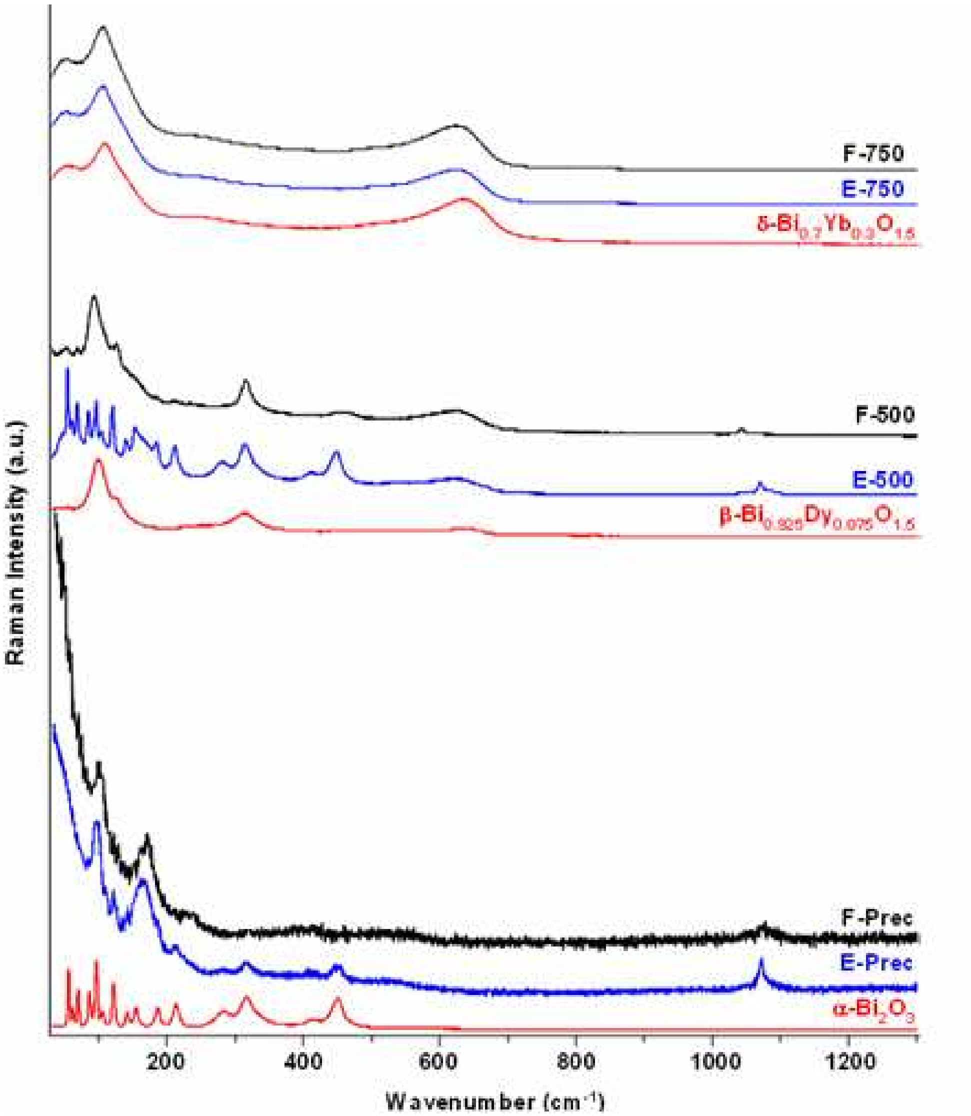

Fig.2.9 Raman spectra in the wave-number range of 25–1300 cm^{-1} for $Bi_{0.75}Dy_{0.25}O_{1.5}$ precursors (E-prec and F-prec), precursors annealed at 500°C (E-500 and F-500) and 750°C (E-750 and F-750), α-Bi_2O_3, β-$Bi_{0.925}Dy_{0.075}O_{1.5}$ and δ-$Bi_{0.7}Yb_{0.3}O_{1.5}$

The X-ray diffraction patterns of powder E and F annealed at 500°C was fitted using the Rietveld method with Fullprof program[12]. The Thompson-Cox-Hasting pseudo-voigt function was used to model the profile. The instrument resolution was deduced from a LaB_6 standard collected in the same conditions. Lorentzian isotropic strain parameters (X), Lorentzian isotropic size parameter (Y), and the isotropic size parameter of Gaussian character (IG) were refined to extract information on the crystallite size and the possibility of micro-strains in the sample. The structural model proposed by Blower[13] (cf annex 1) was used for the β-phase, 25% of Dy were introduced in the bismuth site. For the α-phase, the structural model proposed by Harwig [14] (also given in annex 1) was introduced. Because of the lack of data, only an overall thermal parameter was refined in the structural models.

For powder E, a good fit was obtained when a mixture of α and β-phase was introduced in the refinement. The calculated pattern is compared to experimental data in Fig.2.8. A good agreement between the calculated and experimental data was observed with reliability factors of Rp=4.03%, Rwp=5.02%, Rexp=3.30% for the profile, R_B=2.16% and R_F=2.49% for the β-form and R_B=8.65% and R_F=5.51% (expression of reliability factors is given in annex 2). From this refinement, the relative amount of each phase was deduced; it led to 88% of β-phase, against 12% of α-phase.

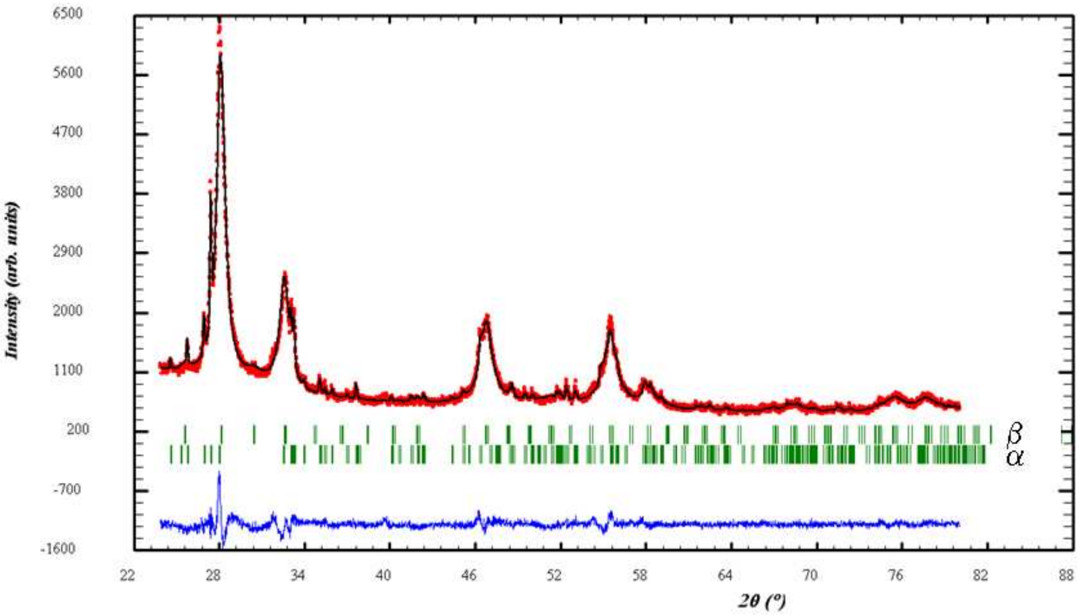

Fig.2.10 XRD calculated data compared to experimental data for $(Bi_2O_3)_{0.75}(Dy_2O_3)_{0.25}$ powder E. The refinement led to a mixture of 88% of β-phase against 12% of α-phase. Experimental points are in red, the calculated profile is black, the good agreement between the calculated and experimental data is given by the difference in blue. Sticks in green, indicate the position of Bragg peaks for β and α, respectively.

From these data, the integral widths of Bragg peaks (β) were deduced. According to Williamson et Hall[15], it should verify the following relationship:

$$\frac{\beta\cos\theta}{\lambda}=\frac{1}{D}+\frac{4\varepsilon}{\lambda}\sin\theta \qquad (2.10)$$

where D is the size of isotropic crystallites and ε is the microstrain.

When using reciprocal parameters, this relationship can be written as follows:

$$\beta^* = \frac{1}{D} + 2\varepsilon d^* \tag{2.11}$$

From the refinement, the evolution of the reciprocal width (β*) was plotted in function of the reciprocal distance (d*) for both phases (Fig.2.9).

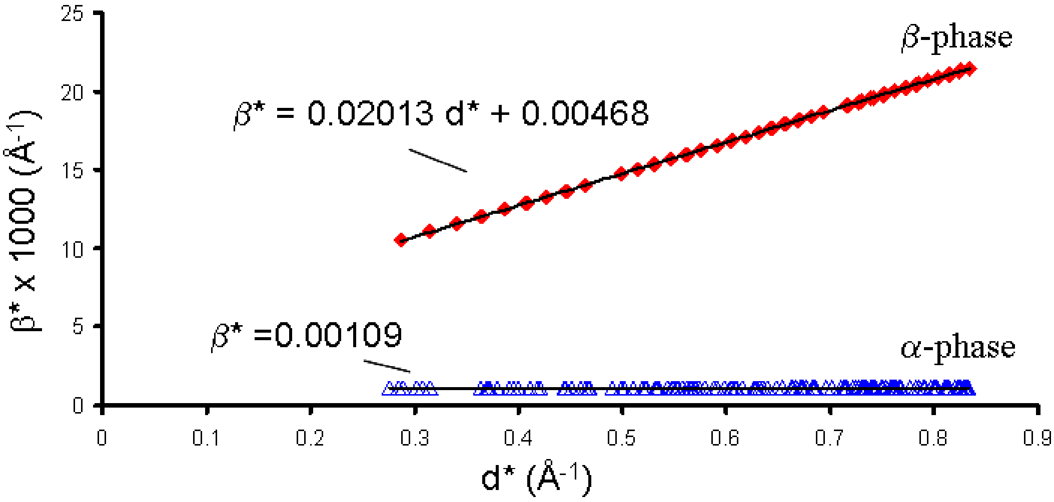

Fig.2.11 Williamson-Hall plot corresponding to the α-phase and β-phase contained in $(Bi_2O_3)_{0.75}(Dy_2O_3)_{0.25}$ powder E.

From these data, a crystallite size of 21nm was deduced for the β-phase and of 92nm for the α-phase. Whereas no strain was observed for the α-phase (slope equal to zero), the calculation led to a strain of 1% for the β-phase. This strain is likely due to the presence of the α-phase in the mixture.

No α-phase was evidenced in the powder F but the fit was not good taking into account only the β-phase (Fig.2.12) (Rp=6.28%, Rwp=3.36%, Rexp=5.00% for the profile, R_B=5.57% and R_F=11.3% for the structure). The powder is likely a mixture of β-phase and δ-phase. However, the unit-cell parameters of the two phases being to close, it was not possible to refine the data with such a mixture. Although the micro-structural parameters may be erroneous in this case, the Williamson-Hall plot was also studied and led to a mean crystallite size of 17nm with strain of 0.6%.

It is worth noting that both refinement led to very close unit-cell parameters for the β-phase: a=7.775(5)Å, b=5.480(6) Å and a=7.779(5)Å, b=5.482(7) Å for the E and F powders, respectively.

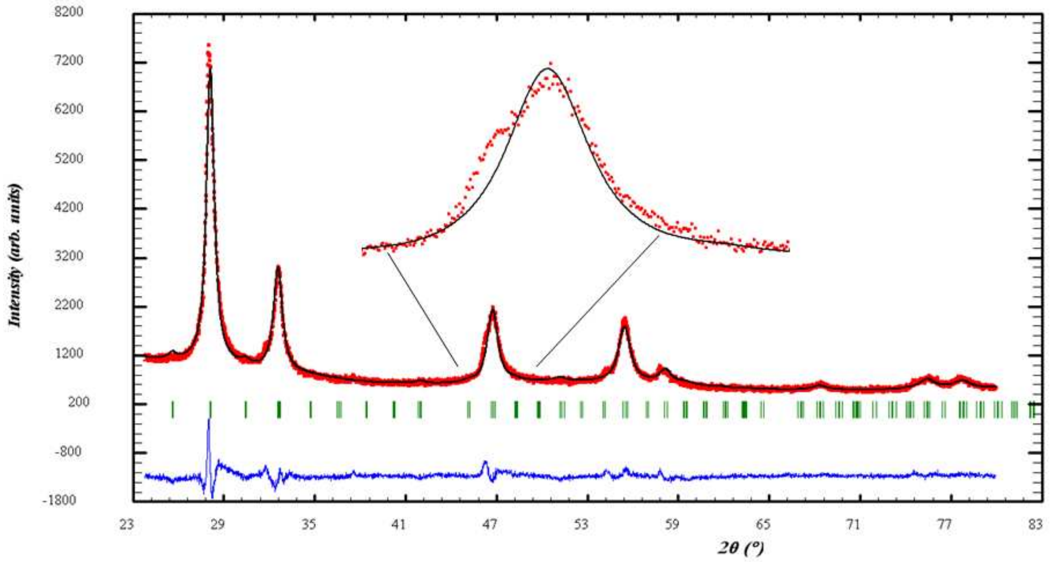

Fig.2.12 XRD calculated data compared to experimental data for $(Bi_2O_3)_{0.75}(Dy_2O_3)_{0.25}$ powder F. Experimental points are in red, the calculated profile is black, the agreement between the calculated and experimental data is given by the difference in blue. Sticks in green, indicate the position of Bragg peaks.

2.4.2.4 Micrograph of $(Bi_2O_3)_{0.75}(Dy_2O_3)_{0.25}$ powders

The nano-scale size of powder F annealed at 500°C for 3h was confirmed by TEM. The analyses were performed on a HITACHI H-800 Transmission Electron Microscope. Micrographs are given in Fig.2.13. It shows particles with nearly spherical shape of about 20nm in diameter. This value is in good agreement with the XRD result (although the attached error in the calculation, the value deduced by XRD was under-estimated due to the possibility of thinner Bragg peaks in presence of a second polymorph), and one can therefore conclude that the particles are single crystallite with a size of about 20nm.

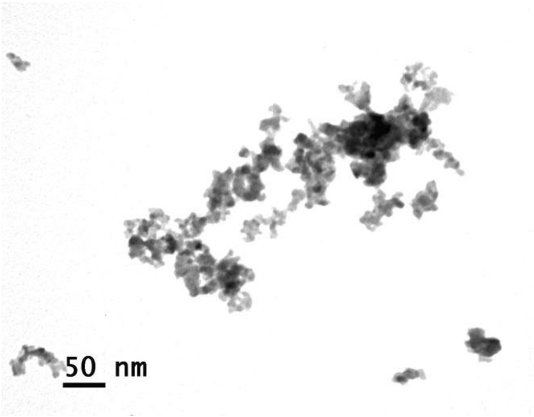

Fig.2.13 Micrography of $(Bi_2O_3)_{0.75}(Dy_2O_3)_{0.25}$ powders

Since, the occurrence of α phase in powder E may affect the sintering process, the method 2 leading to F powder, was kept for the preparation of other compositions.

2.5 Preparation and characterization of $(Bi_2O_3)_{0.75}(Y_2O_3)_{0.25}$, $(Bi_2O_3)_{0.75}(Er_2O_3)_{0.25}$ and $(Bi_2O_3)_{0.75}(Er_2O_3)_{0.125}(Y_2O_3)_{0.125}$ powders

Bi_2O_3, Er_2O_3 and Y_2O_3 were used as raw materials for the preparation of $(Bi_2O_3)_{0.75}(Y_2O_3)_{0.25}$, $(Bi_2O_3)_{0.75}(Er_2O_3)_{0.25}$ and $(Bi_2O_3)_{0.75}(Er_2O_3)_{0.125}(Y_2O_3)_{0.125}$ nano-powders. Bi_2O_3 was annealed at 600^{o}C for one night before use in order to remove adsorbed water and carbonate. Then, method 2 was used to obtain the precipitates, and the precursors were also annealed at 500^{o}C for 3h to obtain the nano-powders.

Fig.2.14 shows the XRD patterns of each powder. They are similar to $(Bi_2O_3)_{0.75}(Dy_2O_3)_{0.25}$ powder F.

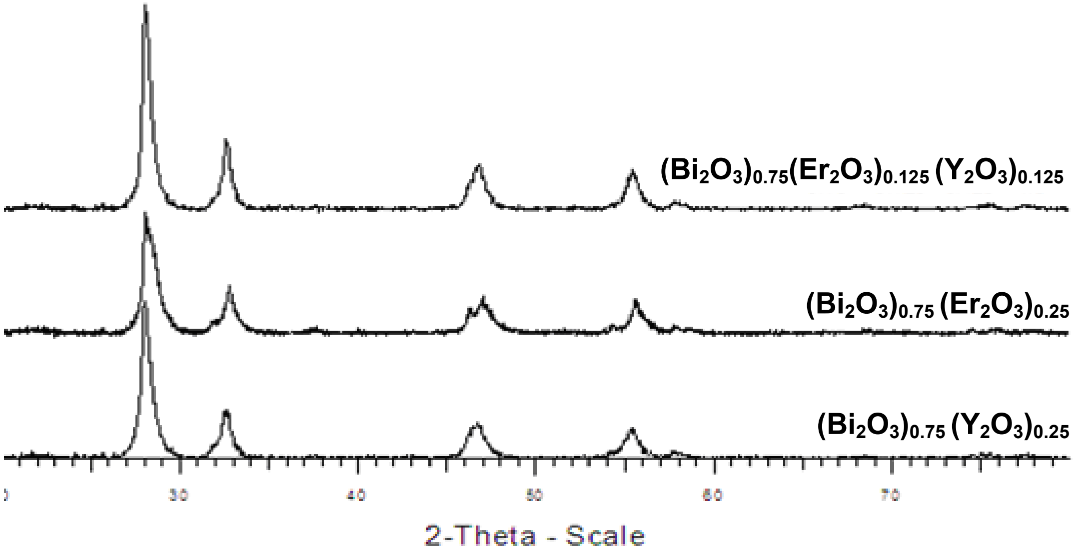

Fig.2.14 XRD patterns of $(Bi_2O_3)_{0.75}(Y_2O_3)_{0.25}$, $(Bi_2O_3)_{0.75}(Er_2O_3)_{0.25}$ and $(Bi_2O_3)_{0.75}(Er_2O_3)_{0.125}(Y_2O_3)_{0.125}$ nanopowders

However, as for powder F, refinement led to rather poor fits taking into account only the β-phase (Fig.2.15), even no α phase was evidenced in the powders. ($(Bi_2O_3)_{0.75}(Y_2O_3)_{0.25}$: Rp=7.47%, Rwp=9.24%, Rexp=3.96% for the profile, R_B=11% and R_F=24% for the structure; $(Bi_2O_3)_{0.75}(Er_2O_3)_{0.25}$: Rp=5.43%, Rwp=6.77%, Rexp=3.79% for the profile, R_B=9.22% and R_F=9.43% for the structure; $(Bi_2O_3)_{0.75}(Er_2O_3)_{0.125}(Y_2O_3)_{0.125}$: Rp=7.70%, Rwp=9.49%, Rexp=3.68% for the profile, R_B=14.2% and R_F=30.2% for the structure.)

As $(Bi_2O_3)_{0.75}(Dy_2O_3)_{0.25}$ powder, these powders were also likely a mixture of β-phase and δ-phase. Although the micro-structural parameters may be erroneous in this case, the Williamson-Hall plot was also studied and led to a mean crystallite size of 12, 10 and 11 nm for $(Bi_2O_3)_{0.75}(Y_2O_3)_{0.25}$, $(Bi_2O_3)_{0.75}(Er_2O_3)_{0.25}$ and $(Bi_2O_3)_{0.75}(Er_2O_3)_{0.125}(Y_2O_3)_{0.125}$, respectively.

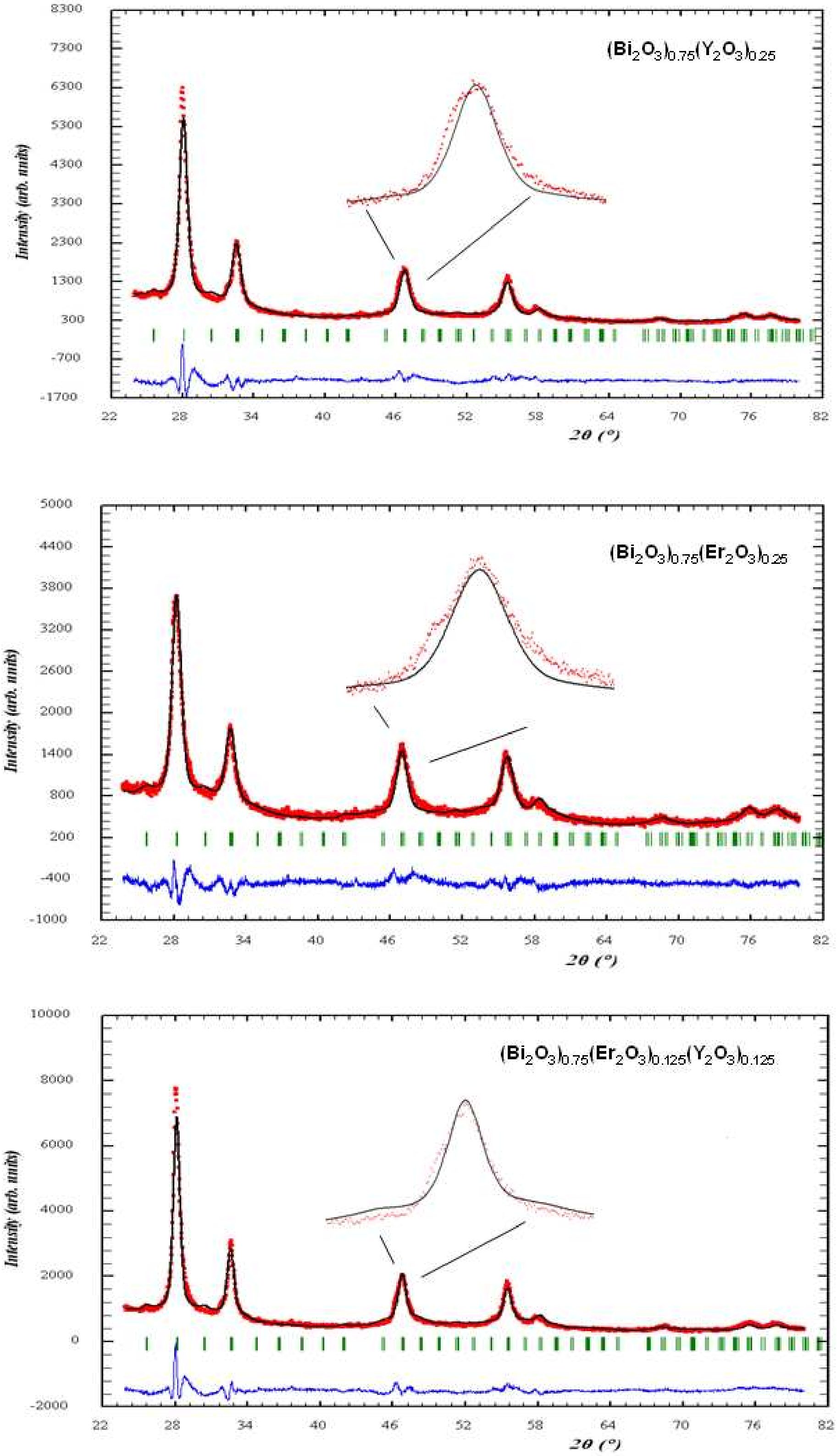

Fig.2.15 XRD calculated data compared to experimental data for $(Bi_2O_3)_{0.75}(Y_2O_3)_{0.25}$, $(Bi_2O_3)_{0.75}(Er_2O_3)_{0.25}$ and $(Bi_2O_3)_{0.75}(Er_2O_3)_{0.125}(Y_2O_3)_{0.125}$ powders with the structure of the β-phase. Experimental points are in red, the calculated profile is black, the agreement between the calculated and experimental data is given by the difference in blue. Sticks in green, indicate the position of Bragg peaks.

The corresponding unit-cell parameters of the β-phase in each composition are given in Table 2.4. $a/\sqrt{2}$ is also reported to evidence how close to cubic (fcc cell), the symmetry is. Very close unit cell parameters (when described in the fcc cell) are observed which confirm the β-form is very close to the δ-form.

Close unit cell parameters were obtained for all compositions, in close agreement with Dy^{3+} (1.027Å), Y^{3+} (1.019Å) and Er^{3+} (1.004Å) radius with a slightly lower value for Er^{3+}.

Table 2.4 Unit cell parameters of the β-phase in powders after sintering at 500°C for 3h deduced from Rietveld refinement of XRD data

Composition	a (Å)	$a/\sqrt{2}$ (Å)	c (Å)
$(Bi_2O_3)_{0.75}(Dy_2O_3)_{0.25}$	7.779(5)	5.500(4)	5.482(7)
$(Bi_2O_3)_{0.75}(Y_2O_3)_{0.25}$	7.79(1)	5.51(1)	5.48(2)
$(Bi_2O_3)_{0.75}(Er_2O_3)_{0.25}$	7.761(3)	5.487(2)	5.433(4)
$(Bi_2O_3)_{0.75}(Er_2O_3)_{0.125}(Y_2O_3)_{0.125}$	7.777(9)	5.499(7)	5.48(1)

To determine the precise composition, X-ray fluorescence analysis was also performed on $(Bi_2O_3)_{0.75}(Y_2O_3)_{0.25}$, $(Bi_2O_3)_{0.75}(Er_2O_3)_{0.25}$ and $(Bi_2O_3)_{0.75}(Er_2O_3)_{0.125}(Y_2O_3)_{0.125}$ powders annealed at 500°C for 3h. Results from semi-quantitative analysis, using external standards, are given in Table 2.5. Within the experimental error, the compositions are in very good agreement with the expected one.

Table 2.5 Weight percentage of metal oxide in $(Bi_2O_3)_{0.75}(Y_2O_3)_{0.25}$, $(Bi_2O_3)_{0.75}(Er_2O_3)_{0.25}$ and $(Bi_2O_3)_{0.75}(Er_2O_3)_{0.125}(Y_2O_3)_{0.125}$ powders annealed at 500°C for 3 hours, compared to theoretical values deduced by X-ray fluorescence.

	$(Bi_2O_3)_{0.75}(Y_2O_3)_{0.25}$		$(Bi_2O_3)_{0.75}(Er_2O_3)_{0.25}$		$(Bi_2O_3)_{0.75}(Er_2O_3)_{0.125}(Y_2O_3)_{0.125}$		
	Bi_2O_3	Y_2O_3	Bi_2O_3	Er_2O_3	Bi_2O_3	Er_2O_3	Y_2O_3
Theoretical value	86.09%	13.91%	78.50%	21.50%	82.14%	11.22%	6.64%
Experiment value	86.23 ±0.08%	13.77 ±0.02%	78.75 ±0.12%	21.25 ±0.02%	82.31% ±0.09%	11.13% ±0.02%	6.56% ±0.03%

The TEM micrographs of these powders are shown in Fig.2.16. Despite the agglomeration, particles with size smaller than 20nm are observed for each sample. This size is very close to the crystallite size deduced from XRD data again, which value were under-estimated, since only one phase was taken into account in the refinement. Once again, one can conclude that using this method of preparation, single crystalline powders are obtained.

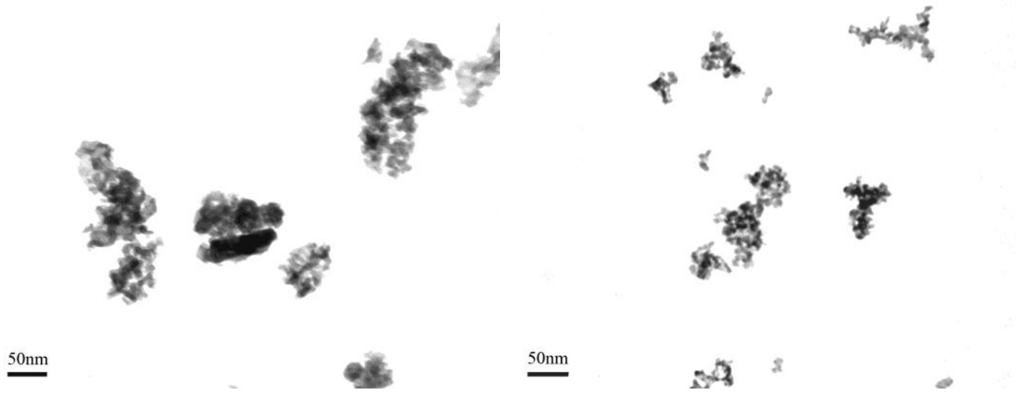

$(Bi_2O_3)_{0.75}(Er_2O_3)_{0.25}$ $(Bi_2O_3)_{0.75}(Y_2O_3)_{0.25}$

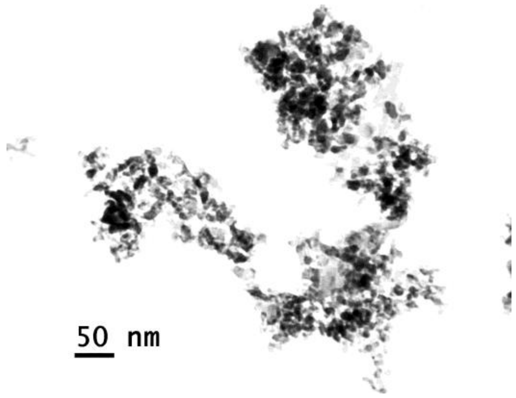

$(Bi_2O_3)_{0.75}(Er_2O_3)_{0.125}(Y_2O_3)_{0.125}$

Fig.2.16 TEM micrographs of $(Bi_2O_3)_{0.75}(Er_2O_3)_{0.25}$, $(Bi_2O_3)_{0.75}(Y_2O_3)_{0.25}$ and $(Bi_2O_3)_{0.75}(Er_2O_3)_{0.125}(Y_2O_3)_{0.125}$ powders annealed at 500°C for 3h.

2.6 Conclusions

Powders of bismuth-based materials with grain size at the nano-scale were successfully prepared by reverse tritration co-precipitation method. The preparation was first optimized for composition $(Bi_2O_3)_{0.75}(Dy_2O_3)_{0.25}$ and then applied to other compositions $(Bi_2O_3)_{0.75}(Er_2O_3)_{0.25}$, $(Bi_2O_3)_{0.75}(Y_2O_3)_{0.25}$ and

$(Bi_2O_3)_{0.75}(Er_2O_3)_{0.125}(Y_2O_3)_{0.125}$. For reason of the stability of the oxides and hydroxides, a high pH value was chosen (11.5) and precipitation was obtained by pouring, drop by drop, a nitrate solution of precursors (0.1mol/L) in an aqueous solution of ammonia (50mL in 550mL). From TG-MS, XRD and Raman spectrometry, annealing conditions were optimized. The most homogeneous powders were obtained when the precipitate was filtered and annealed at 500°C for 3 hours. Although nitrates remained in the sample, their amount was less than 4.8%. From the crystallographic point of view, the obtained powders were mainly in the β-form although one can not discard the possibility of δ-form in the mixture. As shown by combining XRD and TEM, for all compositions, single crystal grains with size of about 20nm were obtained.

References

[1] Chen DR, Xie JL, Li B, Sun SL, Xu RR. *Journal of Shandong University*, 1997, **32**(1): 88.

[2] Madler L, Pratsinis SE. *J. Am. Ceram. Soc.*, 2002, **85**(7): 1713.

[3] Wang YY, Wang SF, Qin YH, Shu YD. *Coating Industry*, 2001, **5**: 1.

[4] Sun LW, He Y, Fu YD, Zhang C. *Journal of Transducer Technology*, 2000, **19**(1): 21.

[5] Shi XC, Xiao ZW, Qin YH. *Hunan Nonfereous Metals,* 2003, **19**(4): 15.

[6] Dos Santos SI, Balachandran U, Guttschow RA, Poeppe RB. *J.Non-Cryst. Solids*, 1990, **121**: 448.

[7] Wang YY, Peng WJ, Chai LY. *J.Cent. South. Univ. Technol.,* 2004, **11**: 410.

[8] He WM, Zhen Q, Pan QY, Liu JQ. *Journal of Functional Materials*, 2003, **34**: 702.

[9] Kumada N, Takahashi N, Kinomura N. *J Solid State Chem.*, 1998, **139**(2): 321.

[10] Yao YB. Handbook of Chemistry and Physics. Shanghai Scientific and Technical Publisher, Shanghai, 1985, 12.

[11] Kodama H. *J. Solid State Chem.*, 1994, **112**: 27.

[12] Rodriguez-Carvajal J. *Physica B.*, 1993, **192**: 55.

[13] Blower SK, Greaves C. *Acta Cryst C.* 1988, **44**: 587.

[14] Harwig HA. *Zeitschrift für Anorganishe and Allgemeine Chemie,* 1978, **444**: 151-166.

[15] Williamson GK, Hall WH, *Acta Metallurgica*, 1953, **1.**

Chapter 3

Process of dense $(Bi_2O_3)_{0.75}(Ln_2O_3)_{0.25}$ (Ln=Y, Er, Dy) solid electrolyte

Dense ceramics can be obtained by conventional sintering (i.e. sintering realized under atmospheric pressure, it will be called pressureless sintering). High temperatures close to the material melting point and long term annealing are usually associated with this technique, which leads to ceramics with large grain size. To avoid the grain growth, hot pressure sintering is widely used. It allows a reduction of porosity and leads to high densification without obvious grain growth. Using this method, Bourell *et al.*[1] obtained fully dense ceramic of ZrO_2-3mol%Y_2O_3 with grain size of 80-90nm at 23Mpa. Dong *et al.* [2] fabricated SiC ceramic with grain size smaller than 100nm by sintering at 1850°C under 200MPa for 1h. Ultra high pressure sintering is also an effective method to get nanocrystalline ceramic. Yuan *et al.* [3] sintered Y_2O_3 stabilized ZrO_2 nano-powders at 1000-1200°C under 4GPa for 2min, the final product had a relative density of 99.3%. Beside these, dense nano crystalline Bi_2O_3-HfO_2-Y_2O_3 ceramic were obtained by microwave plasma sintering [4]. Sparking plasma sintering is also an effective way, which will be introduced later.

In this work, spark plasma sintering was preferred to fabricate ceramic with smallest grain size while pressureless sintering was applied to obtain samples with larger grain size.

3.1 Sintering method

3.1.1 Pressureless sintering

Pressureless sintering is a basic method of sintering, which is widely used in the industry. The green sample is firstly compacted in its final shape by different forming methods. It is then sintered at given temperature without application of external pressure. The optimal temperature for sintering can be easily deduced from the shrinkage curve of a green pellet. In this method, sintering temperature and time, particle size of powder and properties of green compact are factors which affect the performance of final product. In order to obtain nanocrystalline ceramics, using powders with fine particle size as raw material, the sintering temperature must be controlled to obtain samples with high compactness and avoid the grain growth of samples. Using pressureless sintering, Vladimir *et al.*[5] managed to obtain 3-30mol% Al doped ZrO_2 ceramic with grain size of 45nm.

If during the heating process, the components in the green compact react to form a new substance, the technique is called pressureless reaction sintering. The advantage is that it allows the formation of the desired material directly, and because the sintering process is simplified, grain growth can be avoided.

Using conventional sintering, Zhen *et al.*[6] managed to obtain dense $(Bi_2O_3)_{0.75}(Y_2O_3)_{0.25}$ ceramic (relative density nearly 96%) with grain size lower than 100nm. Nanopowders were prepared by reverse titration co-precipitation and annealed at 430^oC before sintering. A mixture of β-Bi_2O_3 and Y_2O_3 was obtained, under pressureless reactive sintering at 550^oC, 600^oC and 650^oC, it subsequently transformed to a δ-Bi_2O_3 solid solution.

3.1.2 Spark plasma sintering

Spark plasma sintering (SPS), which was recently developed for the fabrication of ceramics and composites, is a rapid solidification technique where high quality and uniform compacts can be sintered rapidly at comparatively low temperatures when compared to conventional sintering methods.

In this method, a graphite die is used, which is placed in the centre of a press in a cabin. The powder is pressed uniaxially and direct pulse current is applied as shown in Fig.3.1. The most important character of SPS is that the powder is heated by spark discharge, thus the heating and cooling rate can reach up to 1000K/min. Therefore the sintering process can be very fast in few minutes. This character ensures high compactness of sample, and limits grain growth. Thus, the SPS method has been widely used in fabrication of nano ceramic, especially materials with high melting points.

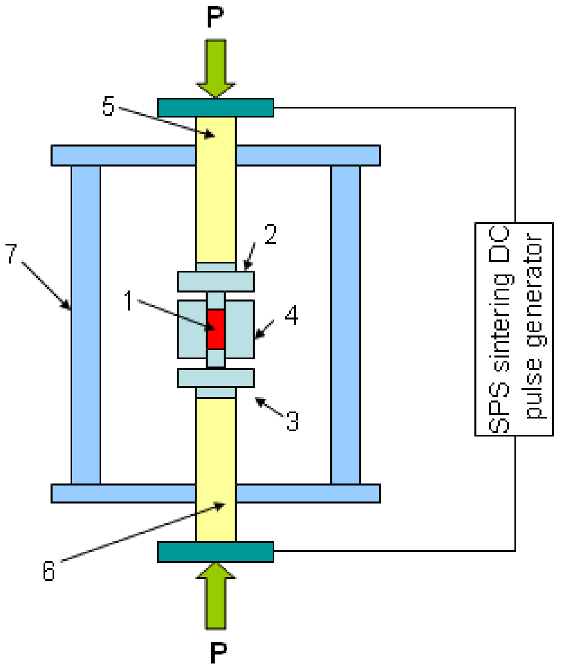

1-powder 2,3-upper,lower punch 4- sintering die
5,6-upper,lower punch electrode
7-vacuum & water cooling chamber

Fig.3.1 Schematic of the SPS device

3.2 Experimental

3.2.1 Sample preparation

Nanopowders obtained in chapter 2 were sintered by SPS and conventional sintering. Green bodies for conventional sintering were prepared by uniaxial pressing at very low pressure followed by cold isostatic pressing at 170MPa for 10 minutes. The body density was around 60% of the theoretical density.

Prior to the sintering experiments, DTA were performed on a Setaram 92 TG-DTA with a heating rate of 5^{o}C/min to determine the melting point of each composition and therefore the limit temperature for sintering. The melting points are given in table 3.1, and show rather refractory compounds for bismuth based materials.

Table 3.1 Melting points of the investigated compositions

	Melting point (^oC)
$(Bi_2O_3)_{0.75}(Dy_2O_3)_{0.25}$	1100
$(Bi_2O_3)_{0.75}(Y_2O_3)_{0.25}$	1185
$(Bi_2O_3)_{0.75}(Er_2O_3)_{0.25}$	1100
$(Bi_2O_3)_{0.75}(Er_2O_3)_{0.125}(Y_2O_3)_{0.125}$	1200

3.2.2 Densification

SPS experiments were performed at the French National platform at CIRIMAT in Toulouse, using the Dr. Sinter 2080 (syntex Inc. Japan) machine, the photos are shown in Fig.3.2. About 0.8g of powders were poured into a graphite die of 8mm diameter. The die wall and the punch surface were protected with graphite foils. A thermocouple was used to measure the temperature of the sample; it was introduced in a hole on the side of the graphite die. This temperature is used to present the sintering temperature of the powder, however the temperature of the sample inside the die is not known accurately. A difference between the “measured” temperature and the temperature of powder in SPS was pointed out by Wada *et al.*[7]. They measured the temperature of the silicon nitride powder in a die with a thermocouple and compared it with the temperature of the hole. The obtained results indicated that the temperature inside the die was about 150^{o}C higher than the temperature of the hole. In this part, the temperature given in sintering process for discussion below was the “measured” temperature.

Fig.3.2 The French National Spark Plasma Sintering Platform available at CIRIMAT in Toulouse, France

3.2.3 Characterization

The final density of pellets after sintering was measured by the Archimede method (see in Annex 3).

X-ray patterns of sintered samples were collected on a D8 Advance AXS Bruker diffractometer equipped with a Vantec1 detector ($\lambda_{CuK\alpha}$=1.5406Å). Data was collected in the $20^o \leq 2\theta \leq 80^o$ domain, with a 0.0148° step size and a counting time of 0.5 sec per step. A diagram was collected in 42′05″. The crystallite size were calculated using the Scherrer Equation ($D=0.89\lambda/\beta\cos\theta$) where β is the full width at half maximum of Bragg peaks.

The surface of all sintered samples was attacked with 20% HF and Scanning Electron Microscopy (JSM-6700F) was used to observe their microstructure.

3.3 Result and analysis

3.3.1 Spark plasma sintering

3.3.1.1 Optimization of sintering condition

SPS is usually performed under vacuum, however a small Ar pressure can be introduced in the chamber. First experiments were performed with the $(Bi_2O_3)_{0.75}(Dy_2O_3)_{0.25}$ nano-powder annealed at 500°C for 3 hours. The main difficulty here was the risk of reduction of Bismuth oxide into Bismuth metal which is liquid at 271°C. Therefore, to optimize the conditions of sintering, a first experiment was carried out under a 2-3Pa Ar pressure, under a load of 50MPa, with a heating rate of 100°C/min.

Fig.3.3 shows the corresponding linear shrinkage curves. Under 50MPa, from room temperature to 200°C, a displacement of 0.37mm was observed. It was caused by the applied load, which led to a compaction of the powder. The real shrinkage started at 400°C and ended at 550°C, the maximum displacement was 1.43 mm. At about 700°C, an accident in the shrinkage curve was evidenced, fumes were also noticed and the experiment was stopped at 900°C and the sample allowed to cool down. Small balls of bismuth metal were found at the edge of the graphite die and confirmed the reduction of bismuth (Fig. 3.4).

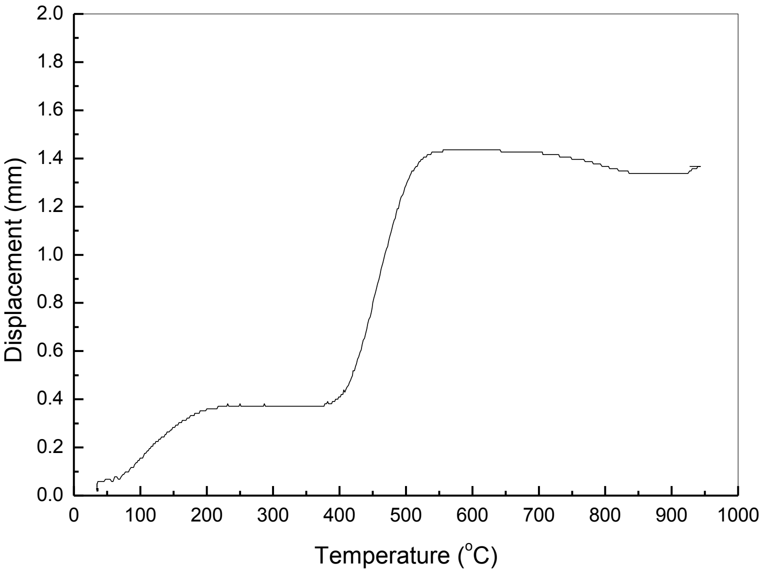

Fig.3.3 Linear shrinkage curve of $(Bi_2O_3)_{0.75}(Dy_2O_3)_{0.25}$ under 50MPa and a Ar pressure of 2-3Pa at 100°C/min heating rate

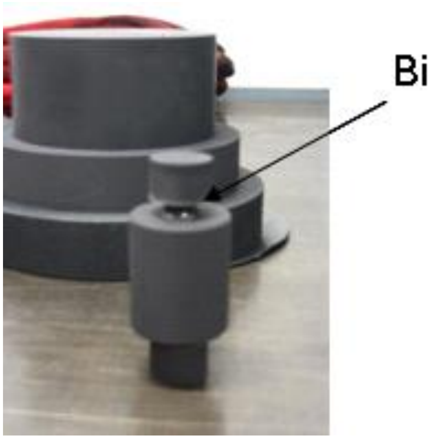

Fig.3.4 Evidence of bismuth balls after the first sintering trial

To avoid the reduction of bismuth, another experiment was therefore performed up to 700°C but, to help for sintering, the load was increased to 100MPa. The linear shrinkage behavior was similar to that under 50MPa. No reduction of Bismuth was to be noticed and the relative density of the pellet was 92% after sintering.

In both cases, the maximum of shrinkage rate occurred around 460°C, however, in order to insure higher compactness, a third experiment was carried out in the same conditions (heating rate: 100°C/min, strength:100MPa) with a plateau of 3 minutes at 500°C. A pellet with a relative density of 91% was obtained.

At that stage, considering that the release of water and CO_2 in the raw-powder decreased the compactness, it was decided to program a 5 minutes plateau at 300°C under air. However, in these conditions, the introduction of an Ar pressure during the sintering step was no more possible. Under vacuum, the oxygen partial pressure was about 10^{-11} bars. The stability of Bi_2O_3 systems was verified from thermodynamic calculation.

The predominance diagrams of Bi-O, Bi-Dy-O and Bi-Er-O systems are shown in Fig.3.5. Because of shortage of data, the calculation of Bi-Y-O and Bi-Er-Y-O systems was not possible.

It can be seen that when oxygen partial pressure is 10^{-11} bars, Bi_2O_3 is stable up to 530°C, then, it firstly reduced to BiO and further reduced to Bi at about 730°C. At lower oxygen partial pressure, reduction of Bi_2O_3 starts at lower temperature. However, in the case of $(Bi_2O_3)_{0.75}(Dy_2O_3)_{0.25}$ and $(Bi_2O_3)_{0.75}(Er_2O_3)_{0.25}$ solid solutions, under 10^{-11} bars, reduction of Bi_2O_3 occurs after 900°C. The activity of Bi_2O_3 is lower in the solid solution than in pure material, which makes it much stable. One can expect the same conclusion for the Bi-Y-O and Bi-Er-Y-O system.

It is worth noting that if one considers the real temperature of sample is higher than the measured temperature, the reduction of Bi_2O_3 observed at “measured” temperature of about 700°C was in agreement with this prediction from predominance diagram for Bi-Dy-O.

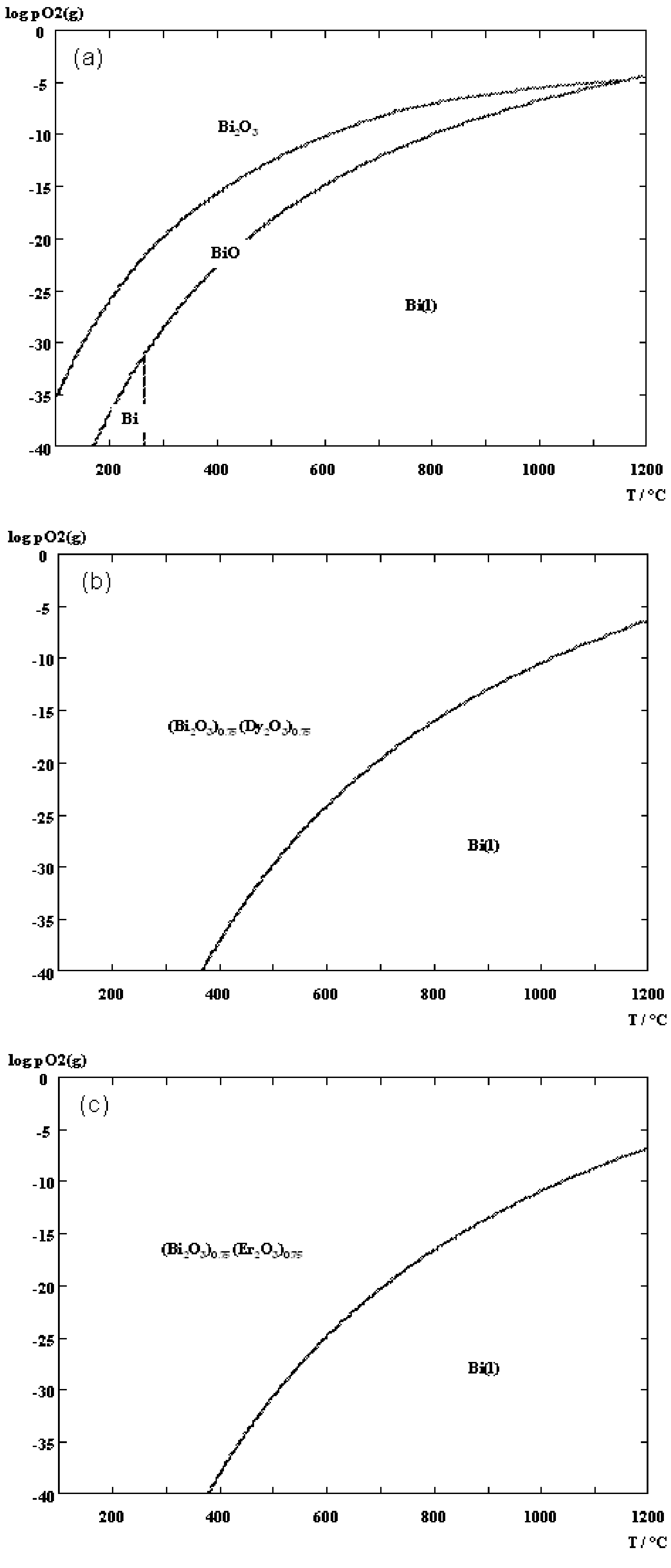

Fig.3.5 Predominance diagrams for Bi-O (a), Bi-Dy-O (b) and Bi-Er-O (c) systems

The program given in Fig.3.6 was therefore applied for sintering. The temperature was first increased to 300°C with a rate of 100°C/min and maintained at 300°C for 5 minutes in air under 2MPa during the first 7 minutes of experiment, the strength was then increased to 100MPa in 1 minute. After 6 minutes of experiment, air was pumped out and the following of the experiment was carried out under vaccum. After 5 minutes at 300°C, the temperature was increased to 500°C in 2 minutes and maintained at this temperature for 1 minute. The sample was then naturally cooled down to room temperature.

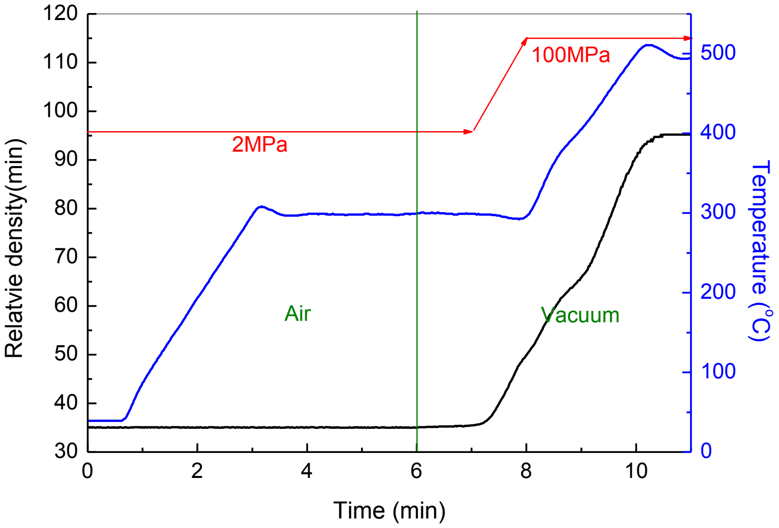

Fig.3.6 Temperature, pressure and relative density of sample as a function of sintering time

The relative density curve as a function of sintering time is also given in Fig.3.6. The shrinkage at 300°C is due to the increase of the applied pressure, and after 10 minutes the densification was finished, indicating that the sample was well sintered.

3.3.1.2 Characterizations of samples obtained by SPS

The sintering conditions shown in Fig.3.6 were applied to all compositions. Relative densities higher than 95% were obtained for all samples (Table 3.1).

Table 3.1 Relative density of all samples sintered by SPS

	Relative density (%)
$(Bi_2O_3)_{0.75}(Dy_2O_3)_{0.25}$	95.34
$(Bi_2O_3)_{0.75}(Y_2O_3)_{0.25}$	97.17
$(Bi_2O_3)_{0.75}(Er_2O_3)_{0.25}$	96.25
$(Bi_2O_3)_{0.75}(Er_2O_3)_{0.125}(Y_2O_3)_{0.125}$	95.82

Fig.3.7 gives the XRD patterns of all samples. Although powders displayed the β phase, all sintered samples correspond to δ phase. Stabilization of a δ phase is likely due to the fact that the actual temperature in the die may be higher than 500°C and the sintering was performed under vacuum which should decrease the temperatures of phase transition. The promotion of phase transition by SPS was also observed in literature.

From these XRD data, the crystallite size of each sample was deduced. The values are given in Table 3.2; the crystallite sizes of original powders are also given for comparison. The crystallite sizes of sintered samples were slightly larger than powders.

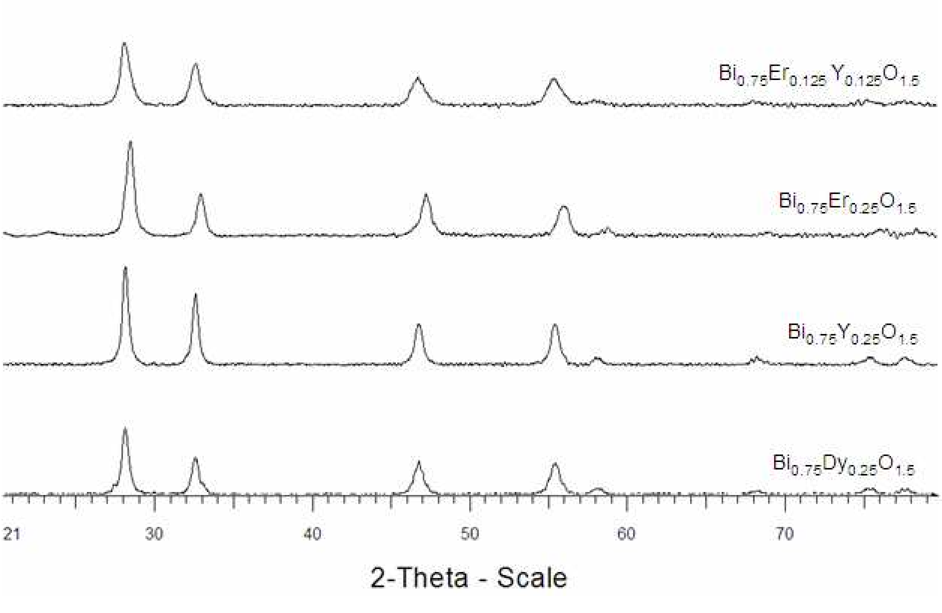

Fig.3.7 XRD patterns of all samples obtained by SPS

Table 3.2 Crystallite size (nm) of all samples after SPS

	Pellets after SPS	**Original powders**
$(Bi_2O_3)_{0.75}(Dy_2O_3)_{0.25}$	20	17
$(Bi_2O_3)_{0.75}(Y_2O_3)_{0.25}$	22	12
$(Bi_2O_3)_{0.75}(Er_2O_3)_{0.25}$	15	10
$(Bi_2O_3)_{0.75}(Er_2O_3)_{0.125}(Y_2O_3)_{0.125}$	11	11

The microstructure of Bi_2O_3-based nanocrystalline ceramics fabricated by SPS are shown in Fig.3.8. All samples exhibit a dense microstructure without residual porosity and virtual cracks. The average grain size of each sample is about 20nm, which is in good agreement with the size of crystallite and indicates single crystal grains.

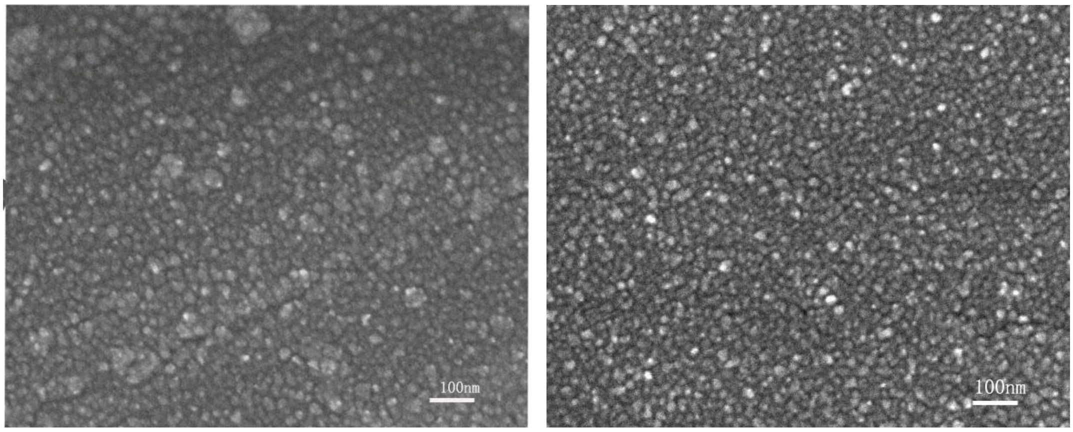

$(Bi_2O_3)_{0.75}(Dy_2O_3)_{0.25}$ $(Bi_2O_3)_{0.75}(Y_2O_3)_{0.25}$

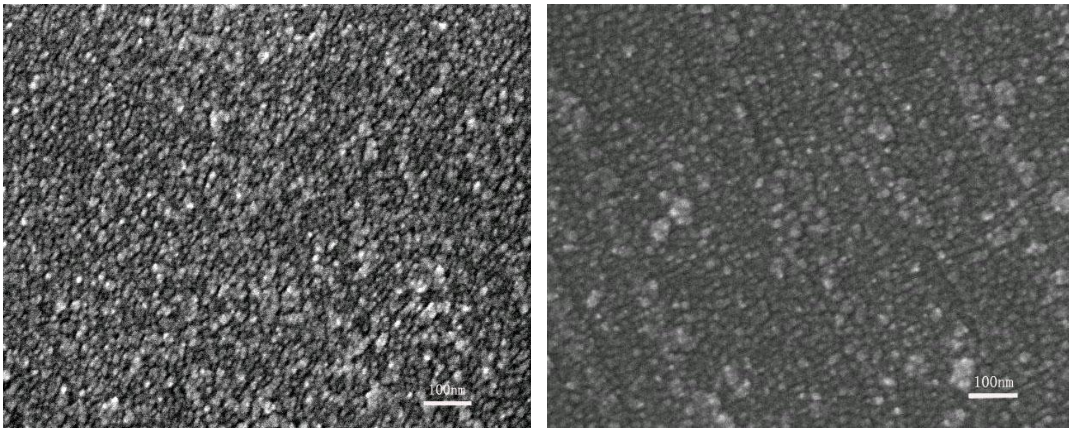

$(Bi_2O_3)_{0.75}(Er_2O_3)_{0.25}$ $(Bi_2O_3)_{0.75}(Er_2O_3)_{0.125}(Y_2O_3)_{0.125}$

Fig.3.8 Microstructure of Bi_2O_3-based nanocrystalline ceramics fabricated by SPS

3.3.2 Pressureless sintering

3.3.2.1 Shrinkage behaviour

With the aim to define the adequate temperature for pressureless sintering, dilatometry was performed on a green sample of each composition. Experiments were carried out on a Linseis L70 dilatometer under static air with a heating rate of 5°C/min. The shrinkage curves of all compositions are given in Fig.3.9.

Shrinkage started around 500°C for $(Bi_2O_3)_{0.75}(Y_2O_3)_{0.25}$, 525°C for $(Bi_2O_3)_{0.75}(Dy_2O_3)_{0.25}$, $(Bi_2O_3)_{0.75}(Er_2O_3)_{0.125}(Y_2O_3)_{0.125}$ and 575°C for $(Bi_2O_3)_{0.75}(Er_2O_3)_{0.25}$. $(Bi_2O_3)_{0.75}(Y_2O_3)_{0.25}$ and $(Bi_2O_3)_{0.75}(Dy_2O_3)_{0.25}$ exhibit a maximum shrinkage rate around 680°C and 700°C, respectively, while $(Bi_2O_3)_{0.75}(Er_2O_3)_{0.125}(Y_2O_3)_{0.125}$ and $(Bi_2O_3)_{0.75}(Er_2O_3)_{0.25}$ show two maximum rates at 630°C, 780 °C and 670°C, 780°C, respectively.

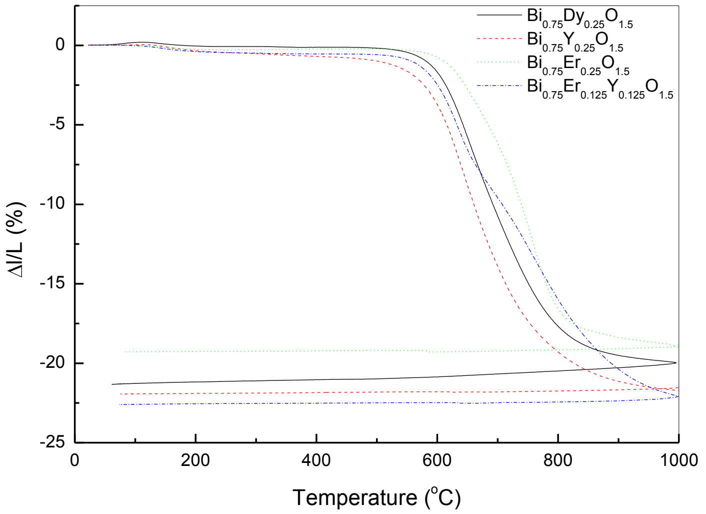

Fig.3.9 Linear shrinkage curves of all samples at 5°C/min heating rate

3.3.2.2 Grain growth behavior

X-ray diffraction was performed on the $(Bi_2O_3)_{0.75}(Dy_2O_3)_{0.25}$ sample sintered at 650°C, 700°C and 750°C for different time. A δ form was obtained for almost all compositions except samples sintered at 650°C, in which traces of rhombohedral β_2-type phase were observed. The formation of this secondary phase is not surprising. It is in good agreement with the X-ray diffraction study which was performed at variable temperatures on precursor in chapter 2. Despite this impurity, the variations of the crystallite size of δ form as a function of time was deduced for each temperature (Fig.3.10). It can be seen that the variation in function of the sintering time follows a parabolic trend.

Depending on the sintering temperature, the rate of grain growth increases from a low value at 650°C to an extremely high value at 750°C.

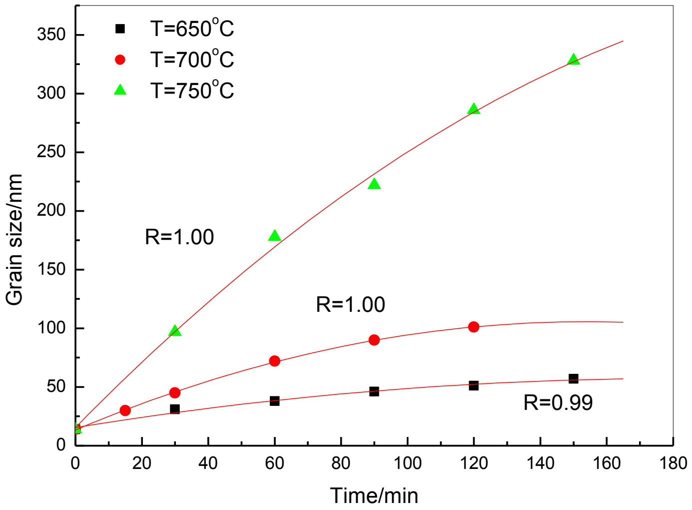

Fig.3.10 Variation of crystallite size versus time of $(Bi_2O_3)_{0.75}(Dy_2O_3)_{0.25}$ samples sintered at 650°C, 700°C and 750°C

The variation of crystallite size in a sintering process can be expressed by:

$$D^n - D_o^{\,n} = kt \tag{3.1}$$

where k is a constant; D is the average crystallite size after sintering; D_0 is the average initial crystallite size; t is the sintering time. Here, the value of D_0 is 17 nm, which corresponds to the average crystallite size of the nanopowder calcined at 500°C for 3h. The exponent, n, characterizes the rate controlling process: for n=2, grain growth is controlled by grain boundary diffusion, for n=3 grain growth is controlled by volume diffusion or diffusion through liquid, and for n=4 grain growth is controlled by surface diffusion.

Using the grain size data in Fig.3.10, and Eqs.(3.1), the best linear regression was found for n=2 at each temperature (with R=0.9991 at 650°C, R=0.9962 at 700°C, R=0.9874 at 750°C). It means that the grain growth of $(Bi_2O_3)_{0.75}(Dy_2O_3)_{0.25}$ sample is controlled by mass transport through the grain boundary.

The calculation led to the following equations representing the grain growth in $(Bi_2O_3)_{0.75}(Dy_2O_3)_{0.25}$ at the three different sintering temperatures.

$$650^{o}\mathrm{C}:\ D^2 - D_0^2 = 19.42t \tag{3.2}$$

$$700^{o}\mathrm{C}:\ D^2 - D_0^2 = 87.64t \tag{3.3}$$

$$750^{o}\mathrm{C}:\ D^2 - D_0^2 = 734.51t \tag{3.4}$$

From the above equations, the rate constants for grain growth are 19.42, 87.64 and 734.51 nm^2/min at 650, 700, and 750^{o}C, respectively. According to the Arrhenius equation, the rate constant can be expressed as a function of the reciprocal of the absolute temperature according to the expression:

$$K = K_0 \exp(\frac{-\Delta E}{RT}) \tag{3.5}$$

where K is the rate constant of grain growth, K_0 is a pre-exponential constant, ΔE is apparent activation energy, R is the universal gas constant and T is the absolute temperature.

Rearranging the above equation gives,

$$\ln K = \ln K_0 + (\frac{-\Delta E}{RT}) \tag{3.6}$$

According to Eq.(3.6), the relationship between ln(K) and1000/T is expected to be linear. This linear relationship is shown in Fig.3.11, which can be represented by the expression:

$$\ln K = 39.87 - 34.18\frac{1000}{T} \tag{3.7}$$

Eq.(3.7) yields the apparent activation energy (ΔE) for the grain growth of nanocrystalline $(Bi_2O_3)_{0.75}(Dy_2O_3)_{0.25}$ to be equal to 284 kJ/mol.

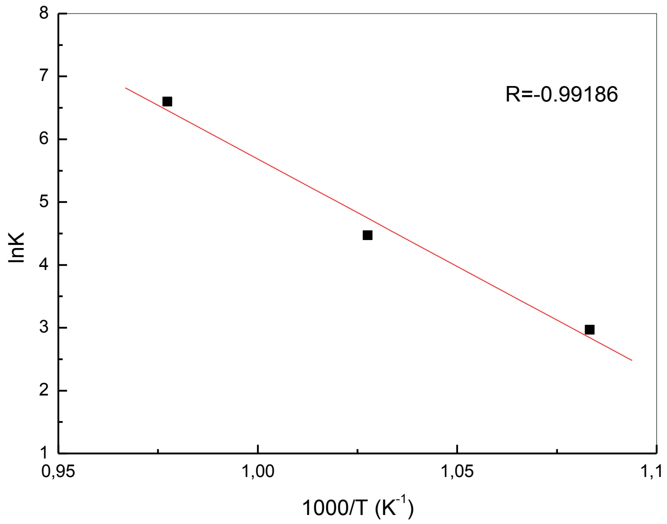

Fig.3.11 Variation of lnK as a function of 1000/T for $(Bi_2O_3)_{0.75}(Dy_2O_3)_{0.25}$ samples

From the above results, samples with different grain size can be obtained by controlling temperature and sintering time. However, for the application, high relative density is needed. The relative density versus sintering time at 650°C, 700°C and 750°C will be discussed in the following part.

3.3.2.3 Density variation

The variation of the density of $(Bi_2O_3)_{0.75}(Dy_2O_3)_{0.25}$ nano crystalline samples as a function of sintering time at 650°C, 700°C and 750°C is given in Fig.3.12. At these temperatures, the change rate of the relative density was extremely rapid in the early stage, and slowed down after 1h. At 650°C, relative density of only 92% were obtained, whereas after sintering at 700°C for 2h or 750°C for 1h, it reached 94%. Only these latter pellets will be kept for the conductivity measurements.

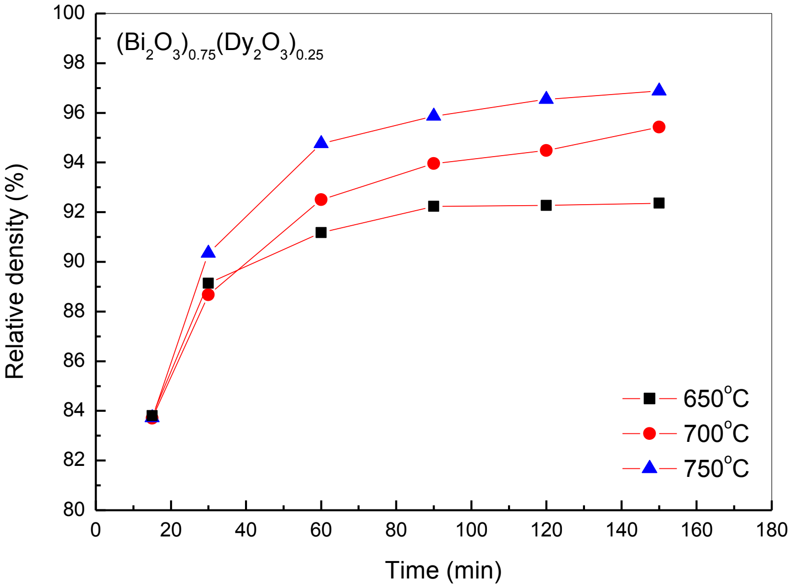

Fig.3.12 Relative density of $(Bi_2O_3)_{0.75}(Dy_2O_3)_{0.25}$ samples as a function of time at 650°C, 700°C and 750°C

3.3.2.4 Sample sintering

According to the study on relative density and grain growth behavior, pellets of all compositions were sintered at 700°C for 2h, 750°C for 1h and 800°C for 1h in order to prepare dense ceramics with different grain sizes. The grain sizes of all pellets were calculated using the Scherrer Equation, they are shown in Table 3.3.

Table 3.3 Crystallite size (nm) of all samples sintered at different temperatures

	700°C, 2h	**750°C, 1h**	**800°C, 1h**
$(Bi_2O_3)_{0.75}(Dy_2O_3)_{0.25}$	101	178	402
$(Bi_2O_3)_{0.75}(Y_2O_3)_{0.25}$	62	81	104
$(Bi_2O_3)_{0.75}(Er_2O_3)_{0.25}$	86	192	263
$(Bi_2O_3)_{0.75}(Er_2O_3)_{0.125}(Y_2O_3)_{0.125}$	78	105	585

In order to compare with microcrystalline sample, powder with microcrystalline were first prepared by solid reaction method. Bi_2O_3 and Dy_2O_3 were homogeneously mixed and annealed at 800°C for 8h, then the powder was pressed into pellets and sintered at 900^{o}C for 2h. After sintering, samples with relative densities of 96% were obtained.

3.3.2.5 Microstructure

The typical high magnification microstructures of $(Bi_2O_3)_{0.75}(Dy_2O_3)_{0.25}$ sintered samples are shown in Fig.3.13. Each sample exhibits a dense microstructure without obvious porosity. Samples prepared with nanopowders display grains with size of about 100 and 400nm for samples sintered at 700 and 800°C, respectively, which is in agreement with the value from XRD. An average grain size of 2µm was observed for the sample sintered at 900^{o}C, prepared from microcrystalline powders.

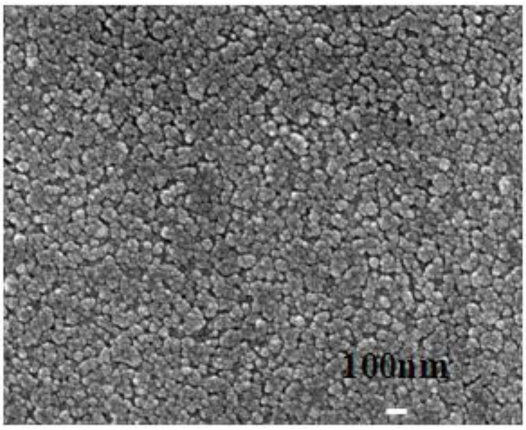

$(Bi_2O_3)_{0.75}(Dy_2O_3)_{0.25}$ sintered at 700°C for 2h

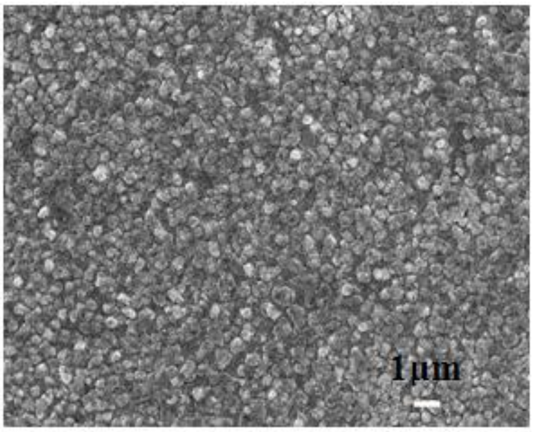

$(Bi_2O_3)_{0.75}(Dy_2O_3)_{0.25}$ sintered at 800°C for 1h

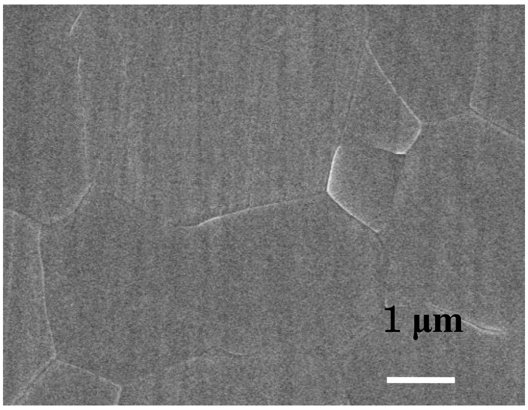

$(Bi_2O_3)_{0.75}(Dy_2O_3)_{0.25}$ sintered at 900°C for 2h

Fig.3.13 Microstructure of $(Bi_2O_3)_{0.75}(Dy_2O_3)_{0.25}$ sintered pellets at different temperatures

3.3.2.6 Stability

As shown by X-ray diffraction, δ forms were stabilized for all compositions. However, as shown for Er[10], Y[11] substituted compounds, these forms are likely to be metastable with a transformation nearby 600°C. However, as mentioned in §**1.2**, one could expect a better stability for ceramics with small grain size or at least, stabilization of high temperature polymorphs at lower temperatures.

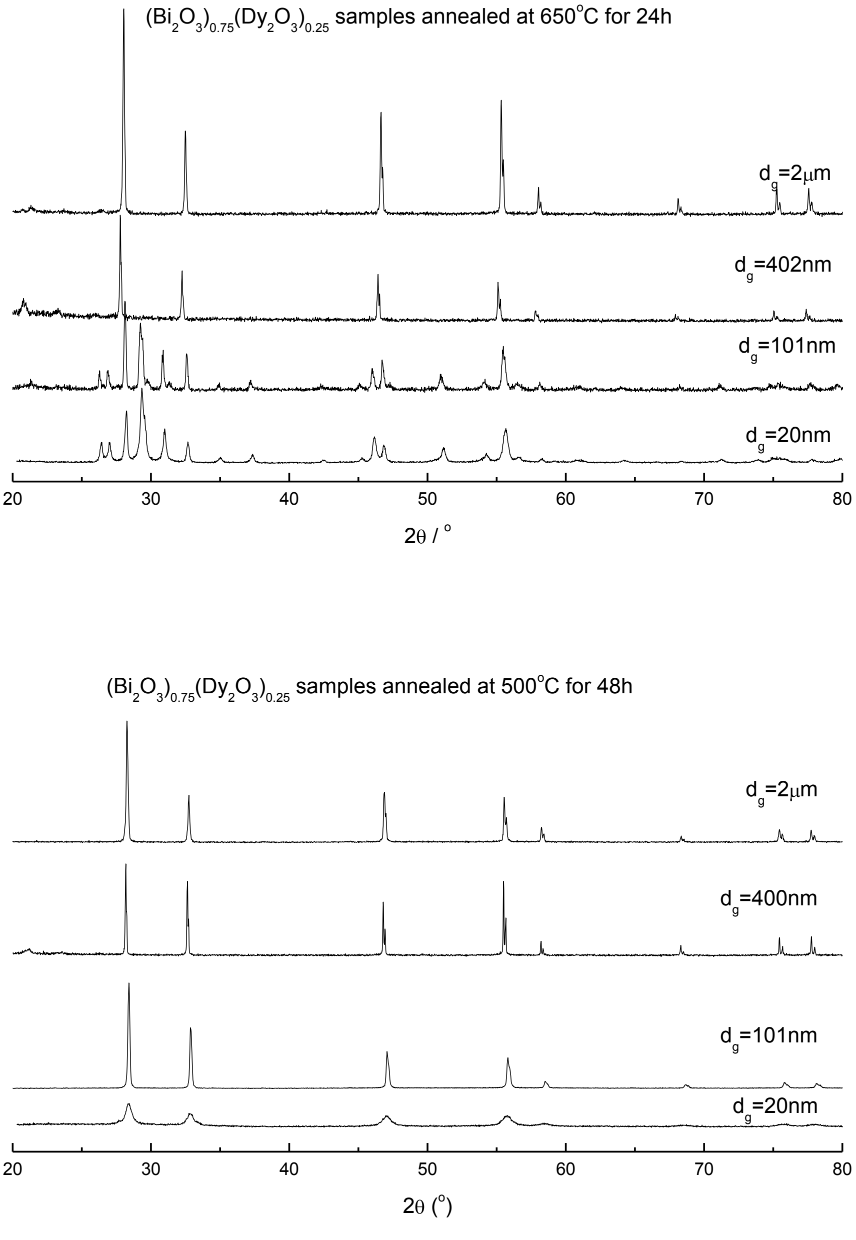

Fig.3.14 XRD patterns of $(Bi_2O_3)_{0.75}(Dy_2O_3)_{0.25}$ samples after annealing at 650°C for 24h and after annealing at 500°C for 48h

In order to check the stability of samples with different grain size, $(Bi_2O_3)_{0.75}(Dy_2O_3)_{0.25}$ pellets with grain size d_g=20nm, 101nm, 400nm and 2μm, were annealed at 650°C for a long time. In contrast to what was expected, samples with the smaller grains (d_g=20, 101nm) appeared to be metastable. The δ form already transformed into β_2 form partly after only 24h annealing at 650°C, while other two samples kept their δ form (Fig.3.14). The stability of samples at 500°C was also investigated, after 48h annealing, all samples exhibited δ form and no β_2 form was observed.

3.4 Conclusion

Using the nano-powders annealed at 500°C for 3 hours, pellets with different grain size were prepared by SPS and pressureless sintering.

According to the predominance area diagram of Bi-O, Bi-Dy-O, Bi-Er-O and shrinkage curves, the conditions of SPS were optimized for composition $(Bi_2O_3)_{0.75}(Dy_2O_3)_{0.25}$. These conditions were then applied to the other compositions. Dense ceramics with relative density higher than 94% were obtained at 500°C for 1 min by SPS, and XRD showed that all samples exhibit the δ form with grain size of about 20nm.

Samples with relative density higher than 94% were also obtained by pressureless sintering. However, higher temperature was needed and grain growth was observed. As shown by the evolution of grain sizes with sintering time, the grain growth is controlled by mass transport through the grain boundaries. Thus, dense ceramics with different grain size were prepared by varying the sintering temperature. Sintering was performed at 700°C for 2 hours, 750°C for 1 hour and 800°C for 1 hour. This led to samples with grain size varying from 60nm to 500nm, depending on the sintering temperature and composition.

At this stage, a range of dense ceramics with different grain size was obtained. The stability of $(Bi_2O_3)_{0.75}(Dy_2O_3)_{0.25}$ pellets was checked at 650°C but, in contrast to what was expected, a better stability was observed for ceramics with large grain size and ceramics with grain size lower than about 100nm transformed into a β_2 form. However, a better stability was noticed at 500°C. Then, impedance spectroscopy was carried out on these samples, being aware of a risk of metastability above 500°C.

References

[1] Bourell DL, Kaysser PW. *J Am Ceram Soc.*, 1993, **76**(3): 705.

[2] Dong SM, Jiang DL, Tan SH, Gou JK. *Journal of Inorganic Materials*, 1997, **12**(2): 191.

[3] Yuan WZ, Tian W, Guo J, *et al. Journal of High Pressure Physics*, 2001, **15**(4): 259.

[4] Zhen Q, Kale GM, *et al. Chemistry of Materials,* 2007, **19**:.

[5] Srdic VV, Winterer M, Hahn H. *J.Am.Ceram.Soc.*, 2000, **83**(8): 1853.

[6] Zhen Q, Kale GM, *et al. Solid State Ionics*, 2005, **176**: 2727.

[7] Wada S, Suganuma M, Kitagawa Y, Murayama N. J. Ceram. Soc. Jpn., 1999, **107**: 887.

[8] Ye F, Liu LM, Zhang JX, Meng QC. *Composites Science and Technolog*, 2008, **68**: 1073.

[9] Luan WL, Gao L, Kawaoka H, Sekino T, Niihara K. *Ceramic International*. 2004, **30**: 405.

[10] Kruidhof H, Bouwmeester HJM, De Vries KJ, Gellings PJ, Burggraaf AJ. *Solid State Ionic*, 1992, **50**: 181.

[11] Kruidhof K, De Vries KJ, Burggraaf AJ. *Solid State Ionic*, 1990, **37**: 213.

Chapter 4

Effect of grain size of dense ceramics on the ion conductivity of Bismuth-based solid electrolytes

Electrochemical Impedance Spectroscopy is a powerful technique for the characterization of electrochemical systems. It was here applied to study the effect of grain size of bismuth-based ceramics on oxide ion conductivity.

4.1 Electrochemical Impedance Spectroscopy (EIS)

From an electronic point of view, oxide ion conductive ceramics behave as a capacitor in parallel with a resistance. Therefore the electrical characterization of such materials can not be performed with Direct Current and Alternating Current must be applied to derive the impedance Z(ω). EIS is usually measured by applying a sinusoidal potential excitation:

$$E(\omega) = E_0 e^{j\omega t} \tag{4.1}$$

where E(ω) is the potential at time t, E_0 is the amplitude of the signal, and ω is the relaxation frequency (ω=2πf). The response signal, I(ω) is shifted in phase (ϕ) and has a different amplitude, I_0.

$$I(\omega) = I_0 e^{j(\omega t + \phi)} \tag{4.2}$$

By varing the frequency of the applied signal, one can get the impedance of the system as a function of frequency.

In polar coordinate, the impedance is given by:

$$Z(\omega) = Z_0 e^{-j\omega} \tag{4.3}$$

where Z_0 is the magnitude of the impedance and ϕ is the phase shift.

In cartesian coordinate, the impedance is given by:

$$Z(\omega) = Z' + jZ'' \tag{4.4}$$

where Z' is the real part of the impedance and Z'' is the imaginary part. ($j = \sqrt{-1}$). Here the two rectangular coordinate values are clearly.

$$Z' = |Z|\cos\phi \quad Z'' = |Z|\sin\phi \tag{4.5}$$

With the phase angle

$$\phi = \tan^{-1}(Z''/Z') \tag{4.6}$$

and the modulus

$$|Z|^2 = (Z')^2 + (Z'')^2 \tag{4.7}$$

The plot of the real part of impedance against the opposite imaginary part gives the Nyquist plot.

The advantage of the Nyquist representation is that it gives a quick overview of the data and allows quantitative interpretation. However, when plotting data in the Nyquist format, the real axis must be equal to the imaginary axis, so as not to deform the shape of the curve. The disadvantage of the Nyquist representation is one loses the frequency dimension of the data, therefore the frequency is usually labeled on the diagram.

In case of a resistor placed in parallel with a capacitor (as shown in Fig.4.1),

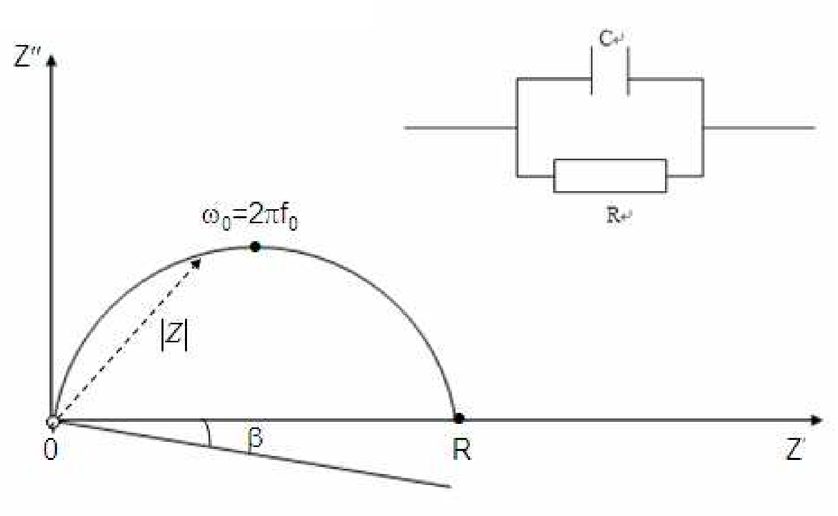

Fig.4.1 Simple equivalent of a RC parallel circuit
and its corresponding Nyquist diagram

The impedance of the circuit is given by:

$$\frac{1}{Z}=\frac{1}{R}+jC\omega \qquad \Rightarrow \qquad Z=\frac{R}{1+R^2C^2\omega^2}-j\frac{R^2C\omega}{1+R^2C^2\omega^2} \tag{4.8}$$

One can easily demonstrate the equation of the Nyquist plot in this case, which is that of a circle of radius R/2 with a frequency $\omega_0=1/RC$.

$$Z=\frac{R}{1+(\omega/\omega_0)^2}-j\frac{R(\omega/\omega_0)}{1+(\omega/\omega_0)^2} \tag{4.9}$$

From these data, the resistance R corresponds to the intercept with the real axis, and the capacitance C is derived from ω_0.

However, in a ceramic, the phenomena are slightly more complicated. In absence of porosity, the ceramic can be described as grains of given size connected to each other by grain boundaries.

Moreover to carry out the experiment, electrode (usually gold or platinum) must be added at the surface. The whole can be modeled with (R//C) circuits in series and three circles should be observed in the Nyquist representation (Fig.4.2).

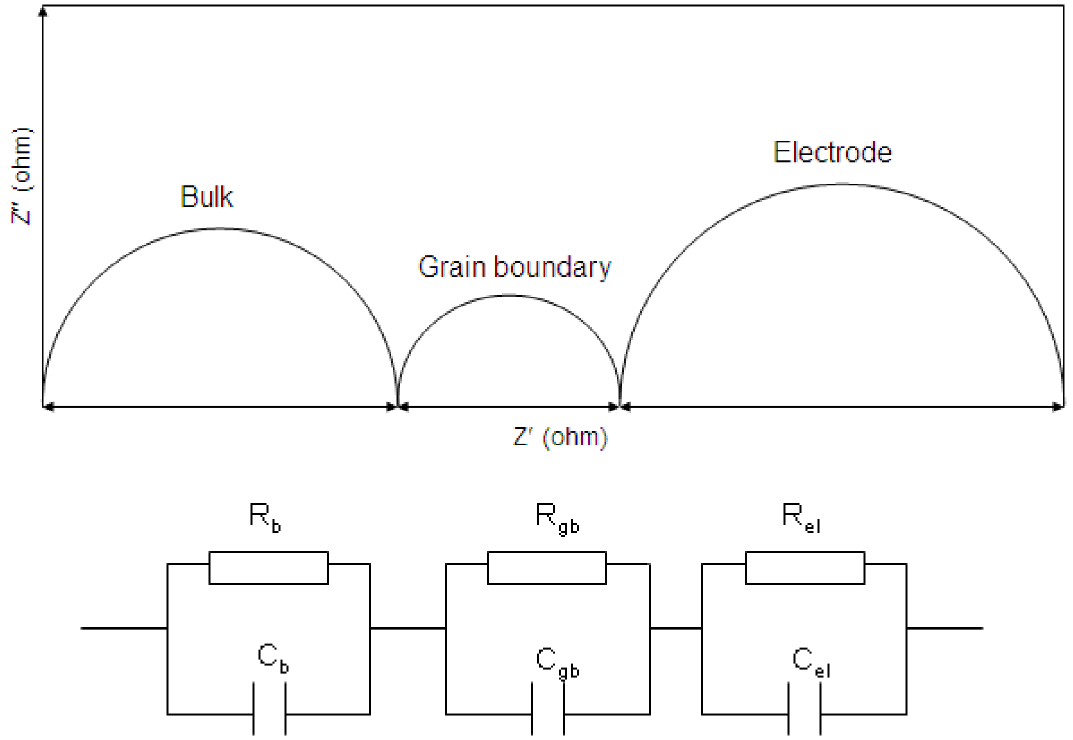

Fig.4.2 Theoritical Nyquist diagram for a solid electrolyte with the corresponding equivalent circuit

Knowing the thickness (e) and surface (S) of sample, the resistance is a function of the conductivity and the capacitance is a function of the dielectric constant of the material as follows:

$$R = \frac{1}{\sigma}\cdot\frac{e}{S} \qquad C = \varepsilon\varepsilon_0\frac{e}{S} \qquad (4.10)$$

where ε_0 is the permittivity of vacuum ($\varepsilon_0=8.8592\times10^{-10}\mathrm{Fcm}^{-1}$).

The capacity of the bulk which corresponds to the transgranular polarization is usually in the order of 10^{-12}-10^{-11}F, that related to the intergranular polarization is in the order of 10^{-9}F and electrode polarization is around 10^{-5}, 10^{-6}F. In Nyquist representation, the bulk response is therefore expected at high frequency, and the electrode response at low frequency.

Modeling an electrochemical phenomenon with an ideal capacitor assumes that the surface under investigation is homogeneous which is not the case and a CPE (Constant Phase Element) is usually used instead of a capacitance:

$$Z = \frac{R}{1 + RY_0(j\omega)^n} \tag{4.11}$$

where Y_0 is the ideal capacitance and n is an experimental constant, $0 \leq n \leq 1$. When n=1, CPE acts as an ideal capacitor.

The fitting procedure also leads to the relaxation frequency, f_0, and depression angle, β, according to the following relationships:

$$f_0 = 1/[2\pi(RY_0)^{1/n}] \tag{4.12}$$

$$\beta = (1-n)\pi/2 \tag{4.13}$$

The depression angle can be interpreted in terms of the heterogeneity of the examined property. A high β value indicates higher heterogeneity.

To model the diffusion of ionic species at the interface of the electrode, a Warburg Impedance, Z_{war}, is commonly used. Several expressions, based on different assumption of infinite diffusion layer are given:

$$Z = R/\sqrt{j\omega} \tag{4.14}$$

where R is the diffusion resistance. Under the assumption of a finite diffusion layer thickness, the impedance is

$$Z = R\frac{\tanh\sqrt{j\omega t}}{\sqrt{\tau}} \qquad \tau = \frac{\delta^2}{D} \tag{4.15}$$

where R is the diffusion resistance, τ is the diffusion time constant, δ is the diffusion layer thickness, D is the diffusion coefficient.

In solids, the mobile oxide ion is thermally activated with temperature, and conductivity follows the following equation:

$$\sigma T = A \times \exp\left(\frac{-E_a}{kT}\right) \tag{4.16}$$

where E_a is the activation energy which corresponds to the energy which must be given to the system to extract the ion from its potential hole.

4.2 Experimental

Electrical properties were characterized by impedance spectroscopy. A stainless steel sample holder equipped for 3 samples was used (Fig.4.3). Samples were placed on a gold counter electrode. A gold plate, used as current collector, was pressed on the top of each sample by the means of alumina tubes maintained with springs. The whole was placed in a resistive furnace; temperature was controlled with a type K thermocouple, placed at the vicinity of samples. To allow a good contact with the gold current collector, gold electrodes were deposited on both surfaces of the pellets by painting a gold paste. To define the lower temperature at which the gold paste could be annealed, a TG-DTA analysis was carried out on the gold paste under air with a heating rate of 5°C/min. The corresponding curves are given in Fig.4.4. It was found that no weight loss was observed after 400°C, therefore the samples painted with the gold paste were sintered at 400°C for 30min to obtained the gold electrolytes.

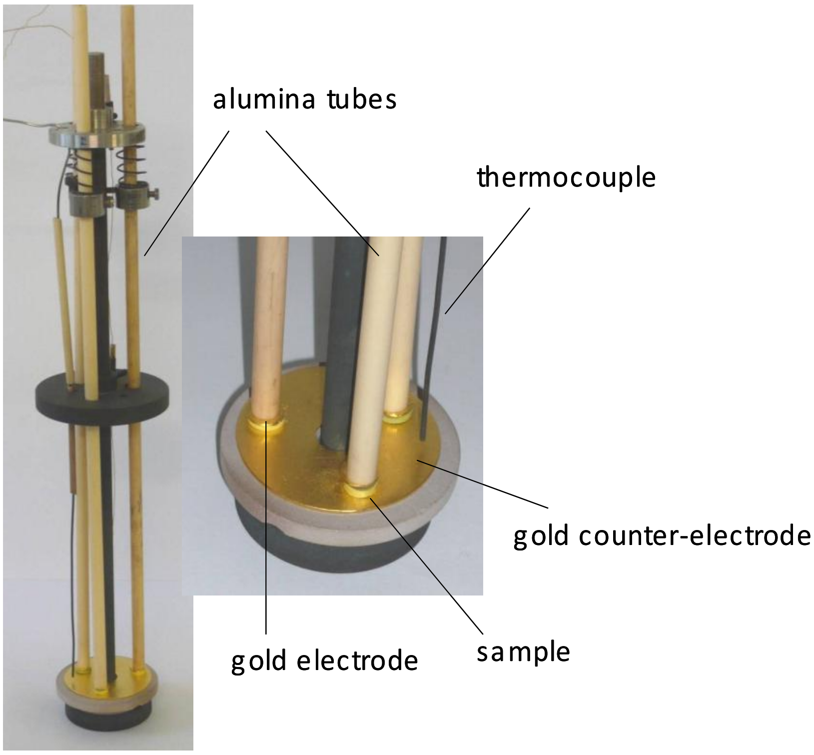

Fig.4.3 The experimental cell which was used for impedance measurements

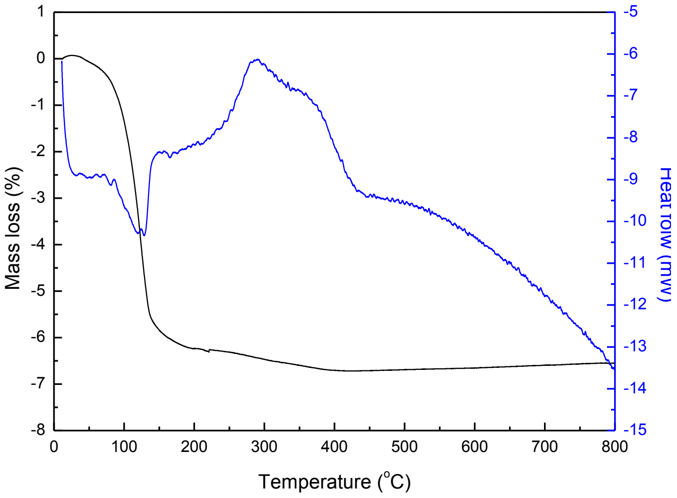

Fig.4.4 TG-DTA curves of the gold paste under air with a heating rate of 5°C/min

A first set of experiments was performed on an automated system to determine the evolution of total conductivity of samples with temperature. This system is equipped with a Solarton 1255 frequency response analyzer, effective in the frequency range 1Hz~1MHz, and a 200mV signal amplitude was used. In a second step, more accurate measurements were carried out on a non automated system, equipped with a computer-controlled Solartron 1260 impedance analyzer. The Equivcrt software was used to analyze the impedance diagram[1].

4.3 Tentative experiments to define the temperature range for measurements

The temperature dependence of total ionic conductivity for $(Bi_2O_3)_{0.75}(Y_2O_3)_{0.25}$, $(Bi_2O_3)_{0.75}(Dy_2O_3)_{0.25}$, $(Bi_2O_3)_{0.75}(Er_2O_3)_{0.25}$ samples sintered at 800°C for 1h is shown in Fig.4.5. Measurements were performed from 200 to 800°C every 25°C with a dwell of 60 minutes between each experiment. Two heating-cooling cycles were carried out. Each plot exhibits linear domain at low temperatures (T<600°C), and a curved region at higher temperatures. The activation energies determined in the low-temperature range are also shown, and all the values are about 1eV. The evolution was almost reversible.

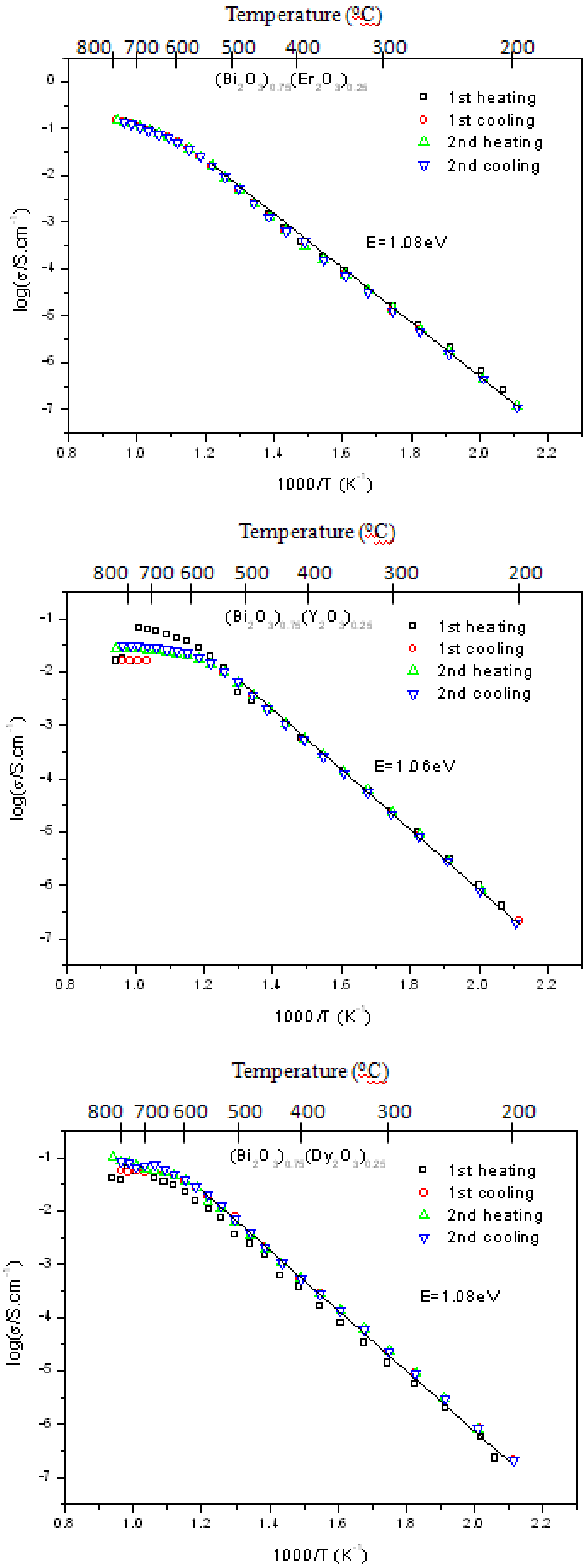

Fig.4.5 Total ionic conductivity of $(Bi_2O_3)_{0.75}(Er_2O_3)_{0.25}$, $(Bi_2O_3)_{0.75}(Y_2O_3)_{0.25}$ and $(Bi_2O_3)_{0.75}(Dy_2O_3)_{0.25}$ samples sintered at 800°C for 1h

In order to avoid grain growth and risk of metastability, it was decided to limit measurements up to 500°C for the following characterizations.

4.4 Impedance analysis

4.4.1 Impedance diagram as a function of the applied signal

To obtain more accurate data, manual experiments were carried out with a Solartron 1260 frequency response analyzer. Variable signal amplitudes were applied to separate out the electrolyte and the electrode contributions. Fig.4.6 shows the impedance diagrams collected at 300°C for $(Bi_2O_3)_{0.75}(Y_2O_3)_{0.25}$ sample as a function of the applied signal. For all impedance spectra given in the manuscript, impedance data were normalized by division by the sample form factor (e/S). The low frequency region is affected by changing the amplitude of the applied signal. Response under 100 and 200mV are quite similar but a decrease of the electrical resistance is observed for higher potentials. It indicates that the low frequency region of the impedance diagram corresponds to the electrode polarization. To be sure not to perturb the sample response and to get enough sensitivity, a potential of 200mV was chosen for the next measurements.

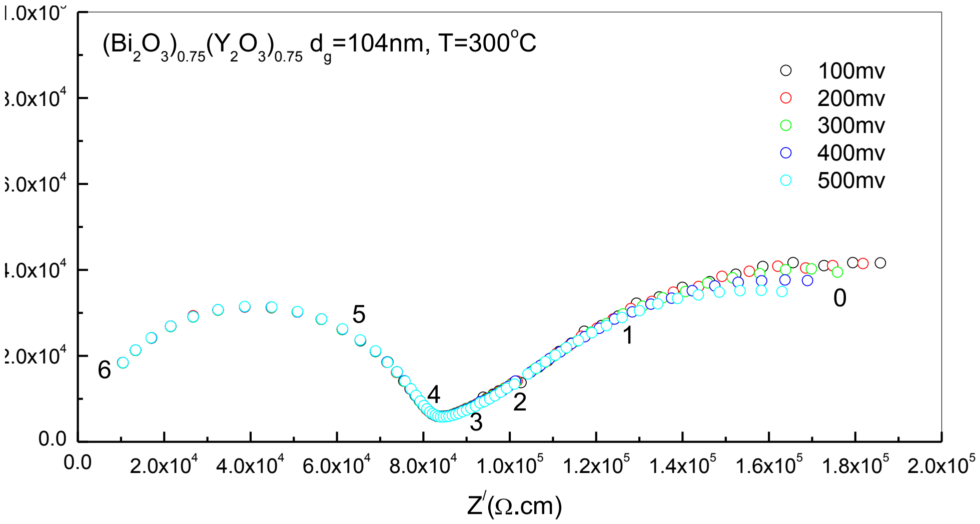

Fig.4.6 Impedance diagram for different amplitudes of applied signal for $Bi_{0.75}Y_{0.25}O_{1.5}$ specimens sintered at 800°C for 1h

4.4.2 Impedance diagrams of $(Bi_2O_3)_{0.75}(Y_2O_3)_{0.25}$ and $(Bi_2O_3)_{0.75}(Dy_2O_3)_{0.25}$ samples with different grain sizes

Impedance plots of $(Bi_2O_3)_{0.75}(Y_2O_3)_{0.25}$ and $(Bi_2O_3)_{0.75}(Dy_2O_3)_{0.25}$ samples versus temperature are shown in Fig.4.7 and Fig.4.8, respectively. At low temperature, between 220 and 375°C, only the $(Bi_2O_3)_{0.75}(Y_2O_3)_{0.25}$ sample with d_g=22nm displayed three-semicircles as expected from theory, while other samples showed only two semicircles, the first circle, likely being a convolution of bulk and grain boundary responses. For $(Bi_2O_3)_{0.75}(Y_2O_3)_{0.25}$ samples, only the response of electrode was observed above 450°C, while for $(Bi_2O_3)_{0.75}(Dy_2O_3)_{0.25}$ samples, the bulk response disappeared above 400°C, except for sample with d_g=20 nm, which still exhibited a HF semicircle at 450°C.

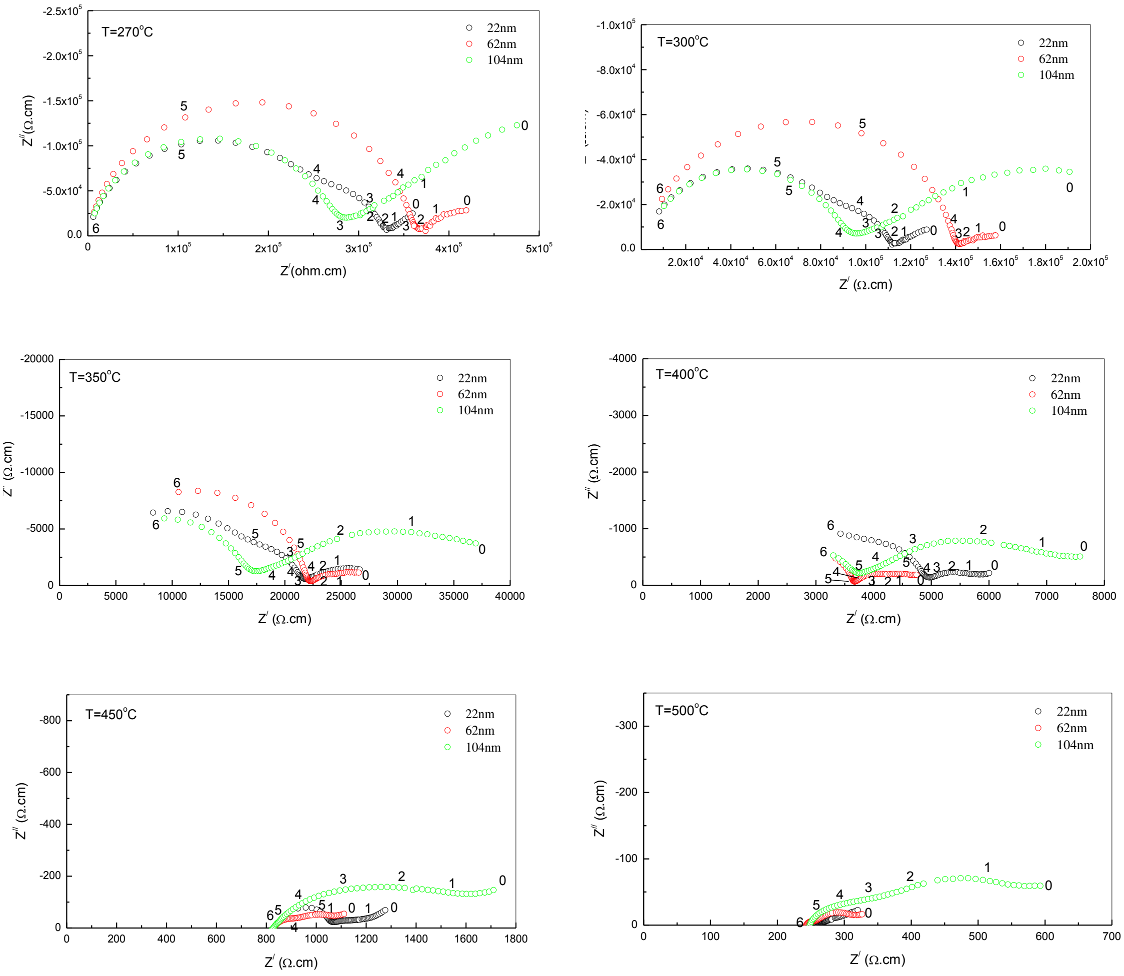

Fig.4.7 Impedance diagrams corresponding to $(Bi_2O_3)_{0.75}(Y_2O_3)_{0.25}$ samples with different grain size, measured at different temperatures

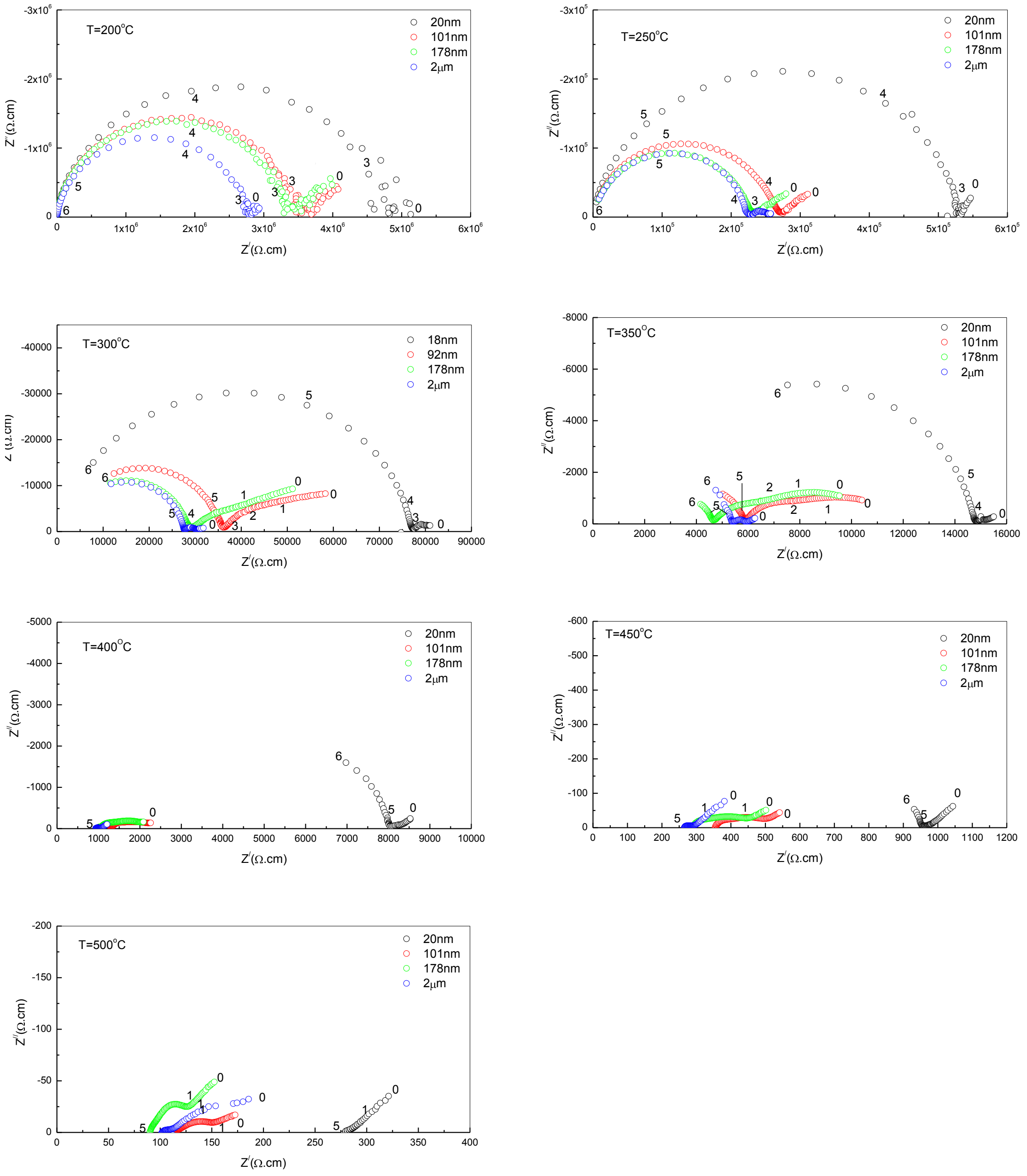

Fg.4.8 Impedance diagrams corresponding to $(Bi_2O_3)_{0.75}(Dy_2O_3)_{0.25}$ samples with different grain size, measured at different temperatures.

4.4.3 Analysis of the impedance diagrams of $(Bi_2O_3)_{0.75}(Y_2O_3)_{0.25}$ and $(Bi_2O_3)_{0.75}(Dy_2O_3)_{0.25}$ samples with different grain size

When excluding the electrode response, the impedance diagrams of $(Bi_2O_3)_{0.75}(Y_2O_3)_{0.25}$ sample with d_g=22nm were resolved using a two-semicircle model for temperatures between 220°C and 375°C, while all other samples were resolved using a one-semicircle model. According to the impedance diagrams, the schematics of the equivalent circuit for all samples are shown in Fig.4.9, and the parameter values measured at 270°C for $(Bi_2O_3)_{0.75}(Y_2O_3)_{0.25}$ sample and at 300°C for $(Bi_2O_3)_{0.75}(Dy_2O_3)_{0.25}$ sample are given in table 4.1.

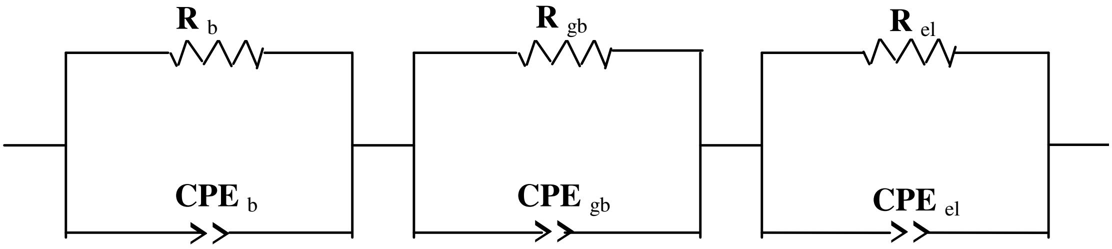

(a) Equivalent circuit used for $(Bi_2O_3)_{0.75}(Y_2O_3)_{0.25}$ sample d_g=22nm

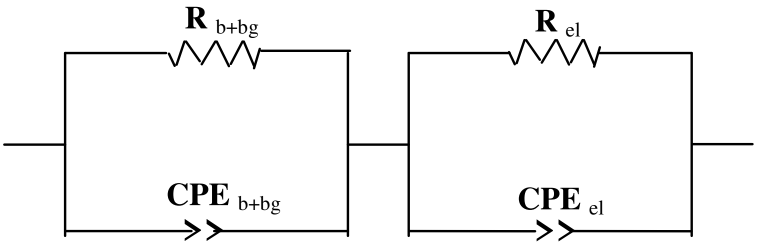

(b) Equivalent circuit used for other samples

Fig. 4.9 Equivalent circuit used to model the experimental data

Table 4.1 The equivalent circuit and parameter values

Sample	**e/S ($cm^{=1}$)**	**Equivalent circuit**	**Values of R (Ω), Y_0 (F) and n**
		$(Bi_2O_3)_{0.75}(Y_2O_3)_{0.25}$ at 270°C	
d_g=22nm	0.5196	(RQ)(RQ)	R=1.28×10^5, Y_0=1.18×10^{-10}, n=0.8625 R=4.23×10^4, Y_0=5.10×10^{-9}, n=0.8397
d_g=62nm	0.5153	(RQ)	R=1.86×10^5, Y_0=7.76×10^{-11}, n=0.8738
d_g=104nm	0.3901	(RQ)	R=1.08×10^5, Y_0=1.31×10^{-10}, n=0.8590
		$(Bi_2O_3)_{0.75}(Dy_2O_3)_{0.25}$ at 300°C	
d_g=20nm	0.6257	(RQ)	R=4.85×10^4, Y_0=1.22×10^{-11}, n=0.9673
d_g=101nm	0.3053	(RQ)	R=1.29×10^4, Y_0=2.15×10^{-11}, n=0.8604
d_g=178nm	0.4233	(RQ)	R=1.13×10^4, Y_0=1.33×10^{-11}, n=0.8413
d_g=2μm	0.3096	(RQ)	R=8.65×10^3, Y_0=2.53×10^{-11}, n=0.9466

Typical impedance diagrams of $(Bi_2O_3)_{0.75}(Y_2O_3)_{0.25}$ and $(Bi_2O_3)_{0.75}(Dy_2O_3)_{0.25}$ are also shown in Fig.4.10 as examples. For sample d_g=22nm, the capacitance values for the HF semicircle and LF semicircle are around 10^{-10} and 10^{-9} F, respectively. These values are within the accepted range for capacitance values corresponding to bulk and grain boundaries, respectively. For other samples, the capacitance of the HF was around 10^{-10} or 10^{-11}F. It was not possible from these data to separate bulk and grain boundaries. A capacitance of 10^{-6}F was deduced for the LF arc, in good agreement with the expected value for the electrode response.

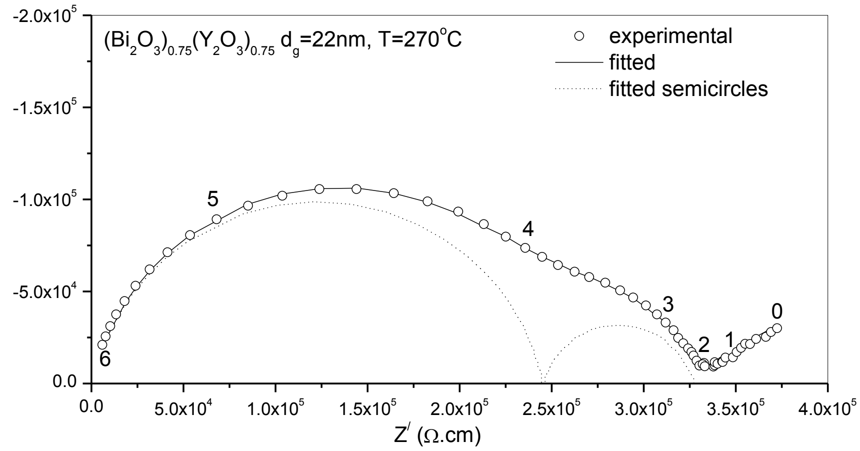

(a) Impedance diagram of $(Bi_2O_3)_{0.75}(Y_2O_3)_{0.25}$ sample d_g=22nm at 270°C

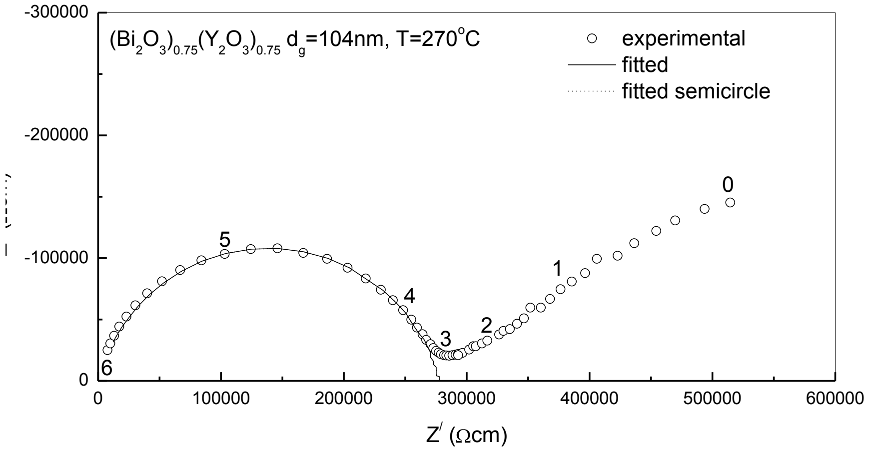

(b) A typical impedance diagram of other samples with only two semicircles

Fig.4.10 Typical impedance diagrams

In this work, polarization effects of the grains and the grain boundaries could not be separated, except in the case of $(Bi_2O_3)_{0.75}(Y_2O_3)_{0.25}$ sample with d_g=22nm. Similar behavior has already been observed for bismuth oxides doped with Er_2O_3, Y_2O_3 and MoO_3[2-5].

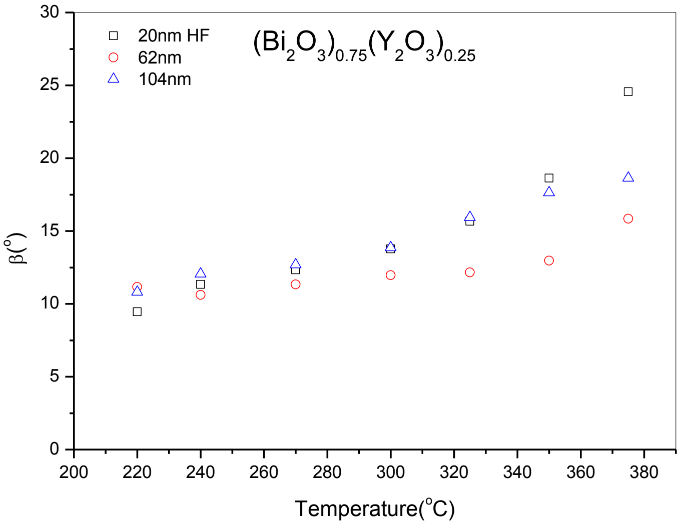

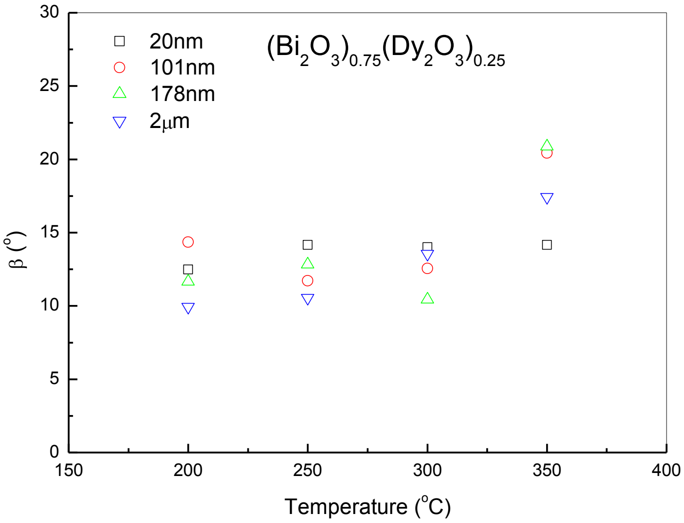

Fig.4.11 Dependence of the depression angle values on temperature for $(Bi_2O_3)_{0.75}(Y_2O_3)_{0.25}$ and $(Bi_2O_3)_{0.75}(Dy_2O_3)_{0.25}$ samples

Fig.4.11 shows the depression angle (β) value as a function of temperature for $(Bi_2O_3)_{0.75}(Y_2O_3)_{0.25}$ and $(Bi_2O_3)_{0.75}(Dy_2O_3)_{0.25}$ samples, respectively. This angle is usually obtained from fitting. If β exceed 30°, one-semicircle mode can not be used to resolve the impedance diagrams. All samples initially have constant β values and exhibit a rapid increase from temperatures higher than 300°C. However, in this case, β is always lower than 30°, indicating that one circle model can be used for the analysis.

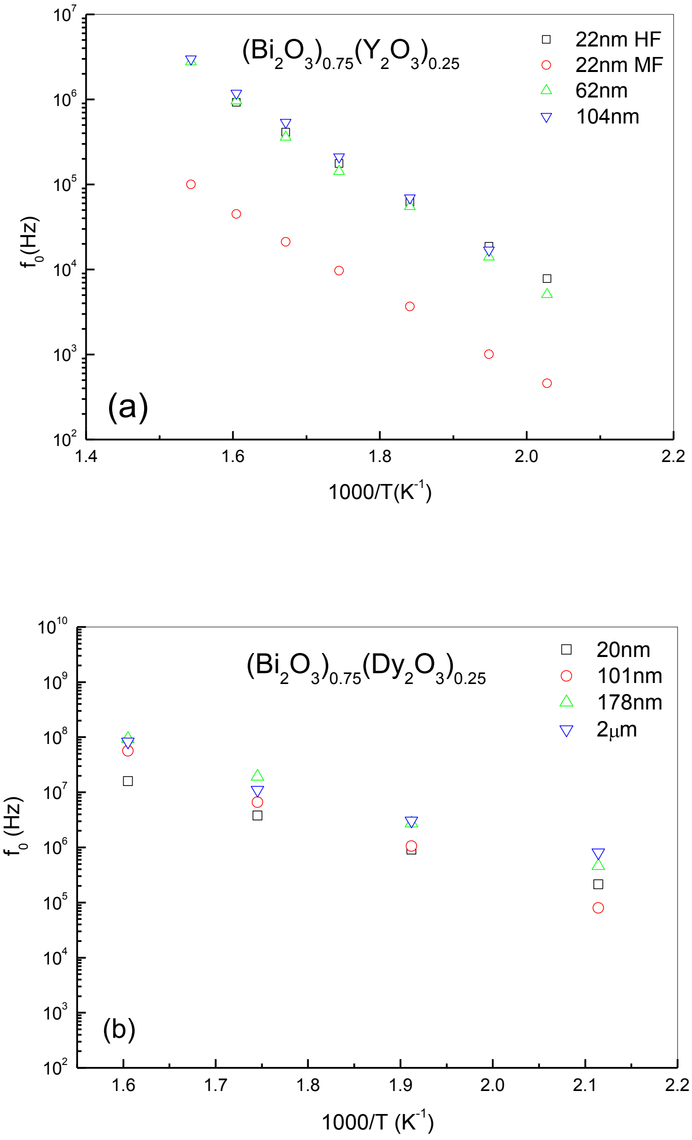

Fig.4.12 Relaxation frequency determined from the impedance diagrams of $(Bi_2O_3)_{0.75}(Y_2O_3)_{0.25}$ and $(Bi_2O_3)_{0.75}(Dy_2O_3)_{0.25}$

Fig.4.12 (a) and (b) show the relaxation frequency which derived from the fitting of the impedance diagram for $(Bi_2O_3)_{0.75}(Y_2O_3)_{0.25}$ and $(Bi_2O_3)_{0.75}(Dy_2O_3)_{0.25}$ samples, respectively. This parameter is an intrinsic characteristic of the material. It could be used to describe phase transition. In this case, no phase transition was observed during the experiment process. Furthermore, it is worth noting in case of $(Bi_2O_3)_{0.75}(Y_2O_3)_{0.25}$, the same relaxation frequency as for the bulk in case of sample with dg=22nm are observed for samples with bigger grains, which indicates that the bulk contribution increases when the grain size increases. Not much differences are observed for $(Bi_2O_3)_{0.75}(Dy_2O_3)_{0.25}$ samples.

4.4.4 Arrhenius plot of conductivity and effect of grain size on conductivity

Table 4.2 gives the bulk, grain boundary and total ionic conductivity of sample $(Bi_2O_3)_{0.75}(Y_2O_3)_{0.25}$ with d_g=22nm from Fig.4.7 at 220-375°C, and their evolution in function of temperature is given in Fig.4.13. The capacitances of the bulk and grain boundary can be calculated using the equation $C=1/(2\pi Rf_0)$, They are also listed in table 4.2.

Table 4.2 bulk, grain boundary and total conductivity of sample $(Bi_2O_3)_{0.75}(Y_2O_3)_{0.25}$ with d_g=22nm

T (°C)	**σ_g ($S.cm^{-1}$)**	**σ_{bl} ($S.cm^{-1}$)**	**σ_t ($S.cm^{-1}$)**	**C_{bulk} (F)**	**C_{bl} (F)**	**δ_{bl} (nm)**
220	5.04×10^{-7}	1.01×10^{-6}	3.36×10^{-7}	2.12×10^{-11}	5.57×10^{-10}	0.84
240	1.23×10^{-6}	2.75×10^{-6}	8.47×10^{-7}	2.02×10^{-11}	8.36×10^{-10}	0.53
270	4.06×10^{-6}	1.23×10^{-5}	3.06×10^{-6}	2.03×10^{-11}	1.02×10^{-10}	0.44
300	1.14×10^{-5}	4.52×10^{-5}	9.12×10^{-6}	1.99×10^{-11}	1.44×10^{-9}	0.30
325	2.64×10^{-5}	1.17×10^{-4}	2.15×10^{-5}	1.97×10^{-11}	1.70×10^{-9}	0.26
350	5.61×10^{-5}	2.92×10^{-4}	4.72×10^{-5}	1.87×10^{-11}	1.99×10^{-9}	0.21
375	1.29×10^{-4}	7.08×10^{-4}	1.09×10^{-4}			

The activation energy at 220-375°C associated to the bulk is 0.96eV, it is lower than the activation energy associated to the total conductivity (1.02eV). For the grain boundary, an activation energy of 1.18eV is deduced.

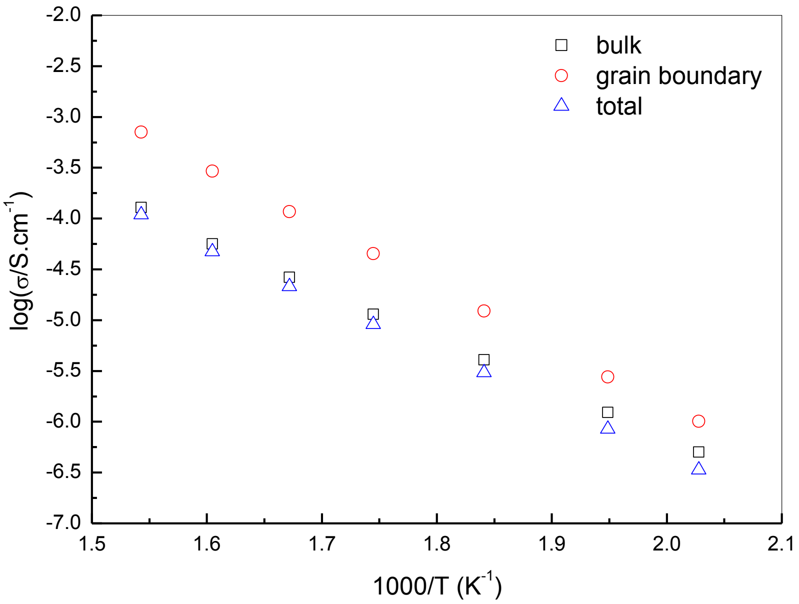

Fig.4.13 Total, bulk and grain boundary conductivity in function of temperature for $(Bi_2O_3)_{0.75}(Y_2O_3)_{0.25}$ sample with d_g=22nm

When considering the Brick layer model which is most supported for zirconia samples with high purity, these materials can be seen as consisting of cubic grains of the same size and homogeneous grain boundaries (Fig.4.14). From this model, the bulk capacitance can be expressed as $C_{bulk}=\varepsilon_0\varepsilon_{bulk}\frac{S}{nd_g}$, and the grain boundary capacitance as $C_{gb}=\varepsilon_0\varepsilon_{gb}\frac{S}{n\delta_{gb}}$, with S being the cross-section area of the sample, d_g the average grain size, and n the number of grains to be crossed in the current direction. Assuming, as for zirconia, dielectic constant is the same for the bulk and for grain boundary, the blocking thickness, δ_{gb}, can be derived as follow:

$$\delta_{gb}=\frac{\varepsilon_{gb}}{\varepsilon_{bulk}}\frac{C_{bulk}}{C_{gb}}d_g \approx \frac{C_{bulk}}{C_{gb}}d_g \qquad (4.19)$$

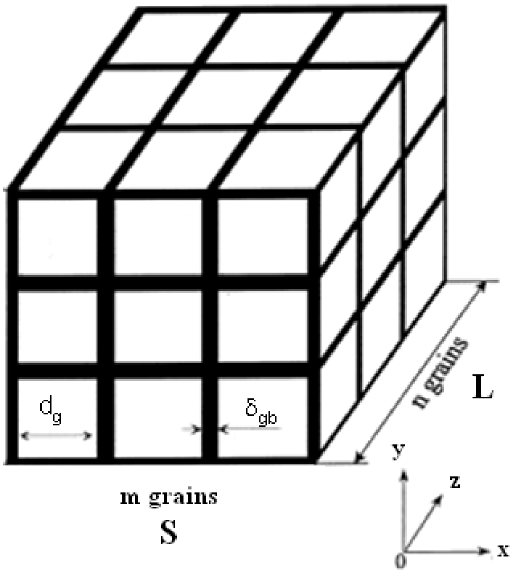

Fig.4.14 Brick layer model

δ_{gb}, values are given in table.4.2 for temperature between 240°C to 350°C, at which C_{bulk} and C_{gb} can be accurately determined. It is worth noting that δ_{bl} is nearly the same for all temperatures, about 0.5nm. In case of 8YSZ samples with grain size lower than 100nm, Boulfrad[6] obtained δ_{gb} values ranging from 2.7 to 7.6nm, our value is rather low and closer to the value they obtained for a ceramic with grain size of 242nm.

If the contribution to the conductivity parallel to the grain boundaries is negligible, the specific grain boundary conductivity can be estimated by the following equation:

$$\sigma_{gb}^{sp} = \sigma_{gb} \frac{\delta_{gb}}{d_g} \tag{4.20}$$

From this equation, the specific grain boundary resistivity was derived.

As shown in Fig.4.15, specific grain-boundary conductivity is about one order lower than the bulk conductivity. The same observation was reported in **§1.3** for ZrO_2- and CeO_2-based materials.

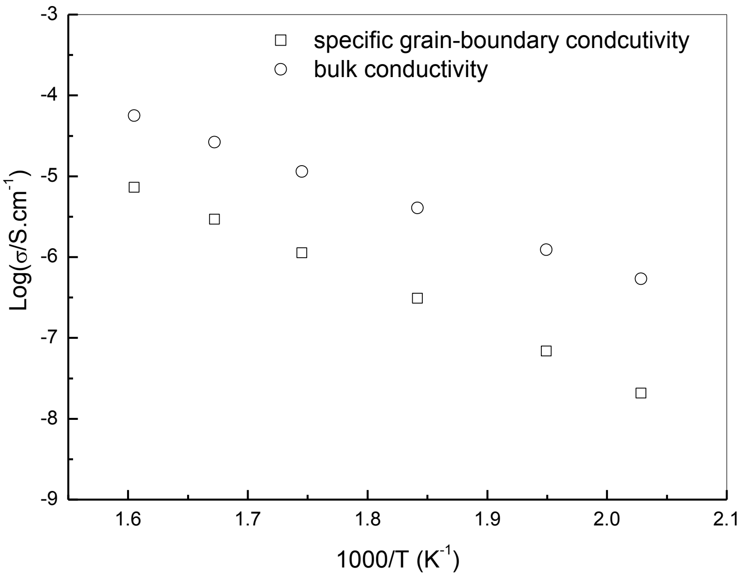

Fig.4.15 Specific grain-boundary conductivity and bulk conductivity $(Bi_2O_3)_{0.75}(Y_2O_3)_{0.25}$ sample with d_g=22nm as function of temperature

In their report on tetragonal zirconia, Guo *et al*[7], showed that the specific grain boundary conductivity increased when the grain size decreased. They noticed (see Fig.1.14, **§1.3**) that bulk conductivity didn't change too much when grain size decreased to the nanoscale, but specific grain boundary conductivity could increase by 1-2 orders of magnitude, although it remained lower than the bulk.

Unfortunately, in this study, grain boundary and bulk contribution could be separated for only one sample and it is not possible to extract the evolution of the bulk and grain boundary conductivities in function of the grain size.

Fig.4.16 shows the total ionic conductivity of $(Bi_2O_3)_{0.75}(Y_2O_3)_{0.25}$ samples from the impedance diagrams in Fig.4.7 (a) and from an automated set-up up to 575°C (b). From Fig.4.16 (a), it can be seen that the ionic conductivity of three samples are almost the same during the whole heating process. It increases quickly with the temperature increase and reached to 3.2×10^{-3} $S.cm^{-1}$ at 400°C. However, if the same conductivity is measured at high temperature, there are some discrepancies at low temperatures (200~350°C). The activation energies of each samples are 1.08, 1.14, and 1.09eV for d_g=22nm, d_g=62nm, and d_g=104nm, respectively. The sample with intermediate grain size d_g=62nm exhibits the lower ionic conductivity and the higher activation energy, whereas the lower activation energy is observed for sample with d_g=22nm. It is also worth noting that bulk conductivity for sample d_g=22nm is very close to sample with large grain size with slightly lower activation energy (0.96eV).

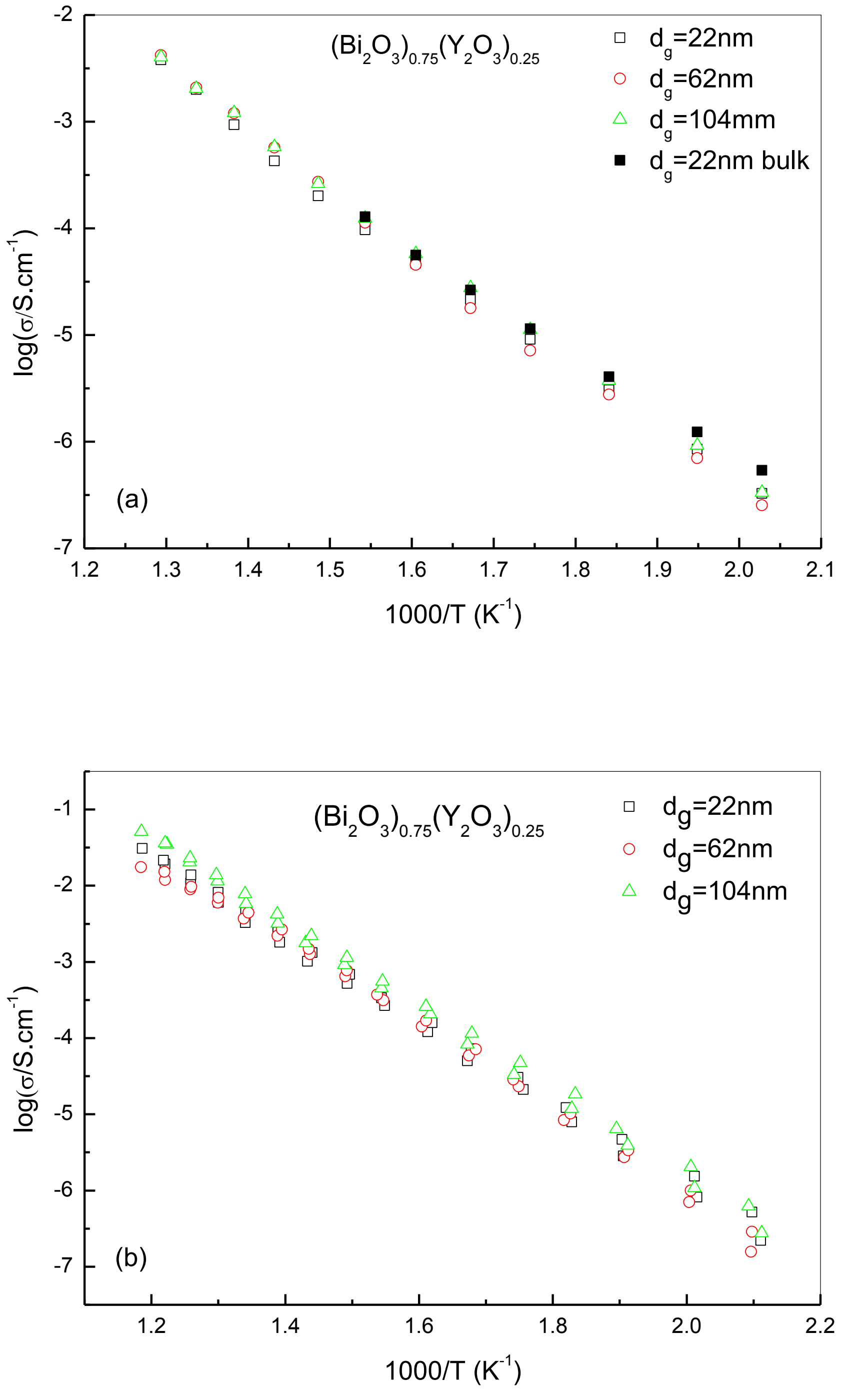

Fig.4.16 Total ionic conductivity of $(Bi_2O_3)_{0.75}(Y_2O_3)_{0.25}$ samples measured (a) from the impedance diagrams in Fig.4.7 (a); (b) from an automated set-up (in this case, only one heating-cooling cycle was measured)

In Fig.4.16 (b), at low temperature, the better conductivity of sample d_g=22nm, when compared to sample d_g=62nm, is confirmed but data are scattered at intermediate temperatures.

Fig.4.17 shows the total ionic conductivity of $(Bi_2O_3)_{0.75}(Dy_2O_3)_{0.25}$ samples. For each sample, the total conductivity increases quickly with temperature increase. At 500°C, it reaches to 10^{-2} S.cm^{-1} for sample with grain size of 101nm, 178nm and 2μm and 3.16×10^{-3} S.cm^{-1} for sample with grain size of 20nm. Moreover, it can be seen that the conductivity decreases with decrease of grain size and is really lower for sample with grains of 20nm. However, activation energies remain in the same order of magnitude, 1.08, 1.06, 1.08 and 1.02eV, from large grains to small grains. Moreover, it is worth noting that, as shown by X-ray diffraction on pellet after experiment, all samples remained in δ form after the impedance study.

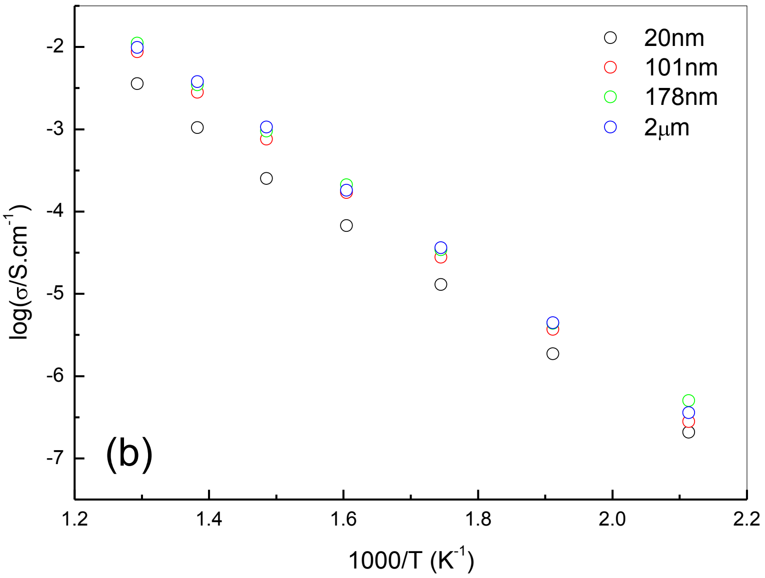

Fig.4.17 Total ionic conductivity of $(Bi_2O_3)_{0.75}(Dy_2O_3)_{0.25}$ samples

The measurements of total ionic conductivity of $(Bi_2O_3)_{0.75}(Dy_2O_3)_{0.25}$ samples were also carried out on an automated set up in the temperature range from 200 to 575°C. Two heating-cooling cycles were carried out. A reversible evolution was observed and the stability of samples was confirmed by X-ray diffraction after impedance measurements. The results confirmed the decrease in total ionic conductivity with decrease of grain size.

Then, the same measurements were performed on $(Bi_2O_3)_{0.75}(Er_2O_3)_{0.25}$ and $(Bi_2O_3)_{0.75}(Er_2O_3)_{0.125}(Y_2O_3)_{0.125}$ samples. Fig.4.18 gives the total ionic conductivity of $(Bi_2O_3)_{0.75}(Er_2O_3)_{0.25}$ and $(Bi_2O_3)_{0.75}(Er_2O_3)_{0.125}(Y_2O_3)_{0.125}$ samples with different grain sizes.

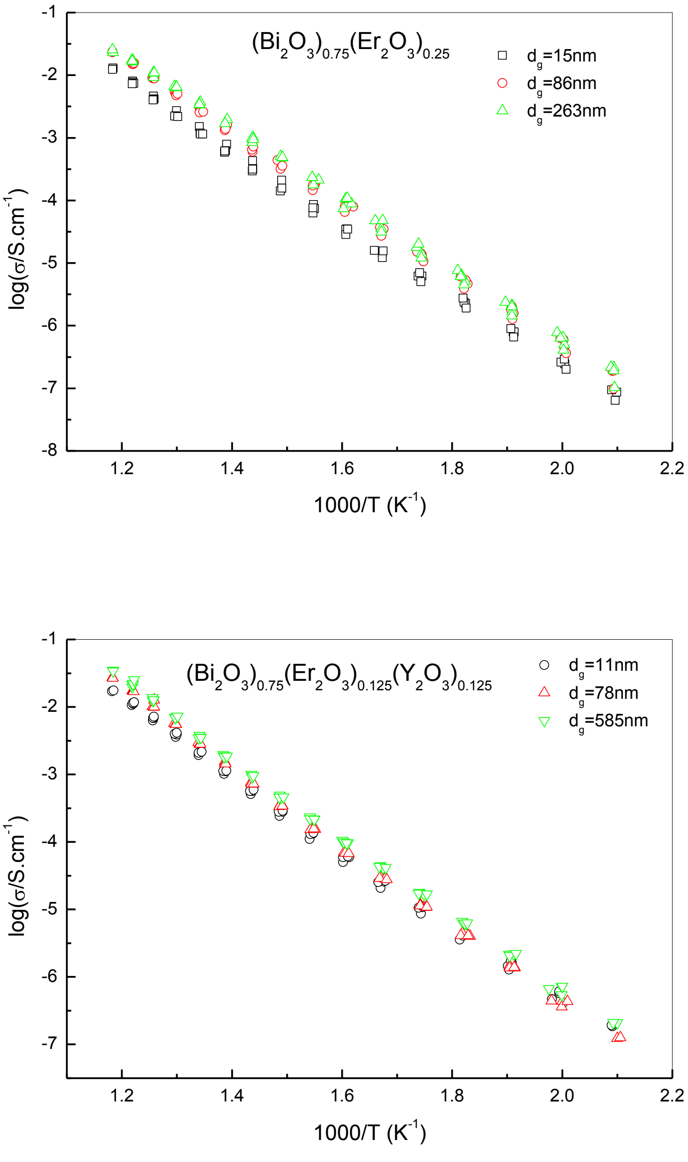

Fig.4.18 Total ionic conductivity of $(Bi_2O_3)_{0.75}(Er_2O_3)_{0.25}$ and $(Bi_2O_3)_{0.75}(Er_2O_3)_{0.125}(Y_2O_3)_{0.125}$ samples

Here again, a reversible evolution was observed and samples were confirmed to be stable. The decrease in the total ionic conductivity with decrease of grain size was also observed for the erbium doped compounds but, interestingly, as for yttrium doped compound, almost no evolution with grain size was observed for the double substituted compound, containing yttrium.

Table 4.3 gives the total ionic conductivity of $(Bi_2O_3)_{0.75}(Ln_2O_3)_{0.25}$ (Ln=Dy, Y, Er) samples with smallest grain size at 300°C and 500°C. In contrast to Nakayama's report[8], here best conductivities were obtained for Y doped compounds. However, Dy samples are the second in the list and intermediate values are obtained for the Er/Y sample.

Table 4.3 Total ionic conductivity ($S.cm^{-1}$) of $(Bi_2O_3)_{0.75}(Ln_2O_3)_{0.25}$ (Ln=Dy, Y, Er) samples with smallest grain size at 300°C and 500°C (grain size is given into brackets)

	300°C	**500°C**
$(Bi_2O_3)_{0.75}(Dy_2O_3)_{0.25}$ (20nm)	1.15×10^{-5}	4.20×10^{-3}
$(Bi_2O_3)_{0.75}(Y_2O_3)_{0.25}$ (22nm)	2.11×10^{-5}	6.03×10^{-3}
$(Bi_2O_3)_{0.75}(Er_2O_3)_{0.25}$ (15nm)	0.62×10^{-5}	2.71×10^{-3}
$(Bi_2O_3)_{0.75}(Er_2O_3)_{0.125}(Y_2O_3)_{0.125}$ (11nm)	0.86×10^{-5}	3.60×10^{-3}

4.5 Conclusion

Impedance spectroscopy was carried out on dense ceramics of $(Bi_2O_3)_{0.75}(Dy_2O_3)_{0.25}$, $(Bi_2O_3)_{0.75}(Er_2O_3)_{0.25}$, $(Bi_2O_3)_{0.75}(Y_2O_3)_{0.25}$ and $(Bi_2O_3)_{0.75}(Er_2O_3)_{0.125}(Y_2O_3)_{0.125}$ with grain size ranging from 20nm to 2μm to study the effect of grain size on ion conductivity. From the results, it was concluded that a decrease of the conductivity with the grain size decrease was usually observed, except for yttria doped ceramics for which almost no evolution with the grain size was observed. Although, in most cases, it was not possible to separate the bulk conductivity and the grain boundary effect, this decrease was assumed to be due to an increase of the blocking effect when the density of grain boundary increases. In contrast to Nakayama's report[8] which indicated best properties for Dy samples, in this study best conductivities were obtained for Y doped compounds.

References

[1] Boukamp BA, Solid State Ionics, 1986, **20**: 31
[2] Macdonald JR, Impedance Spectroscopy, Wiley, New York, 1987
[3] Duran P, Jurado JR, Moure C, Valverde N, Steele BCH, Mater. Chem. Phys., 1987, **18**: 287.
[4] Wang LS and Bamett SA, *J. Electrochem. Soc.,* 1992, **139**: 2567.
[5] Suzuki T, Kaku K, Ukawa S, Dansui Y, *Solid State Ionics,* 1984, **13**: 237.
[6] Boulfrad S, Djurado E, Dessemond L. *Fuel Cells*, 2008, **5**: 313.
[7] Guo X, Zhang ZL. *Acta Materialia*, 2003, **51**: 2539.
[8] Nakayama S. *Ceram. Int.*, 2002, **28**: 907.

Conclusion

In this study, $(Bi_2O_3)_{0.75}(Dy_2O_3)_{0.25}$, $(Bi_2O_3)_{0.75}(Y_2O_3)_{0.25}$, $(Bi_2O_3)_{0.75}(Er_2O_3)_{0.25}$, $(Bi_2O_3)_{0.75}(Er_2O_3)_{0.125}(Y_2O_3)_{0.125}$ nano powders were prepared using a reverse chemical titration method. Dense ceramic of Ln_2O_3 doped Bi_2O_3 solid electrolytes with different grain size were obtained by SPS and pressureless sintering. Then, the effect of grain size on ionic conductivity of these ceramics was studied. The following conclusions can be drawn:

(1) In order to avoid the formation of $BiONO_3$ and to obtain oxides and hydroxides as precipitate, thermodynamic equlibrium in the solution was analyzed to determine a suitable pH value. The precipitation was obtained by pouring, drop by drop, a nitrate solution of precursors (0.1mol/L) in an aqueous solution of ammonia (50mL in 550mL) with pH=11.5. BiOOH, $Dy(OH)_3$, $Y(OH)_3$ and $Er(OH)_3$ were predicted as the final products, respectively, if the equilibrium could be achieved. However, little nitrate was still observed from TG-MS and Raman spectrum.

(2) From TG-MS, XRD and Raman spectrometry, annealing conditions were optimized. The most homogeneous powders were obtained when the precipitate was filtered and annealed at 500°C for 3 hours. Although nitrates remained in the sample, their amount was less than 1%. From the crystallographic point of view, the obtained powders were mainly in the β-form although one can not discard the possibility of δ-form in the mixture. As shown by combining XRD and TEM, for all compositions, single crystal grains with size of about 20nm were obtained. XRF results showed that there was no formula deviation from the expected one.

(3) According to the predominance area diagram of Bi-O, Bi-Dy-O, Bi-Er-O and shrinkage curves, the conditions of sintering were optimized for compositon $(Bi_2O_3)_{0.75}(Dy_2O_3)_{0.25}$. Two techniques were used: Spark Plasma Sintering and pressureless sintering. Once optimized, the conditions were then applied to other compositions.

(4) With SPS, dense ceramics with relative density higher than 95% were obtained at 500°C for 1 min by SPS, XRD showed all samples exhibited the δ form with grain size of about 20nm.

(5) The condition of pressureless sintering was optimized by studying the grain growth behaviour and relative density versus times at different temperature for $(Bi_2O_3)_{0.75}(Dy_2O_3)_{0.25}$. The evolution of grain size with sintering time showed that the grain growth is controlled by mass transport through the grain boundaries. At last,

dense ceramics with relative density higher than 94% were obtained at 700°C for 2h, 750°C for 1h and 800°C for 1h. XRD showed that all samples were in δ form with grain size from 60nm to 500nm, depending on sintering temperature and compositions.

(6) Although what was expected at the beginning of this study, the decrease of grain size does not led to a better stability of δ forms at 650°C. However, they remain stable up to 500°C.

(7) $(Bi_2O_3)_{0.75}(Dy_2O_3)_{0.25}$ and $(Bi_2O_3)_{0.75}(Y_2O_3)_{0.25}$ impedance spectra were studied in details. For most of them, a single semi-circle was observed on Nyquist diagram and it was not possible to separate the bulk response from the grain boundary response. However, for $(Bi_2O_3)_{0.75}(Y_2O_3)_{0.25}$ sample with d_g=22nm, two semi-circles were observed.

(8) The effect of grain size on ion conductivity of Bi_2O_3-based solid electrolytes was studied, and the results showed that for all the compositions, except sample containing yttrium, the total ionic conductivity decreased with the decrease of grain size. This could be explained by a predominant blocking effect due to grain boundaries.

To conclude, in this work, it has been shown that bismuth based ceramics with grain size at the nano-scale could be easily obtained from nano-powders. However, except in the case of yttria stabilized ceramics, a decrease of the conductivity is observed when the grain size decreases, likely because of a blocking effect due to grain boundaries. For small grain size a space charge effect is possible but has not been demonstrated.

Annexes

Annexe.1 Structure model

α-Bi_2O_3 [1]

Cell: a=5.8496(3) Å, b=8.1648(4) Å, c=7.5101(4) Å, α=90, β=112.977(3), γ=90.
$P2_1/c$ (14) V=330.23.

Atom	(site)	x	y	z	Occupancy
Bi1	(4e)	0.5242(6)	0.1843(4)	0.3615(4)	1
Bi2	(4e)	0.0404(5)	0.0425(4)	0.7767(4)	1
O1	(4e)	0.7783(8)	0.3037(5)	0.7080(7)	1
O2	(4e)	0.2337(8)	0.0467(5)	0.1266(6)	1
O3	(4e)	0.2658(7)	0.0294(6)	0.5115(6)	1

β-Bi_2O_3 [2]

Cell: a=7.741(3) Å, b=5.634(2) Å, α=90.
$P\text{-}42_1c$ V=337.61

Atom	(site)	x	y	z	Occupancy
Bi1	(8e)	0.2539(7)	0.2532(10)	0.3615(4)	1
O1	(8e)	0.3074(7)	0.027(2)	0.7080(7)	1
O2	(4d)	0.5	0.101(2)	0.1266(6)	1

References:

[1] Harwig HA. *Zeitschrift fuer Anorganische und Allgemeine Chemie*, 1978, **444**: 151-166.
[2] Blower SK, Greaves C. *Acta Crystallographica C*, 1988, **44**: 587-589

Annexe.2 Definition of the reliability factors

The quality of the agreement between observed and calculated profiles is measured by a set of nowadays conventional factors. In FullProf two sets of reliability factors are calculated, according to the meaning of the integer N. In the first set N is the total number of points used in the refinement (N=NPTS-NEXC=total number of points in the pattern-total number of excluded points). In the second set only those points where there are Bragg contributions are taken into account. The definition of the reliability factors is as follows:

The profile $Rp = 100\sum_i|y_{oi}-y_{ci}| / \sum_i|y_{oi}|$

The weighted profile $Rwp = 100[\sum_i w_i|y_{oi}-y_{ci}|^2 / \sum_i w_i|y_{oi}|^2]^{1/2}$

The Bragg $R_B = 100\sum_k|I_k-I_{ck}| / \sum_k|I_k|$

The expected $Rexp = 100[(N-P+C)/ \sum_i(w_i\, y_{oi}^2)]^{1/2}$

Where N-P+C is the number of degrees of freedom (N=NPTS-NEXC=total number of points in the pattern - total number of excluded points; P =the number of refined parameters and C= the number of strict constraint functions.)

R_F =100*Sum{n}[|Fobs(n)-sqrt(Sum{k}[F^2cal(k)])|]/Sum{n}[Fobs(n)]

where Fobs=Sqrt(F2obs).

Annexe.3 Characterization techniques

Final density was measured by Archimede method.

$$\rho_s = \frac{m_2 \rho_0}{m_1 + m_2 + m_3}$$

Where ρ_s is the density of samples, m_1 is the mass of bottle with water, m_2 is the mass of sample, m_3 is mass of (bottle+water+ sample) and ρ_0 is the density of water.